

AN ABSTRACT OF THE THESIS OF

Sheng - wei Lee for the degree of Master of Science

in Atmospheric Sciences presented on July 1, 1982

Title: Analysis of Surface Wind Stress and Ocean

Circulations Simulated by General Circulation Models

Abstract approved: Redacted for Privacy
Young - June Han

Surface wind stress simulated by OSU two-level atmospheric general circulation model is analyzed in terms of its spatial and temporal characteristics. It is shown that the main features of the annual mean field in Northern Hemisphere are 10 to 20 degrees too south of the corresponding observational positions. The patterns in the Southern Hemisphere, however, are well simulated. The monthly mean fields reveal a distinct seasonal variability which is highly dependent on latitude. Spectral and cross-spectral analysis of the 3-year time series show that eastward traveling synoptic time scale disturbances dominate the variability. The long period disturbances are symmetric and have no preferred directions of propagation.

The ocean circulations simulated by the barotropic version of the OSU six-layer ocean general circulation model using simulated wind stress are found to be largely

controlled by the wind stress curl field. The seasonal variabilities of the corresponding mass transport are larger than that of the circulation driven by observed wind stress due to the stronger variability of the curl field of the simulated wind stress. Planetary waves with westward phase propagation and eastward group velocity are likely to constitute a major part of the response of a barotropic model to the fluctuating winds.

ANALYSIS OF SURFACE WIND STRESS
AND OCEAN CIRCULATIONS SIMULATED
BY GENERAL CIRCULATION MODELS

by

SHENG-WEI LEE

A THESIS

submitted to

Oregon State University

in partial fulfillment of
the requirements for the
degree of

Master of Science

Commencement June 1983

APPROVED:

Redacted for Privacy

Assistant Professor of the Department of
Atmospheric Sciences
in charge of major

Redacted for Privacy (Acting for W. L. Gates)

Chairman of the Department of Atmospheric Sciences

Redacted for Privacy

Dean of Graduate School

Date thesis is presented July 1, 1982

Typed by Shu-Ching Hu for Sieng-Wei Lee

ACKNOWLEDGMENT

I would like to express my gratitude to Dr. Y.-J. Han for his guidance and assistance in this research, and to Dr. S. K. Esbensen for his valuable comments on some of the material. I also sincerely thank Mr. W. R. McKie for his expert help in most of the computer programming and constructive review of the manuscript.

TABLE OF CONTENTS

1.	INTRODUCTION	1
2.	DESCRIPTION OF THE AGCM SIMULATED WIND STRESS FIELDS AND THE COMPARISON WITH OBSERVED FIELDS	5
2.1.	Calculation of surface wind stress in the AGCM	7
2.2.	3-year mean wind stress fields	11
2.2.1	Vectors	12
2.2.2	Zonal-component	15
2.2.3	Meridional-component	18
2.2.4	Curl	25
2.2.5	Root mean square wind stress	28
2.3.	Seasonal Variations	32
2.3.1	Vectors	32
2.3.2	Curl	43
3.	SPECTRAL ANALYSIS OF THE SIMULATED WIND STRESS	51
3.1.	Autospectral analysis	51
3.1.1	Algorithm and method of calculation	51
3.1.2	Autospectra of simulated wind stress	56
3.2.	Cross-spectral analysis	67
3.2.1	Algorithm and method of calculation	67
3.2.2	Cross-spectra of selected fields	71
4.	BAROTROPIC OCEAN EXPERIMENT	80
4.1.	The ocean circulation driven by the AGCM simulated wind stress	82
4.2.	Seasonal variation of simulated ocean transport	89
5.	SUMMARY	99
6.	BIBLIOGRAPHY	103

LIST OF FIGURES

Figure		page
2.1.	Schematic representation of the OSU AGCM's vertical structure.	6
2.2.	Annual mean observed wind stress vectors.	13
2.3.	3-year mean AGCM-simulated wind stress vectors.	14
2.4.	Zonal-component of the 3-year mean AGCM-simulated wind stress.	16
2.5.	Zonal-component of the annual mean observed wind stress.	17
2.6.	Zonal means of the simulated and observed zonal-component of the wind stress.	19
2.7.	As is fig. 2.4 except for meridional component.	20
2.8.	As in fig. 2.5 except for meridional component.	22
2.9.	As in fig. 2.6 except for meridional component.	24
2.10.	3-year mean AGCM-simulated wind stress curl.	26
2.11.	Annual mean observed wind stress curl.	27
2.12.	Zonal means of the simulated and observed wind stress curl.	29
2.13.	Root mean square observed wind stress over (a) North Pacific (b) North Atlantic Oceans. (after Willebrand (1978))	30
2.14.	Root mean square simulated wind stress over global oceans.	31
2.15.	Monthly variation of zonal mean of observed zonal-component of the wind stress.	33
2.16a.	Mean observed wind stress vectors for January.	34
2.16b.	As in fig. 2.16a except for July.	35
2.17.	As in fig. 2.15 except for simulated wind stress.	37

2.18a.	Mean simulated wind stress vectors for three Januaries.	38
2.18b.	As in fig. 2.18a except for April.	39
2.18c.	As in fig. 2.18a except for July.	40
2.18d.	As in fig. 2.18a except for October.	41
2.19a.	Mean observed wind stress curl for January.	44
2.19b.	As in fig. 2.19a except for July.	45
2.20a.	Mean simulated wind stress curl for three Januaries.	46
2.20b.	As in fig. 2.20a except for April.	47
2.20c.	As in fig. 2.20a except for July.	48
2.20d.	As in fig. 2.20a except for October.	49
3.1.	Longitudinally averaged autospectra over the North Pacific Ocean at 42N (J=34).	57
3.2.	Longitudinally averaged spectra of horizontal stress at 5 latitudes over the North Pacific Ocean.	59
3.3.	Autospectra at (90E, 10N) (I=55, J=26).	61
3.4.	Autospectra at 4 points over the South Pacific Ocean.	63
3.5.	Autospectra at (160E, 42N) (I=69, J=34).	65
3.6.	Longitudinally averaged autospectra of zonal-component wind stress for the summer and winter over the North Pacific Ocean at 42N.	66
3.7.	Coherence and phase spectra of stress components for two points at (170E, 30N) and (160E, 30N) with a east-west separation of 963 Km.	72
3.8.	As in fig. 3.7 except for two points at (170E, 30N) and (150E, 30N) with an east-west separation of 1926 Km.	74
3.9.	As in fig. 3.7 except for two points at (160E, 30N) and (160E, 34N) with a south-north separation of 445 Km.	76

3.10.	As in fig. 3.7 except for two points at (160E, 34N) and (160E, 42N) with an south-north separation of 890 Km.	78
3.11.	Coherence and phase spectra of zonal component wind stress for two points at (175W, 58N) and (175E, 58N) with an east-west separation of 589 Km.	79
4.1.	Annual mean streamfunction of the mass transport of the oceanic circulation driven by the AGCM simulated surface wind stress.	84
4.2.	Streamfunction of the mass transport at day 90 of the oceanic circulation driven by observed surface wind stress.	85
4.3a.	Monthly mean streamfunction of the simulated transport for January.	90
4.3b.	As in fig. 4.3a except for April.	91
4.3c.	As in fig. 4.3a except for July.	92
4.3d.	As in fig. 4.3a except for October.	93
4.4a.	Time-longitude plot of the streamfunction along 34N (J=32) for day 180-240 of the simulation.	97
4.4b.	As in fig. 4.4a except for day 300-360.	98

ANALYSIS OF SURFACE WIND STRESS
AND OCEAN CIRCULATIONS SIMULATED
BY GENERAL CIRCULATION MODELS

1. INTRODUCTION

The ocean has long been recognized as an important component in the earth's climate. Due to the large coverage of the earth's surface and the high specific heat of water, the ocean acts as a heat reservoir. It influences the climate through its exchange of heat and moisture with the atmosphere and the poleward transport of energy by the ocean currents. Vonder Haar and Dort (1973) found that the oceanic transports are at least of comparable overall importance as atmospheric transports. Thus, it is necessary to take into account the hydrosphere as well as the atmosphere for better modeling of the climate. The first experiment using a coupled ocean-atmosphere model was done by Manabe (1969) who performed a series of controlled experiments to investigate the problem of ocean-atmosphere interaction. Later, Manabe et al. (1975) carried out a subsequent experiment with realistic global geography and found further evidence of the role of oceans.

The Climatic Research Institute at OSU has recently been devoting much effort to couple a new 6-level ocean general circulation model (OGCM) to the existing 2-level atmospheric general circulation model (AGCM). Schlesinger and Gates (1981) examined the role of the ocean in the maintenance of global climate in a series of five simulations using the OSU AGCM with different surface conditions. Han and Gates studied the performance of OSU OGCM first by a homogeneous wind-driven ocean experiment (1982a), then by a baroclinic ocean experiment in which the ocean is driven by thermohaline forcing as well as wind forcing (1982b). A third experiment which combined the OGCM with a mixed layer and sea-ice model is now in progress. The coupled AGCM-OGCM model will then be used in climate experiments. The main purpose of this study is to examine the behavior of the AGCM simulated wind stress which, in the coupled model, is to be explicitly used by the OGCM as one of the major forcing fields from the overlying atmosphere.

Surface wind stress is an important factor in the atmosphere-ocean system. It represents the principal mechanism for the dissipation of atmospheric kinetic energy (Gates, 1979). It also contributes to the ocean the major part of energy for maintaining the semi-permanent currents and the corresponding mass transport. Sverdrup (1947)

showed that the mass transport for most of the ocean can be approximated from a knowledge of wind stress alone. Later, Bryan (1963) demonstrated, with a numerical model of a barotropic ocean, the sensitivity of mass transport to the wind stress field. Therefore, in order to get better simulation of the ocean current and the associated mass and energy transport, a reasonably good set of wind stress data is greatly in need.

The first systematic computation of the wind stress was made by Scripps Institute of Oceanography in 1948. Hidaka (1958) later extended the computation to three major world oceans. Both computations used only the mean speed in each direction category of the wind rose which, according to Hellerman (1965), would significantly underestimate the wind stress magnitude by 10-30%. Hellerman (1967) revised Hidaka's calculation by utilizing wind roses with both direction and speed frequencies. More recently, Han and Lee (1981) compiled a new set of monthly mean stress data over the global ocean using updated climatological monthly mean wind data. The calculated stress data extended to high-latitude oceans and revealed many features which were not resolved in earlier analyses.

Once the wind stress field is established, it is

desirable to know its space-time variability which might contribute to the strong variability as which is frequently observed in the ocean. Several spectra of wind speed at certain stations in the surface layer have been documented. Examples are at stations on the Oregon coast (Frye et al., 1972), on the tropical Pacific island of Palmyra (Hwang, 1970), at weathership P on NE Pacific (Fissel, 1976), etc. Willebrand (1978) analyzed surface parameters, including wind stress, over Northern Oceans and found that eastward propagating disturbances with period shorter than 10 days dominate the atmospheric variability.

In the following, the spatial distribution of the 3-year mean wind stress and stress curl fields simulated by the OSU AGCM are reviewed. Their seasonal variabilities are also discussed. These fields are compared against the observational fields whenever available. The next chapter will deal with the space-time characteristics of the simulated wind stress. Results of the auto- and cross-spectral analysis are shown. In the last chapter, the simulated wind stress is actually tested on the OGCM with homogeneous stratification. Streamfunction fields of ocean mass transport are compared with those simulated by the same model driven by observed wind stress. Seasonal variabilities of the simulated streamfunction fields are also discussed.

2. DESCRIPTION OF THE AGCM SIMULATED WIND STRESS FIELDS AND THE COMPARISON WITH OBSERVED FIELDS

In this chapter, the surface wind stress field generated by the OSU AGCM will be described in detail in terms of mean field and temporal variations. The OSU AGCM is a primitive equation model for the troposphere. It is formulated in the σ vertical coordinate system with σ defined as

$$\sigma = (P - P_T) / (P_s - P_T)$$

where P is the pressure, P_s and P_T the pressures at the surface and top of the model atmosphere. The vertical structure is sketched in Fig.2.1. The atmosphere is divided into two layers with equal mass. At the center of each layer are the reference levels 1 and 3 with σ equals 1/4 and 3/4 respectively. The interface between the layers is level with $\sigma = 1/2$. The tropopause corresponds to $\sigma = 0$ and the surface is always given by $\sigma = 1$. The kinematic boundary condition $\dot{\sigma} = d\sigma/dt = 0$ is applied at the earth's surface and the top of the model atmosphere. The primary dependent variables in the model are the horizontal velocity V , temperature T , and specific humidity q for both layers, together with the surface pressure parameter $\pi (= P_s - P_T)$. The reader is referred to Gates et al. (1971),

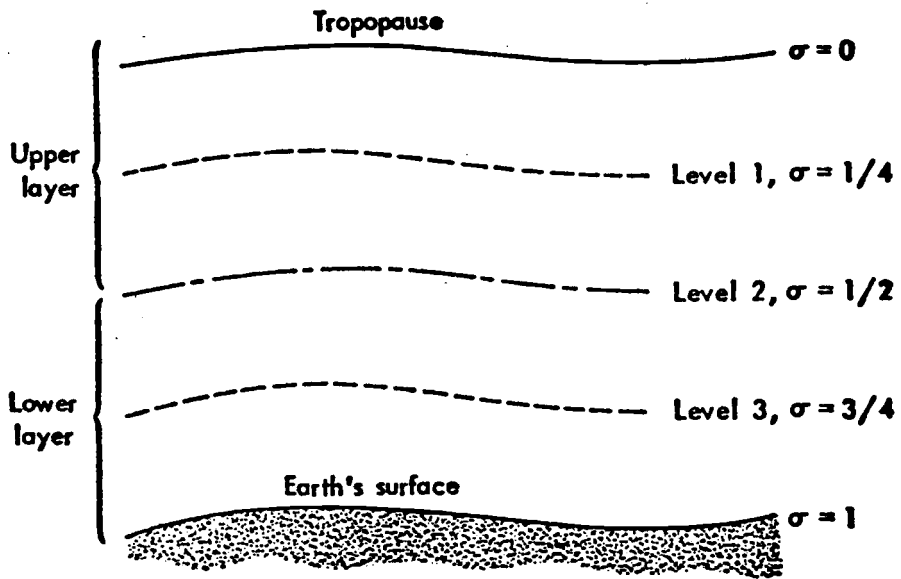


Fig. 2.1. Schematic representation of the OSU AGCM's vertical structure. (after Gates et al. (1971))

Gates and Schlesinger (1977), Schlesinger and Gates (1979) for detailed description of the model's physical aspects and numerical methods. The horizontal grid size is 5° in longitude and 4° in latitude. A B-scheme grid structure is adopted in which the horizontal velocity is carried at a point that is staggered one-half grid length latitudinally and longitudinally from the point where variables T , q , π and the geopotential $\bar{\phi}$ are carried.

2.1 Calculation of Surface Wind Stress in the AGCM

Surface wind stress $\vec{\tau}_s$ (or turbulent flux of momentum) serves as part of the frictional force in the lower layer of the AGCM. It is parameterized by the bulk aerodynamic method

$$\vec{\tau}_s = \rho_4 C_D V_s' \vec{V}_s \quad (2.1.1)$$

where ρ_4 is the surface air density, V_s' the effective surface wind speed and \vec{V}_s the vector surface wind.

The surface wind is extrapolated from the vector wind at level 3 and level 1 according to the formulae:

$$\vec{V}_s = 0.7 \vec{V}_4 = 0.7 \left(\frac{3}{2} \vec{V}_3 - \frac{1}{2} \vec{V}_1 \right) \quad (2.1.2)$$

and the effective wind speed is given by

$$V_s' = \max(|\vec{V}_s|, G) \quad (2.1.3)$$

where G is the gustiness parameter ($= 2$ m/sec). The drag coefficient C_D is given by

$$C_D = \begin{cases} 2(1 + 3 \frac{Z_s}{5000}) \times 10^{-3} & \text{over no water surfaces} \\ \min[(1 + 0.07|\vec{V}_s|, 2.5] \times 10^{-3} & \text{over water surfaces} \end{cases} \quad (2.1.4)$$

where Z_s is the surface elevation in meters.

The drag coefficient has been an uncertain parameter in evaluating the surface wind stress. It is known to be affected by the surface wind speed and stability condition. The latter was shown to have very little effect on estimation of monthly mean wind stress (Esbensen and Reynolds, 1981). The formulation of the drag coefficient over water surface in the AGCM is suggested by Deacon and Webb (1962), and is linearly dependent on wind speed.

The numerical values of C_D over ocean for various wind speeds are tabulated in Table 2.1. Also included in the table, as a comparison, are the C_D 's used by Han and Lee (1981) (hereafter referred to as HL) and Willebrand (1978). HL took the values for the neutral stability condition from the table given by Bunker (1976). Willebrand calculated C_D from the formulae given by Garratt (1977):

$$C_D = (0.75 + 0.067 |\vec{V}_s|) \times 10^{-3} \quad (2.1.5)$$

Table 2.1 Three estimates of the drag coefficient (10^{-3})

Wind speed (m/sec)	AGCM	Bunker	Garratt
0 - 5	1.00 - 1.35	1.20	0.75 - 1.09
5 - 10	1.35 - 1.70	1.54	1.09 - 1.42
10 - 15	1.70 - 2.05	1.87	1.42 - 1.76
15 - 20	2.05 - 2.40	2.16	1.76 - 2.09
20 - 25	2.40 - 2.50	2.40	2.09 - 2.43
25 - 30	2.50	2.60	2.43 - 2.76
30 - 35	2.50	2.80	2.76 - 3.10
35 - 40	2.50	3.00	3.10 - 3.43
40 - 50	2.50	3.20	3.43 - 4.10
>50	2.50	3.40	>4.10

As can be seen, for wind speed lower than 25 m/sec, the value by Garratt's formulae is the smallest whereas the other two are comparable. For wind speed larger than 25 m/sec, the value in AGCM was held constant while the other two continued increasing. The large difference at higher speed is not important because such speed is rarely found near the surface.

The source-sink terms in the governing equations (and hence the surface wind stress) are evaluated at every sixth

time step, that is, once every hour, using the latest values of the dependent variable. The wind stress values were saved every six hours.

Since the observed stress fields recently analyzed by HL (1981) will be heavily used as the verification of the AGCM's simulated stress, we will briefly review the algorithm and data source of their calculation.

The primary surface wind data used for the stress calculation were obtained from the National Climatic Center (NCC). These data are defined on a $5 \times 5^\circ$ Marsden subsquare grid for each of the 12 calendar months, and represent observed climatological surface winds available up to 1974.

The zonal and meridional component of the wind stress at each grid point, a weighted average over direction-speed space, were computed for each of the 12 calendar months from the formulae:

$$\begin{aligned} \tau_x &= \left[\sum_{ij} F_{ij} \rho C_i U_{ij}^2 \sin \theta_j \right] / \sum_{ij} F_{ij} \\ \tau_y &= \left[\sum_{ij} F_{ij} \rho C_i U_{ij}^2 \cos \theta_j \right] / \sum_{ij} F_{ij} \end{aligned} \quad (2.1.6)$$

where F_{ij} is the unnormalized frequency (probability of

occurrence) of wind speed U_{ij} ; U_{ij} is the observed wind in speed category i and direction category j ; θ_j is the angle for direction j ; C_i is the surface drag coefficient for the speed category i and ρ is the air density.

The NCC data set provides only the mean speed and frequency in eight directions (N, NE, E, ... NW) plus total standard deviation of the speed. A Gaussian distribution of wind speed for each direction was found to give a satisfactory estimation of the wind stress.

Special care was taken in the data-sparse areas, mainly in high latitudes. This involved a merging of the stress field calculated from the NCC data with the geostrophically computed wind stress field, and a spatial smoothing which removed the possible discontinuity due to the merging.

2.2 3-YEAR MEAN FIELDS

We will look at the mean fields of the vectors, zonal and meridional components, curl and root mean square of the simulated wind stress in this section. The mean fields are the averages of the 6 hourly fields over three years of simulation.

2.2.1 Vectors

Fig. 2.2 shows the global distributions of the annual mean observed stress vector. The main gyres are found in the eastern part of the ocean basins. In the Northern Hemisphere, the westerly stress turns clockwise below 50N and counterclockwise above 50N in both oceans. The southern boundary of the westerlies is at 30N in both oceans. The northern boundary, however, is at 55N in the Pacific and 60N in the Atlantic. In the Southern Hemisphere, the westerly stress counterclockwise equatorward of 35S and clockwise near Antarctica. The boundaries between westerlies and easterlies are at 30S and 70S.

Fig. 2.3 shows the distribution of simulated wind stress vectors. In the north Pacific, the stress is westward almost everywhere except between 40N and 20N. The cyclonic gyre is found centered at (175E, 45N) which is about 15 degree south of the observed gyre. The observed anticyclonic gyre near North America is not seen. In the north Atlantic, the cyclonic and anticyclonic gyres are well defined except that they are 20 and 10 degrees south of the corresponding those that are observed. This also means that the westerly stress belt is 10 degree narrower. As shown in fig. 2.2, the annual mean observed stress is

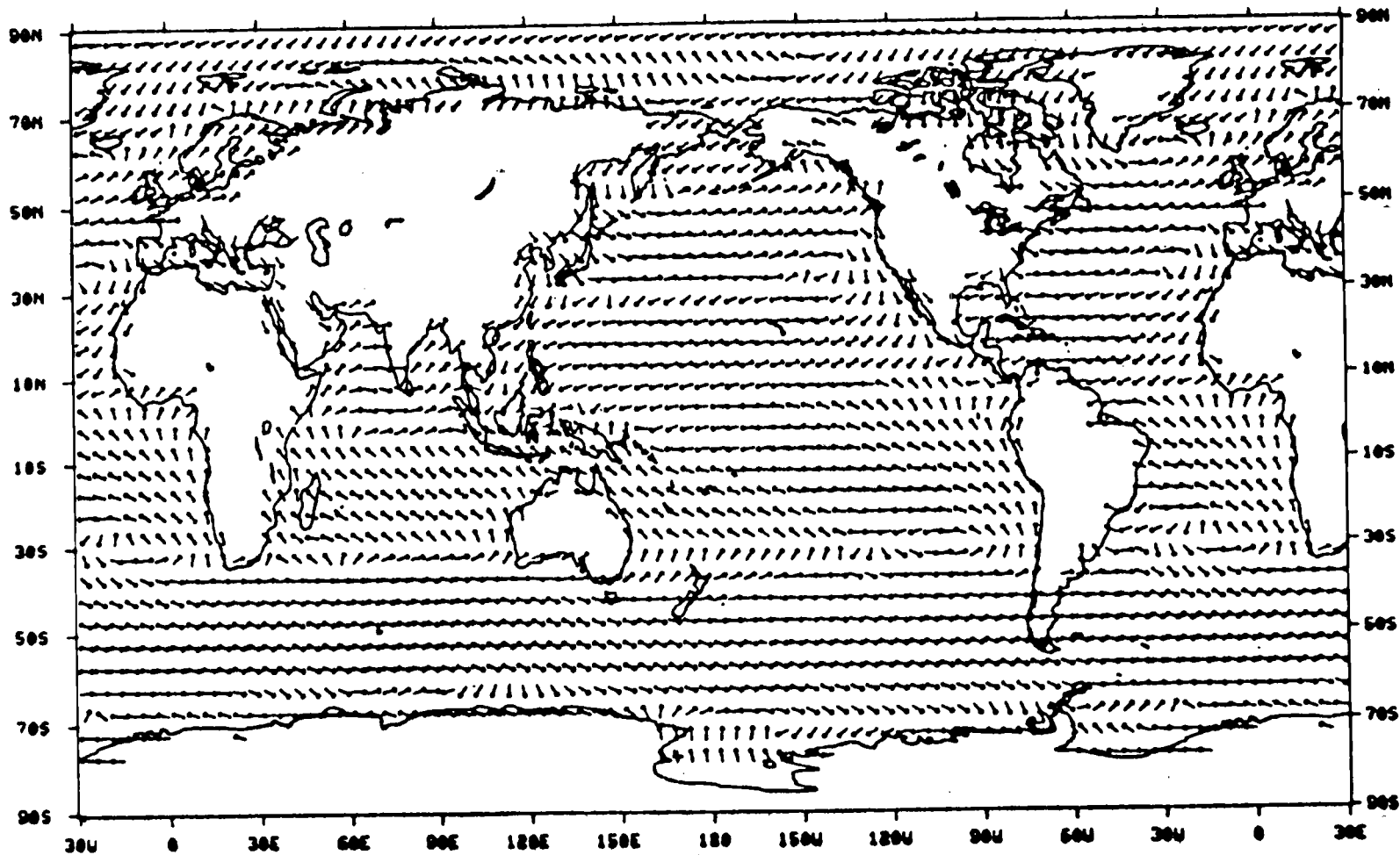


Fig. 2.2. Annual mean observed wind stress vectors.
(after Han and Lee (1981)).

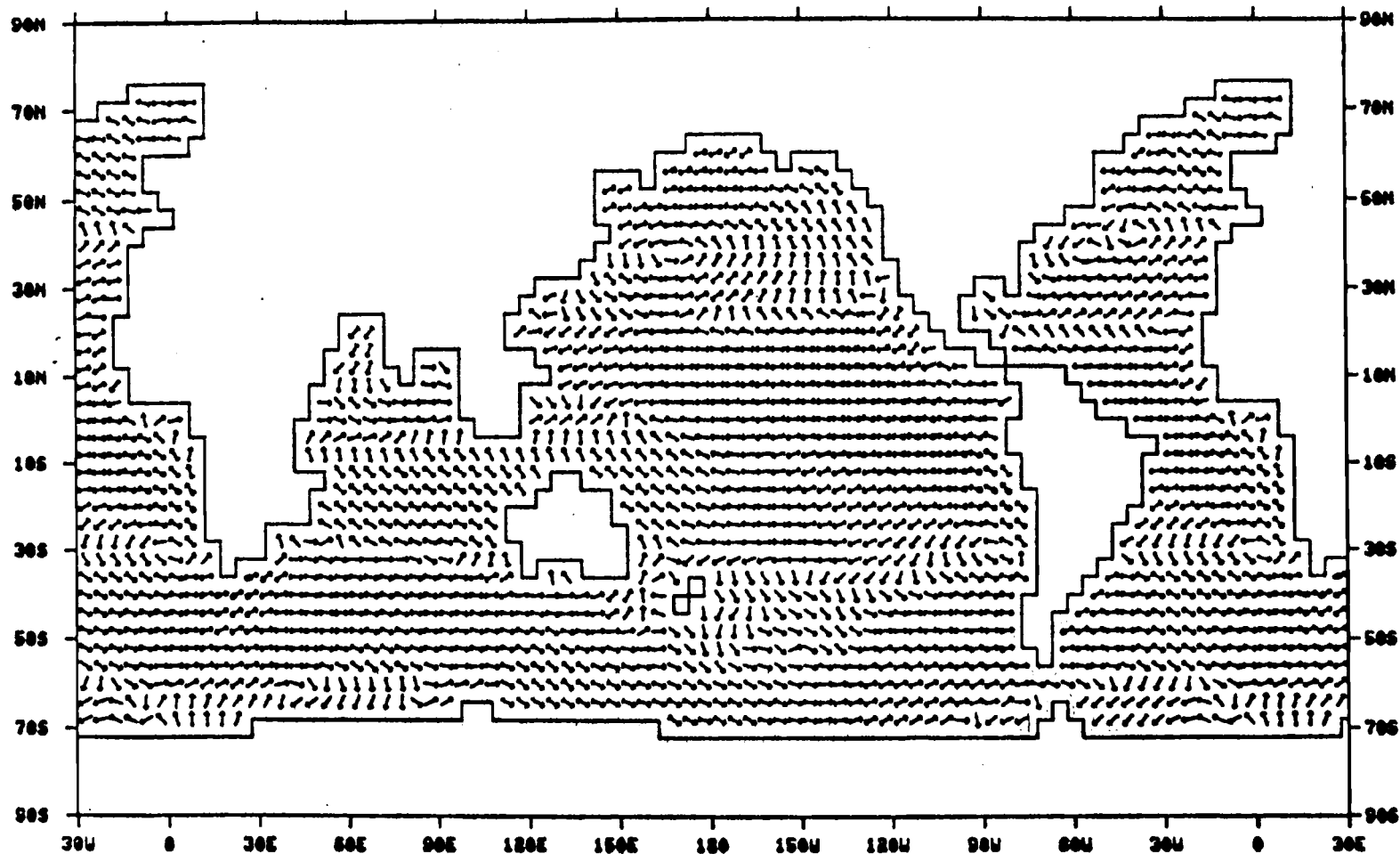


Fig. 2.3. 3-year mean AGCM-simulated wind stress vectors.

southwesterly and weak northwesterly over the North Indian Ocean despite the dominating northeasterly stress from November through April. While the simulated field shows fairly strong northeasterly and northwesterly stress dominating this area. This will be discussed in a later part of this chapter.

The distribution over the Southern Hemisphere is fairly well simulated. The cyclonic gyres on the eastern part of the ocean are clearly seen near 30S. They are 10 degrees east of the observed gyres. Consequently, the simulated northward stress along the west coast of continents is confined to a relatively narrow band.

2.2.2 Zonal component

Fig. 2.4 shows the global distribution of the zonal component of the simulated wind stress. The region between 20N and 30S is dominated by westward stress except in the North Indian Ocean. The pattern is similar to that of the observed field (fig. 2.5). The magnitude is smaller on the average, except for eastern part of the south Pacific where a center is found to have a value of 1.2 dyne cm^{-2} ,

while the center at approximately the same location on the observed field is 1.0 dyne cm^{-2} . South of 30S, the

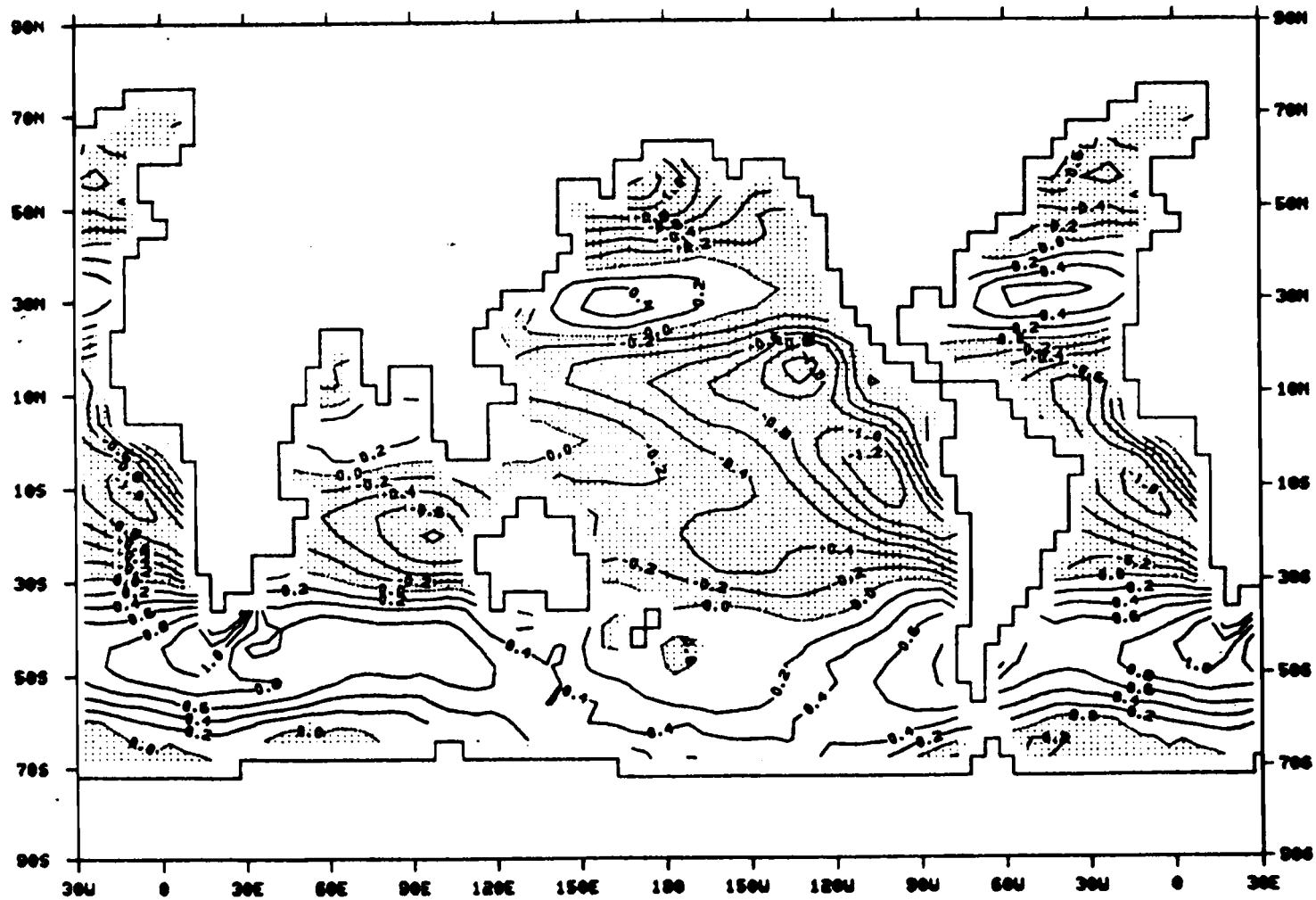


Fig. 2.4. Zonal-component of the 3-year mean AGCM-simulated wind. Contour interval is 0.2 dyne/cm². The zero lines are dashed and negative values are stippled.

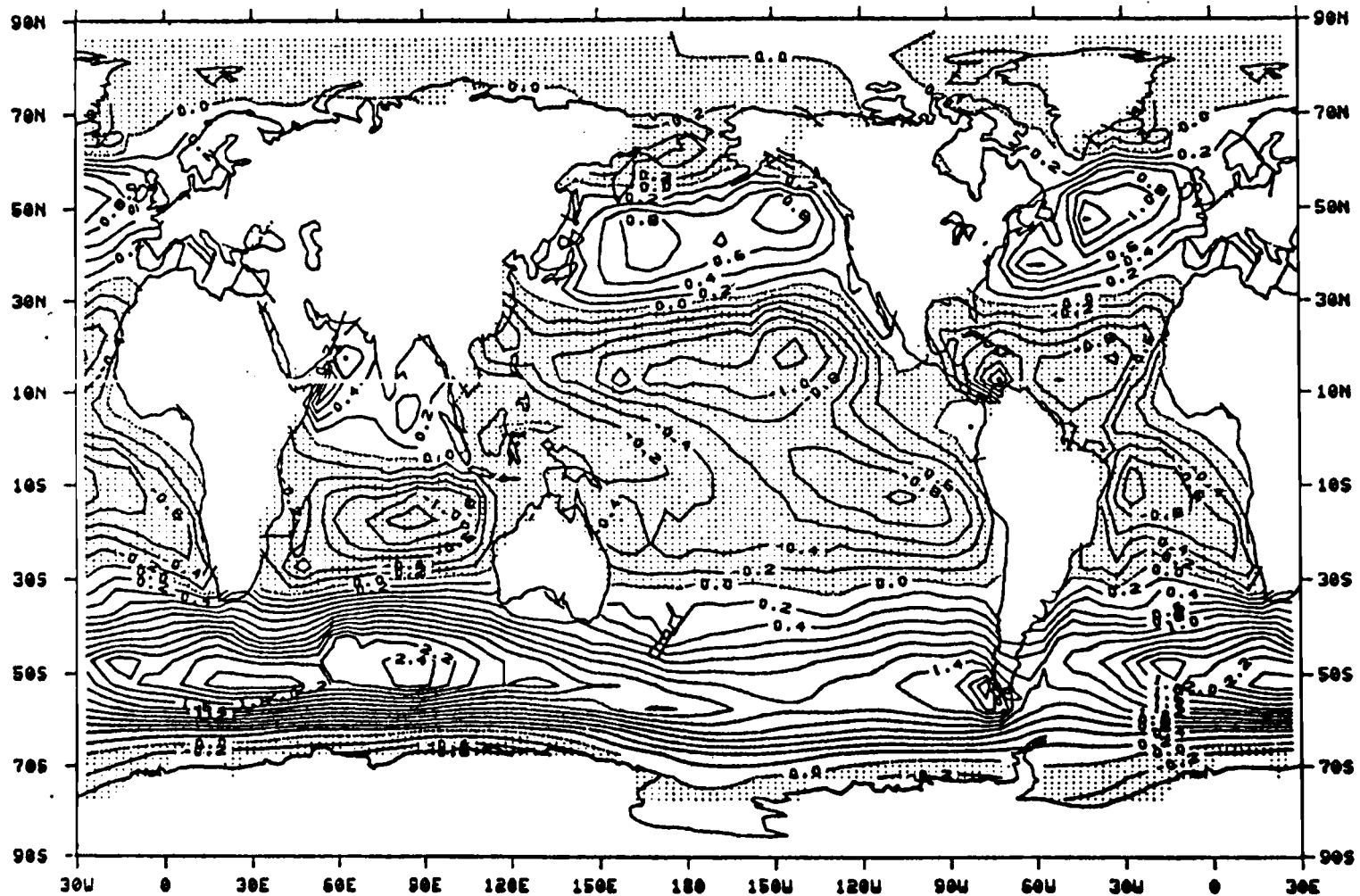


Fig. 2.5. As in Fig.2.4 except for annual mean observed wind stress.

eastward stress dominates most of the area with a maximum center near the tip of South Africa. The pattern is also similar to the observed field, but the magnitude of eastward stress is much smaller. This can be clearly seen from the zonal mean curve shown in fig. 2.6. The distribution over northern oceans again reflects the south-shift of the main gyres. The north and south bounds of positive area are 18 and 6 degrees south of those of the observed field. The maximum values of the centers located at (165E, 30N) and (53W, 30N) are 0.5 and 0.7 dyne cm^{-2} , compared to 0.9 and 1.3 dyne cm^{-2} for the observation. The south-shift is also illustrated by the phase difference between the two curves shown in fig. 2.6. The dominating westward stress in high latitude of North Hemisphere is relatively strong compared to the observation. The maximum value at the center of the Bering Sea is 1.2 dyne cm^{-2} while no value over 0.4 dyne cm^{-2} is found over that area in the observed field.

2.2.3 Meridional component

Fig. 2.7 shows the meridional component (τ_y) of the simulated wind stress. In the Northern Hemisphere, positive values are found north of 15N and east of 170E over the Pacific and almost everywhere north of 15N over the Atlantic. Negative values are mainly on the western

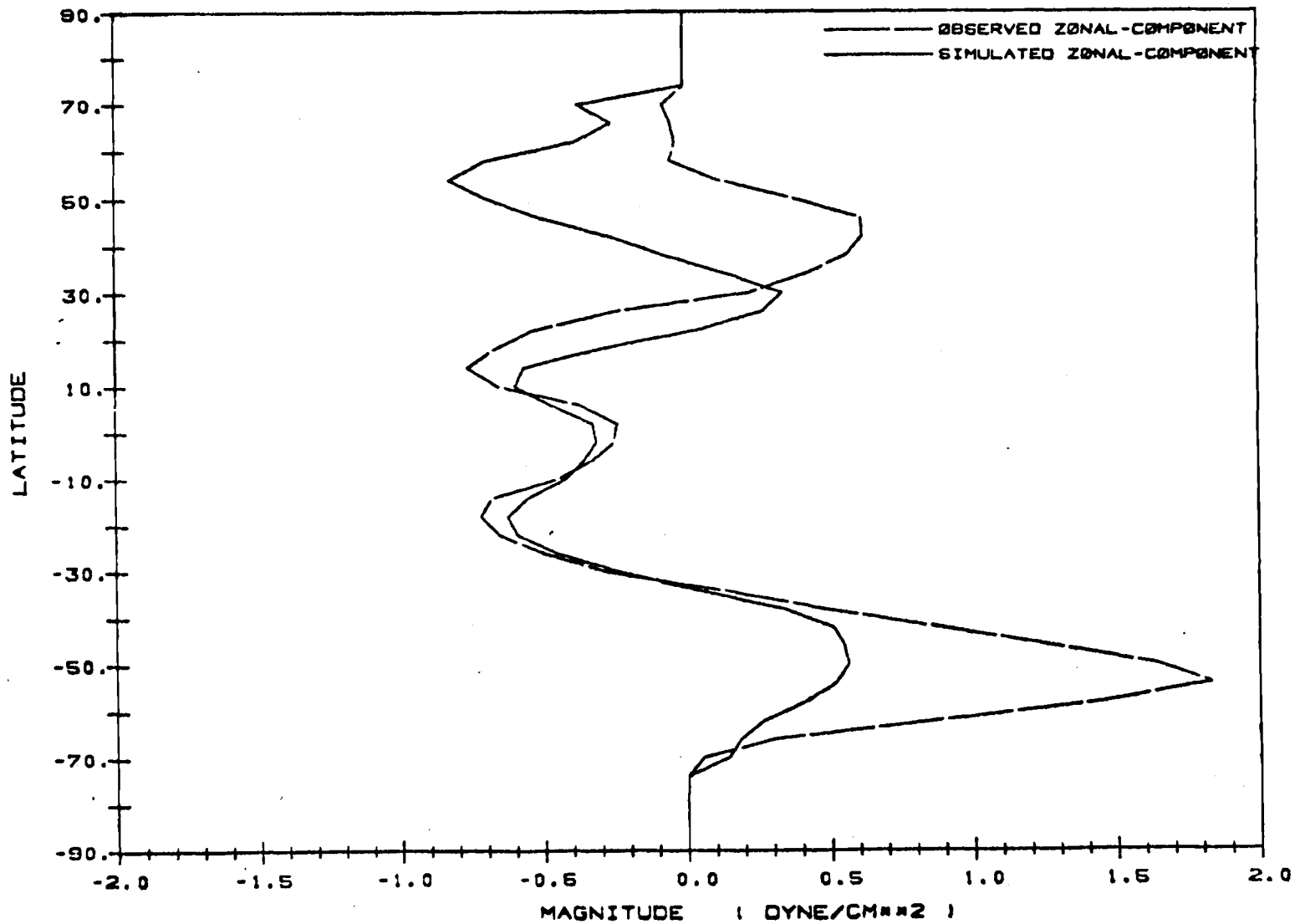


Fig. 2.6. Zonal means of the simulated (solid lines) and observed (dashed lines) zonal-component of the wind stress.

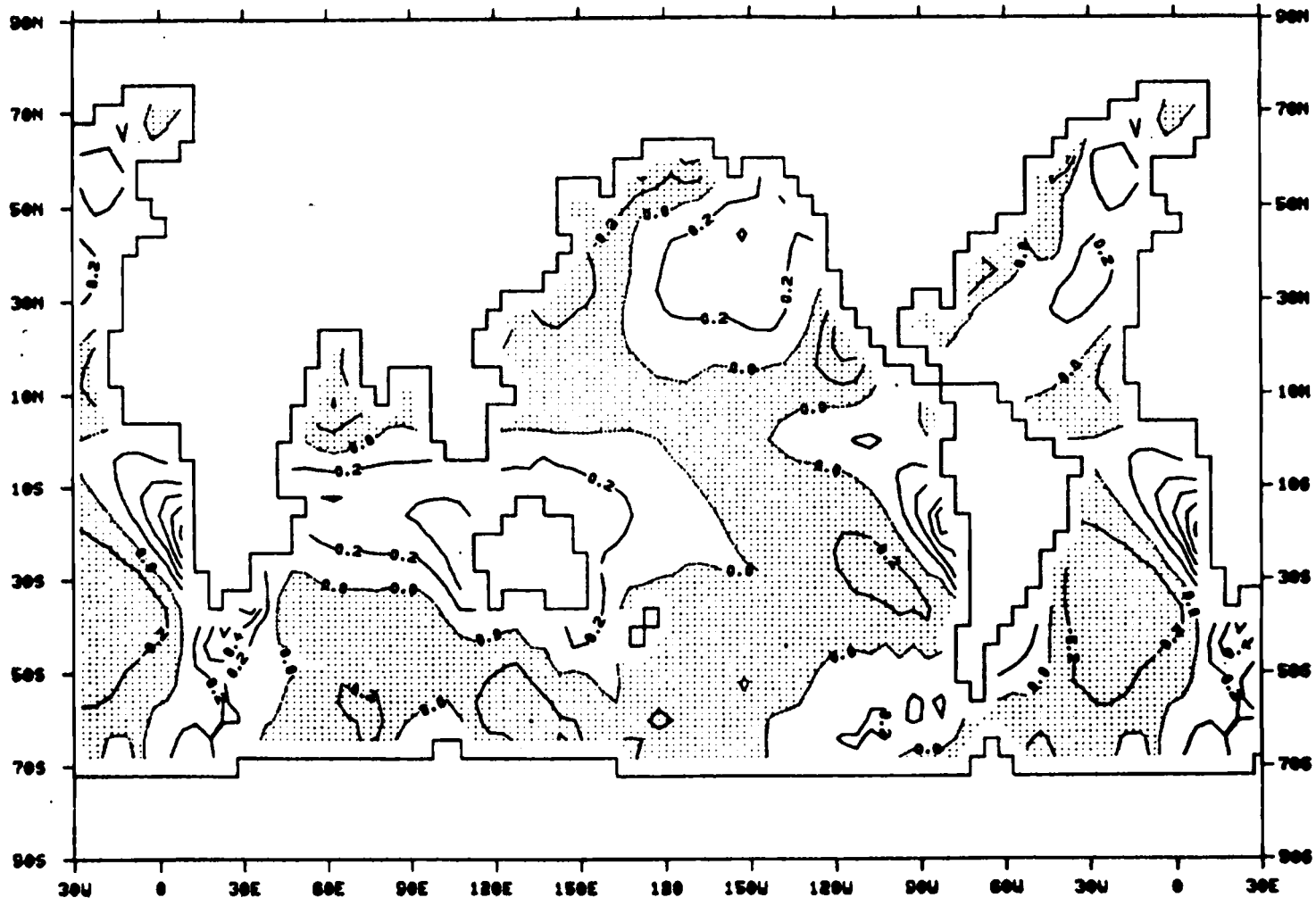


Fig. 2.7. As is Fig. 2.4 except for meridional component.

part of the basin (along the east coasts of the Asian and North American continents). The southern boundary of the positive area is 15 degrees south of the observed (fig. 2.8). The northern boundary, however, is at about the same place. The absolute values are in general slightly larger than observed in the region north of 15N. In the Indian Ocean, the annual mean of observed τ_y is generally positive due to the strong southwesterly summer monsoon. However, the simulated field has a negative value everywhere in this region. The center has a value of -0.4 dyne cm^{-2} which is one of the largest negative values. In the Southern Hemisphere, northward stresses are found mainly over the eastern part of the ocean basins. They are confined in a smaller area with a value larger than that of the observation. The maximum found over the Pacific is 0.90 dyne cm^{-2} compared to the observed 0.58 dyne cm^{-2} . The contrast is small over the Atlantic. Both cases have a maximum of 1.0 dyne cm^{-2} . In the Indian Ocean, the northward stress is much weaker than that of the observation. A maximum of 0.5 dyne cm^{-2} is compared against the observed 1.1 dyne cm^{-2} . The central part of the Pacific between 10S and 30S is dominated by southward stress instead of northward stress as in the observed field. However, the difference in magnitude is small because the stresses in this area are mainly east-west oriented. High latitudes are dominated mainly by westward

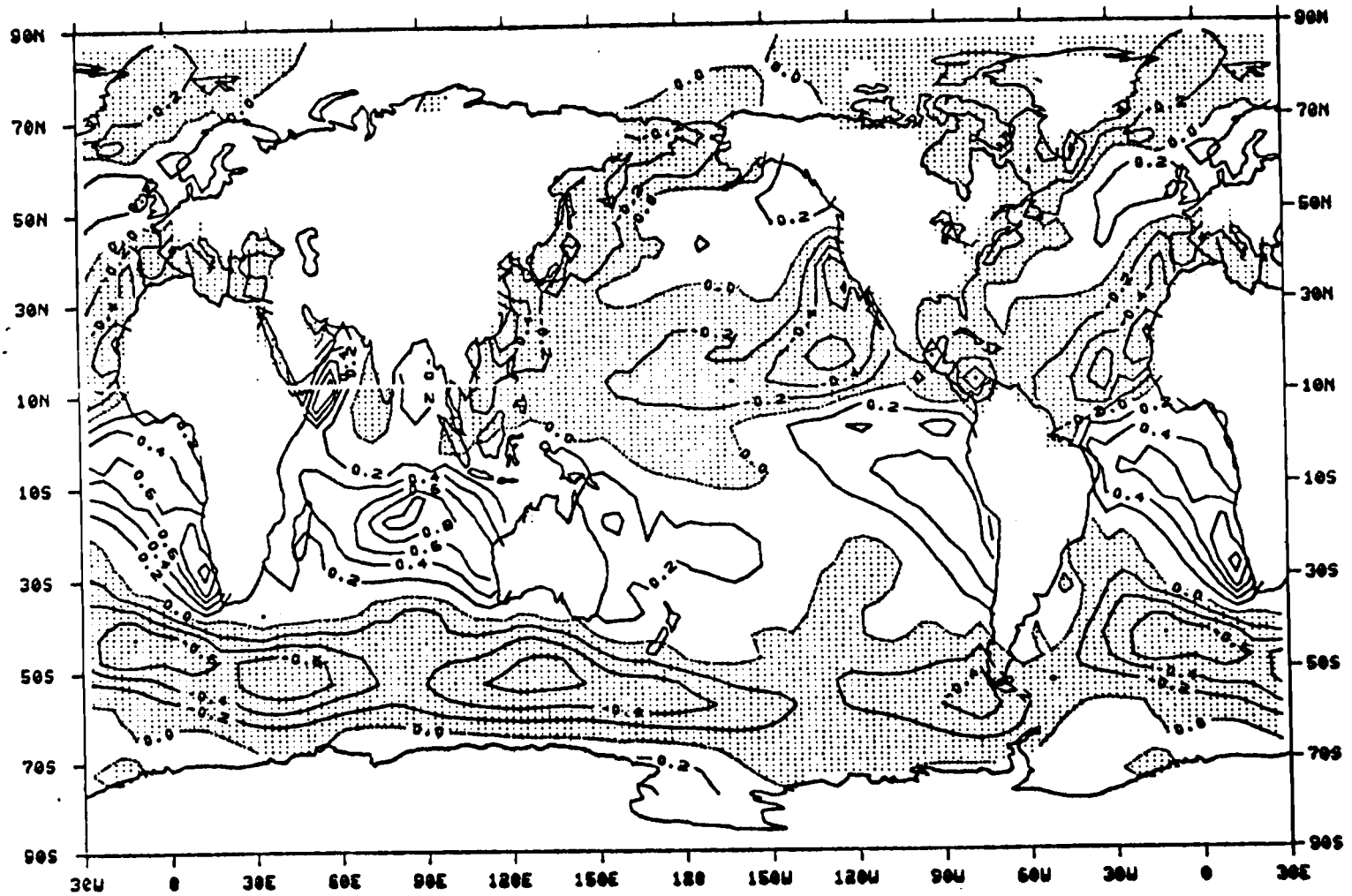


Fig. 2.8. As in Fig. 2.5 except for meridional component.

stress. The distribution of observed τ_y is almost zonal with well defined centers located south of Australia and southeast of Africa. The values at these centers can reach $-0.69 \text{ dyne cm}^{-2}$. In the simulated field, we cannot see the zonal distribution. The simulated magnitudes are much smaller than the observations. Only a very small area has a value over $-0.4 \text{ dyne cm}^{-2}$. Fig. 2.9 shows the zonal means of both cases. As in the zonal component, that the simulated wind stress field suffers phase difference in the north hemisphere and a magnitude difference in the Southern Hemisphere when compared to the observed field.

The wind stress is calculated from the surface wind, therefore the positioning errors of the main gyres in the Northern Hemisphere must result directly from the errors in the wind fields. A comparison between AGCM simulated wind and observed wind at the surface, 800mb ($\sigma = 3/4$), and 400mb ($\sigma = 1/4$) was given by Schlesinger and Gates (1977). The maximum speed of the simulated westerlies did occur equatorward to the observed positions at all levels. The difference is especially evident in July. However, the maximum speed of simulated wind is larger than the observed wind. This contradicts the comparison between two wind stress fields. This could be due to the exclusion of land points in the present study. Also, the comparisons were made against observational data from different sources.

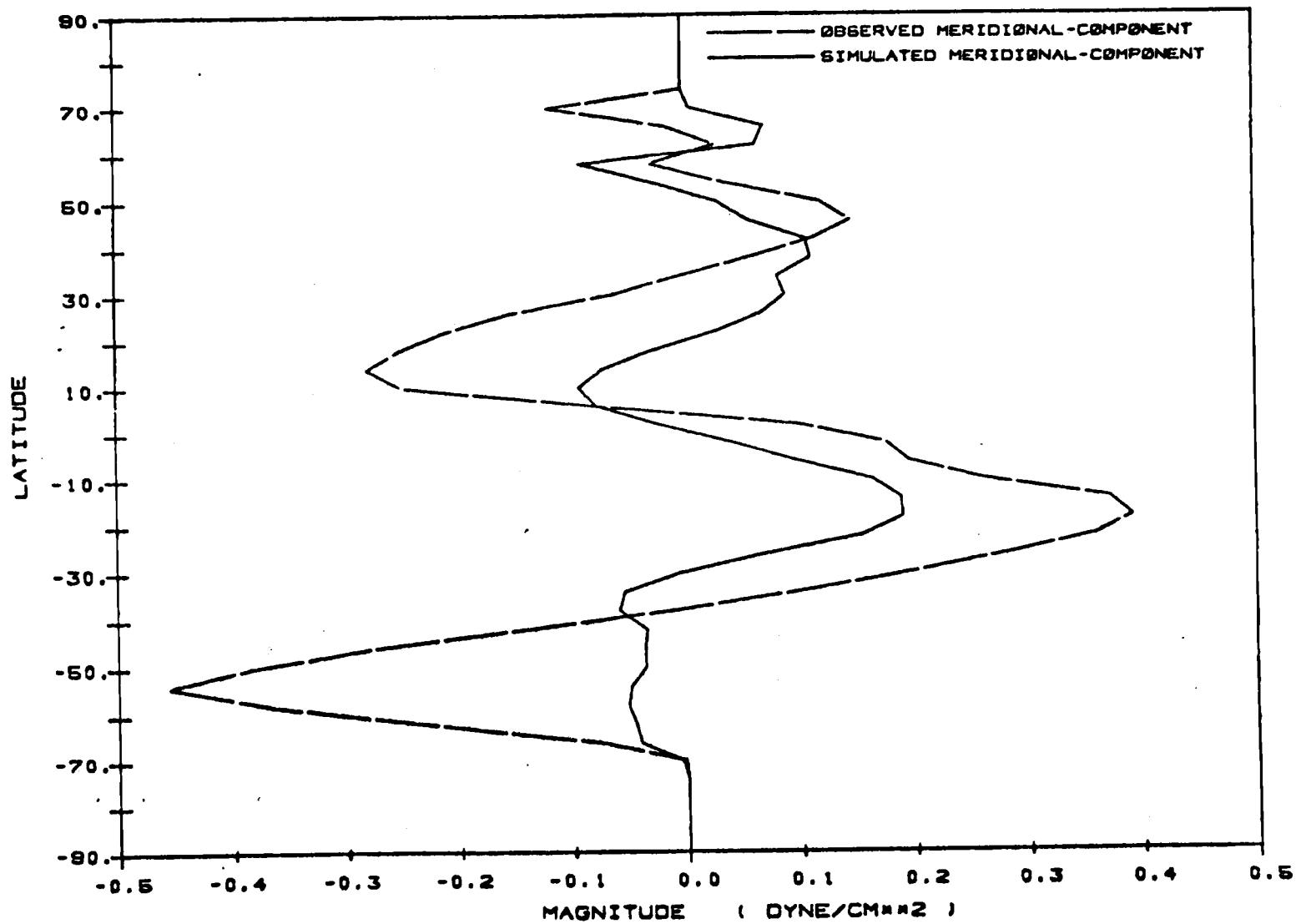


Fig. 2.9. As in Fig. 2.6 except for meridional component.

2.2.4 Curl

The curl of wind stress is crucial in deciding the direction and magnitude of mass transport of the ocean by currents. The relation between the transport and the curl was first derived by Sverdrup (1947):

$$M_y = (\vec{k} \cdot \nabla \times \vec{\tau}_s) / \beta$$

$$= \left(\frac{\partial \tau_y}{\partial x} - \frac{\partial \tau_x}{\partial y} \right) \frac{a}{2\Omega \cos\phi} \quad (2.2.1)$$

where $M_y = \int_0^d \rho v dz$ is the net meridional transport by ocean current; d is equal to or greater than the depth at which the horizontal pressure gradient becomes zero.

Positive (Negative) curl corresponds to northward (southward) Sverdrup transport. Fig. 2.11 shows the global distribution of the observed annual mean stress curl. The curl is approximated as the circulation per area within 5X5 degree boxes whose centers are the corners of Marsden 5X5 degree subsquares. Fig. 2.10 shows the global distribution of the simulated curl field. In the Northern Hemisphere, positive values are found between 27N and 50N (60N in Atlantic). The observed maximum centers along 60N are reproduced at about the same locations except the magnitudes are smaller. As expected from the distribution of the zonal component of the stress, the zero lines also shift south to those of the observation. The northern zero

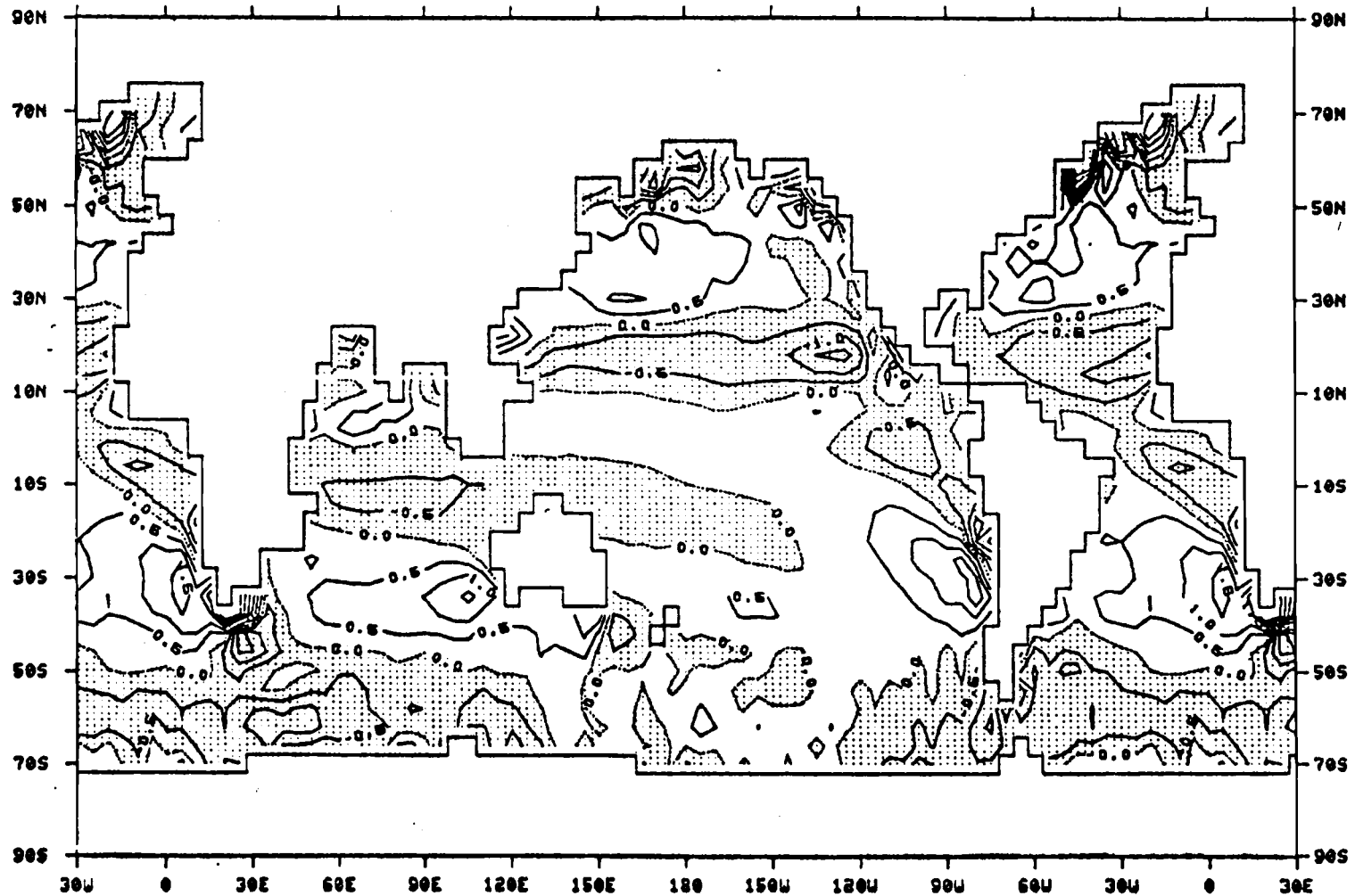


Fig. 2.10. 3-year mean AGCM-simulated wind stress curl. Contour interval is 0.5×10^{-8} dyne/cm². The zero lines are dashed and the negative values are stippled.

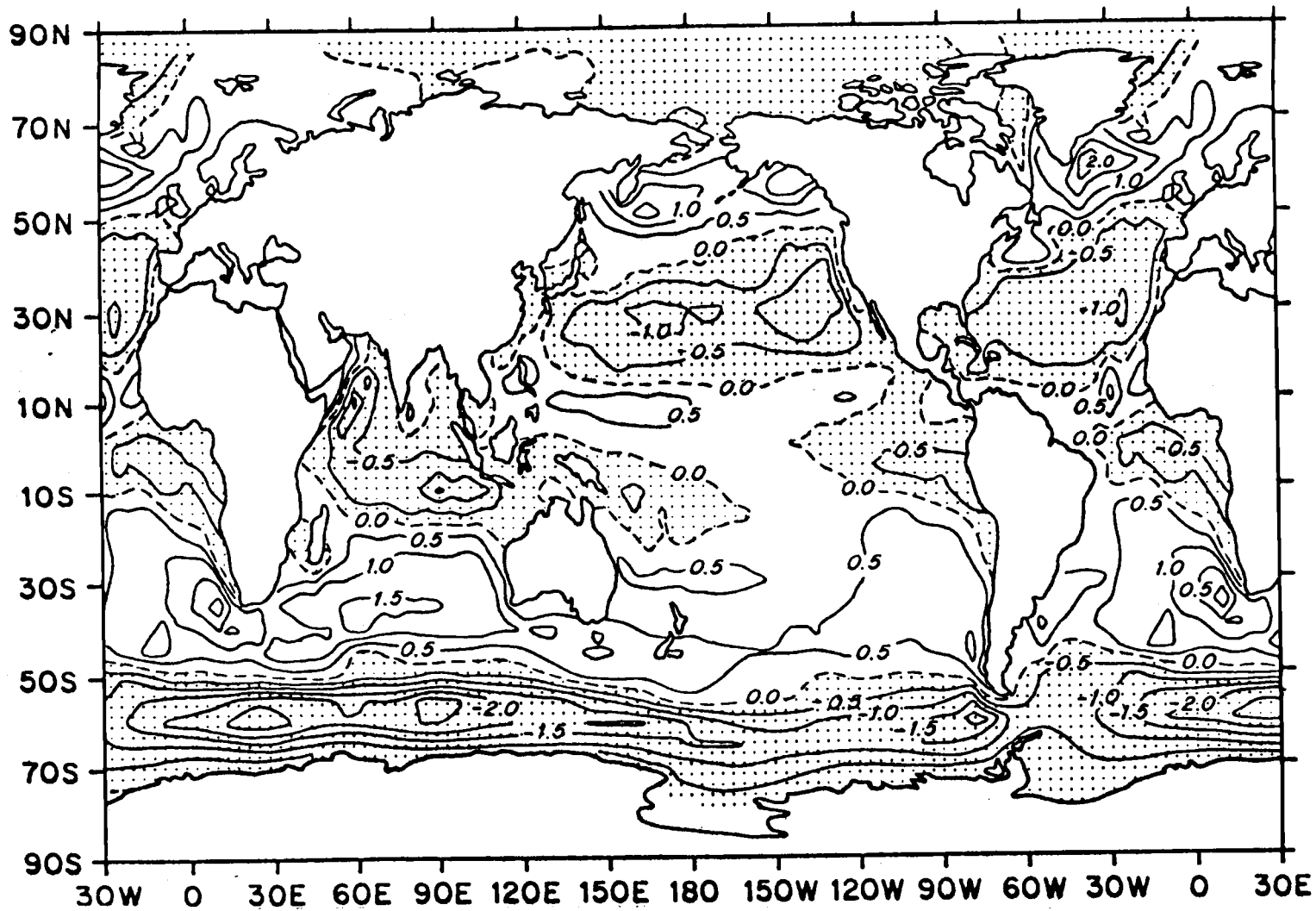


Fig. 2.11. As in Fig. 2.10 except for annual mean observed wind stress curl. (after Han and Lee (1981))

line shifts 15 degrees, and the southern zero line shifts 5 degrees to the south. This causes the negative region to be much narrower than that of the observed field. In the Southern Hemisphere, the pattern agrees quite well with the observations in the area between the equator and 50S. The observed centers over the Indian ocean are also seen on the simulated field, except the value over the Pacific Ocean is smaller (1.0 against observed 1.5 in unit of 10^{-8} dyne cm^{-3}). The distribution beyond 50S is somewhat noisy. We cannot find the zonal distribution as found in the observed field. Fig. 2.12 shows the zonal means of the simulated and observed curl fields. The features described above are clearly illustrated here. We may notice that there seems to be a constant latitudinal phase shift between the zonal mean curves of the curl and the zonal stress component. This is because the meridional variation of the zonal wind stress is the dominant term of the curl's magnitude.

2.2.5 Root mean square

The root mean square (rms) wind stress field gives the spatial distribution of the energy density. Fig. 2.13 shows the rms observed surface wind stress over the North Pacific and Atlantic Oceans, as given by Willebrand (1978). He used four years of observational data up to 1976 to

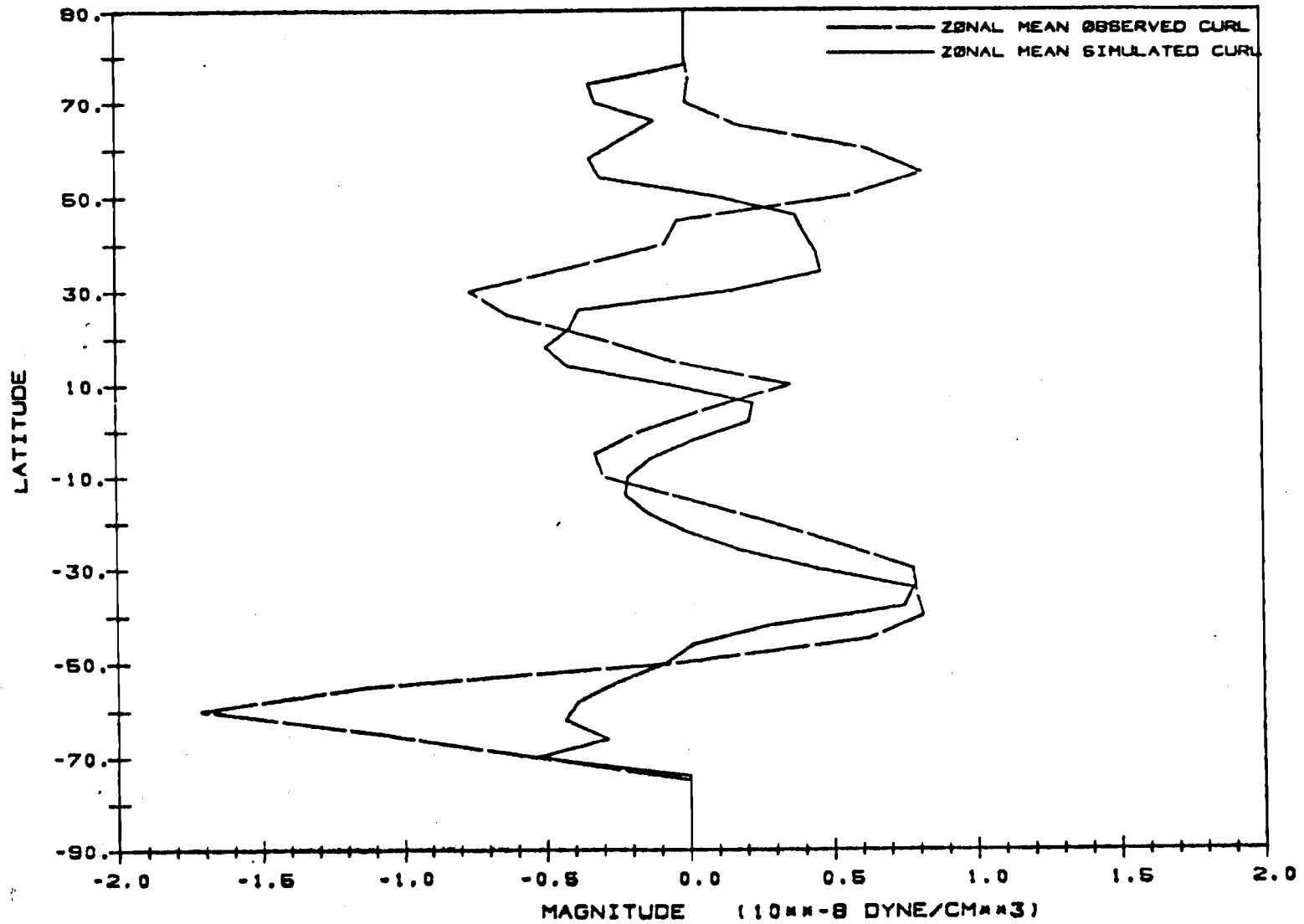


Fig. 2.12. Zonal means of the simulated (solid lines) and observed (dashed lines) wind stress curl.

calculate the surface wind stress and rms stress.

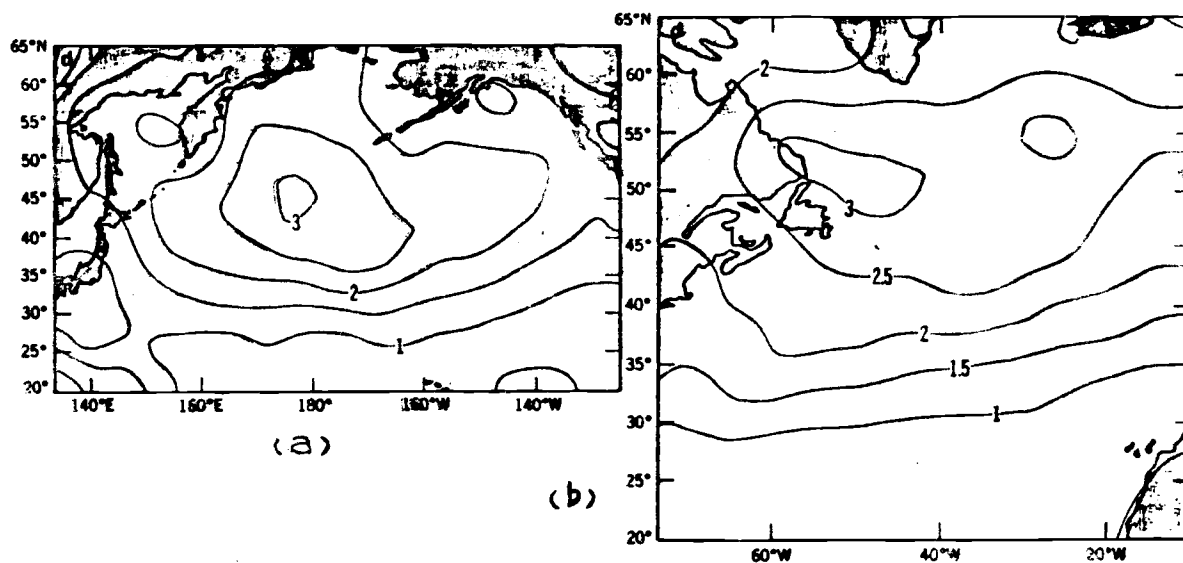


Fig. 2.13. Root mean square observed wind stress over (a) North Pacific (b) North Atlantic Oceans, (after Willebrand (1978))

The typical value varies between 1 and 3 dyne cm^{-2} . Maxima are found southwest of the Aleutian islands near 45N in the Pacific and east of Newfoundland near 50N in the Atlantic. The global distribution of rms simulated wind stress is shown in fig. 2.14. The value between 30N and 30S is generally less than 1 dyne cm^{-2} , with the minimum value being found near the equator. In the northern oceans, the structure of the distribution is a little complicated. The minimum center is found to be at the position where it happens to be a maximum in the observed field. This is due to the southward shift of the cyclonic gyre in the North Pacific Ocean as we mentioned in section 2.2.1. The observed storm track (large rms value) is replaced by the semi-permanent Aleutian Low (small rms

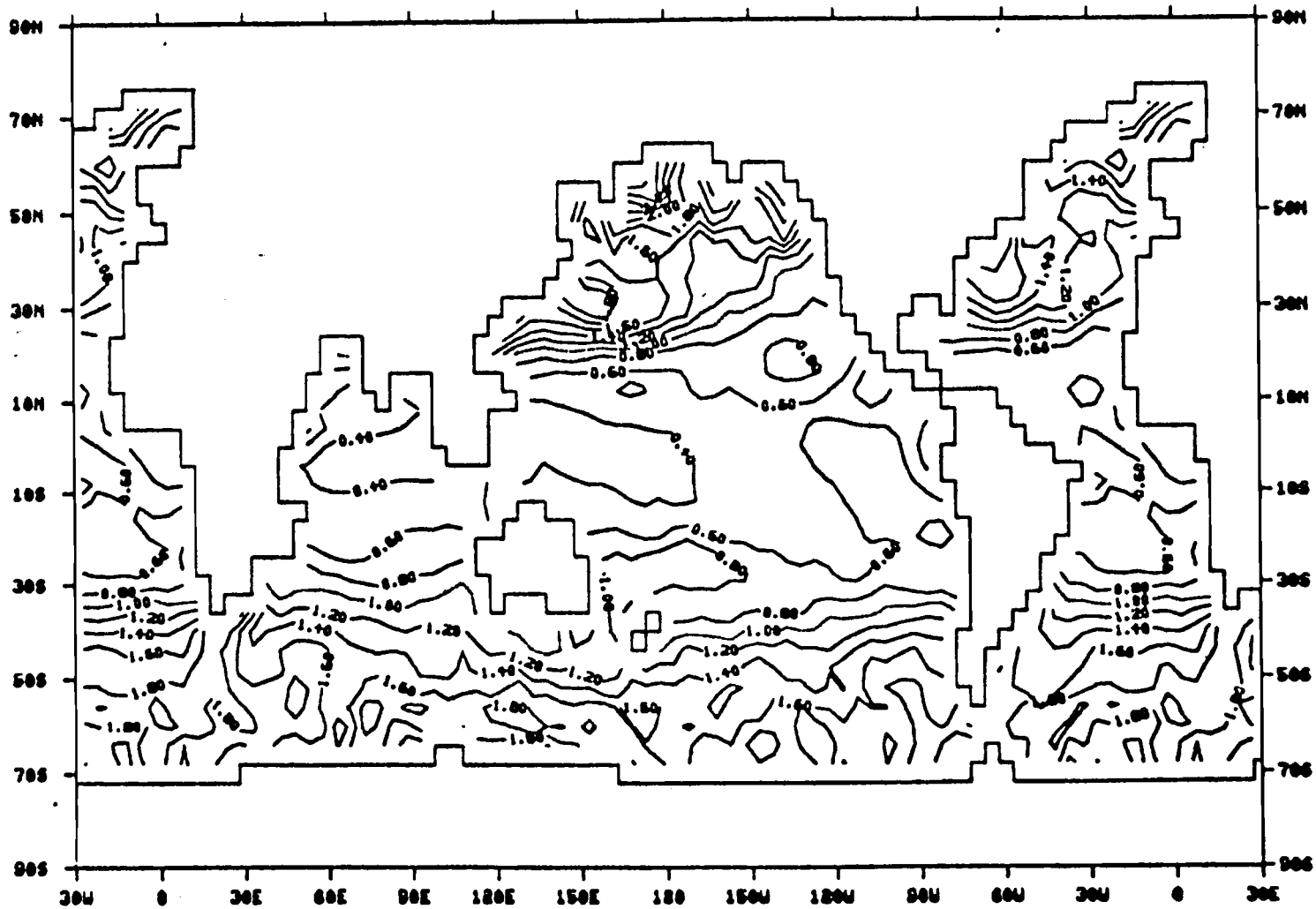


Fig. 2.14. Root mean square simulated wind stress over global oceans. Contour interval is 0.2 dyne/cm . The lines of 1 dyne/cm are dashed.

value) in the simulated field. In the Pacific, maxima are located in the Bering Sea and east of Japan with values 2.8 and 2.1 dyne cm^{-2} , respectively. The value over the Pacific is larger than that over the Atlantic where the maximum value is found to be 1.8 dyne cm^{-2} at locations in North Sea and east of New England.

2.3 Seasonal Variations

2.3.1 Vectors

First, we briefly describe the seasonal change of the observed wind stress field. The study of the monthly mean of zonal stress reveals a seasonal variation which is strongly dependent on latitude as seen in fig. 2.15. The annual variation is the predominant mode for almost all latitudes with exceptions in the northern high latitudes where a weak semi-annual variation predominates and in southern latitudes around 50S and 60S, where distinct semi-annual variation, with maxima in spring and fall, predominates. From the distributions of the monthly mean observed vector field for the 12 months (only January and July are shown in figs. 2.16a,b), we can clearly see the annual variations. The most conspicuous one is associated with the Asian monsoon as seen in the Indian Ocean and west Pacific Ocean. The northeasterly stress prevails during

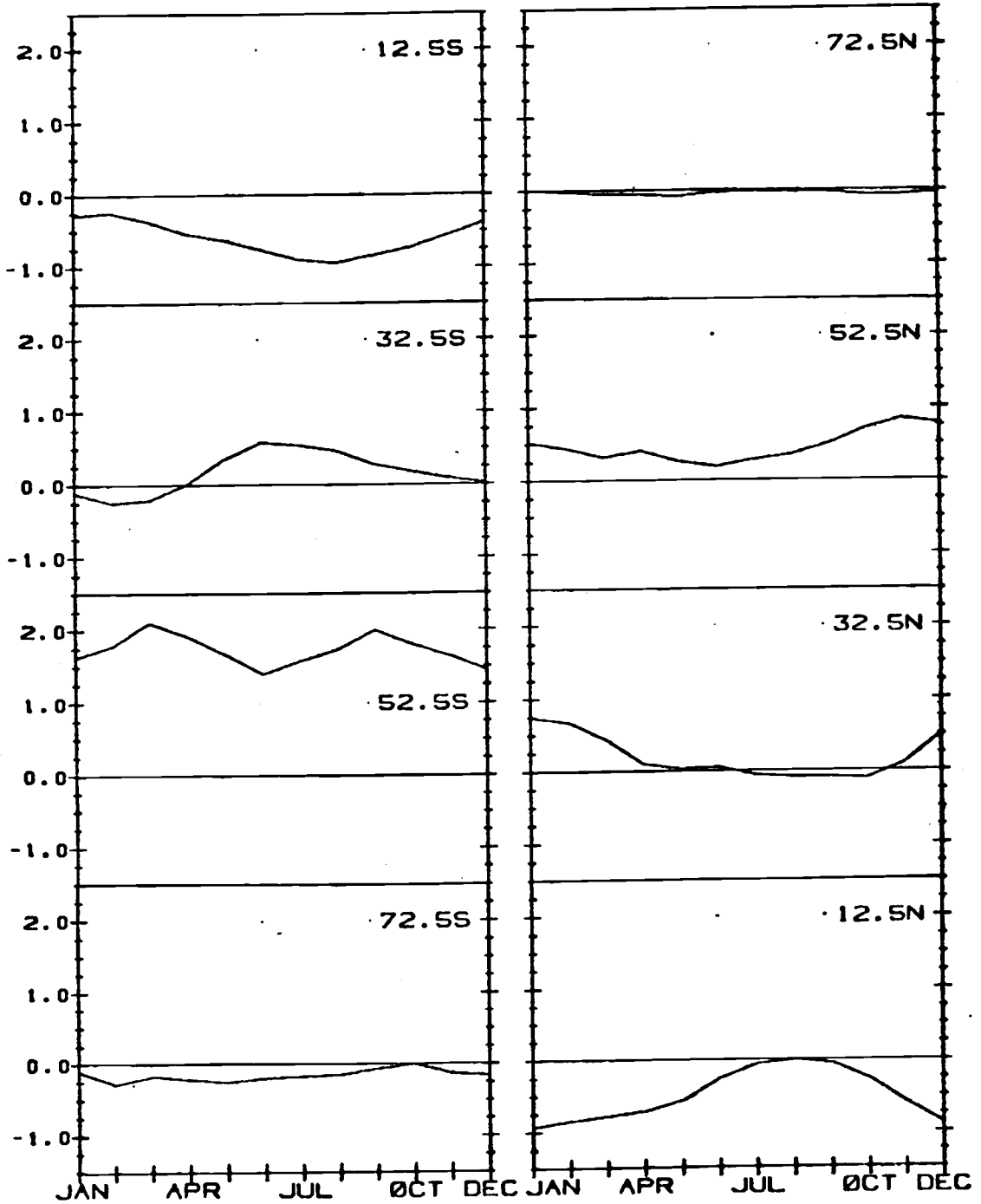


Fig. 2.15. Monthly variation of zonal mean of observed zonal-component of the wind stress. Units are dyne/cm^2 .

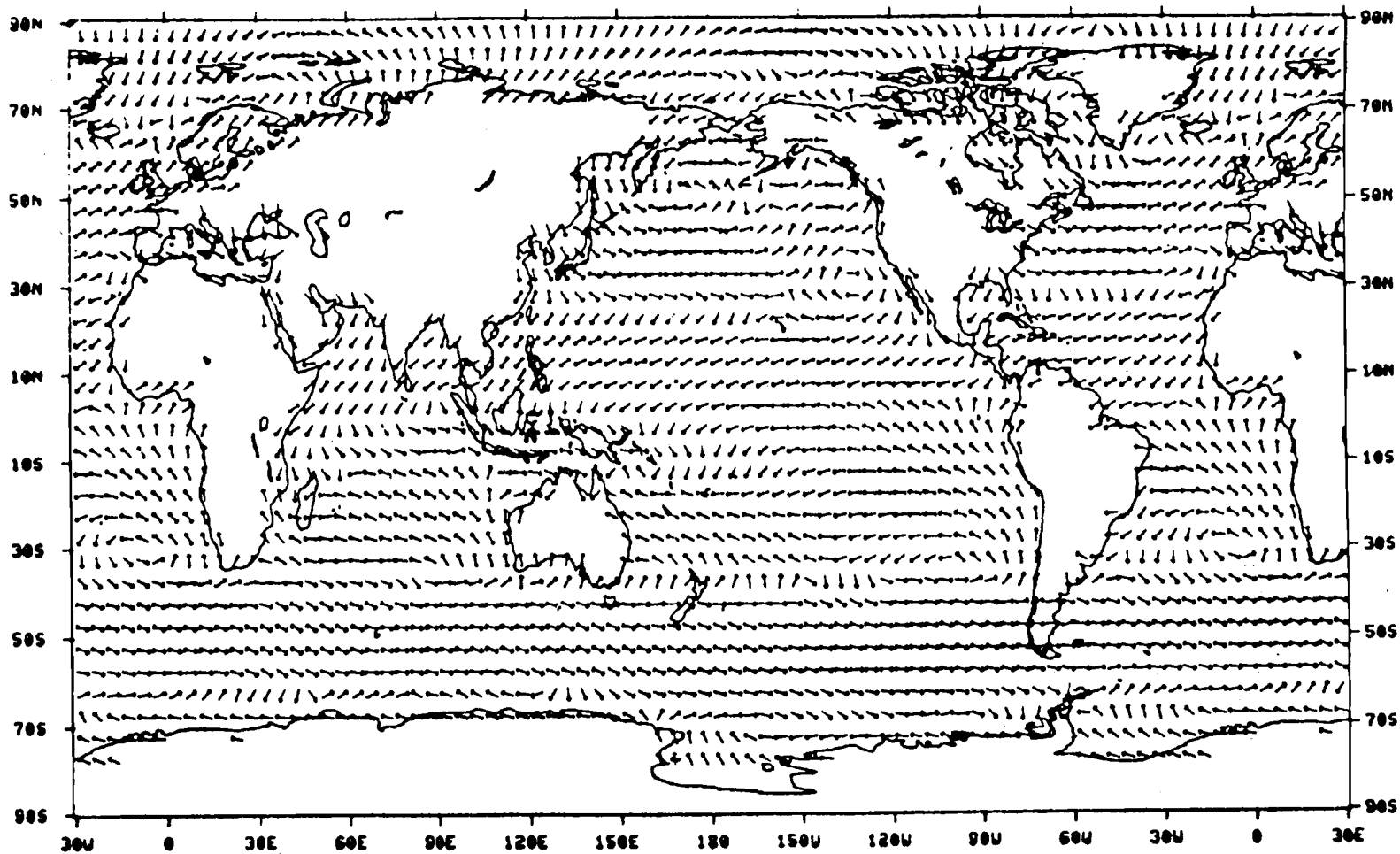


Fig. 2.16a. Mean observed wind stress vectors for January.
(after Han and Lee (1981))

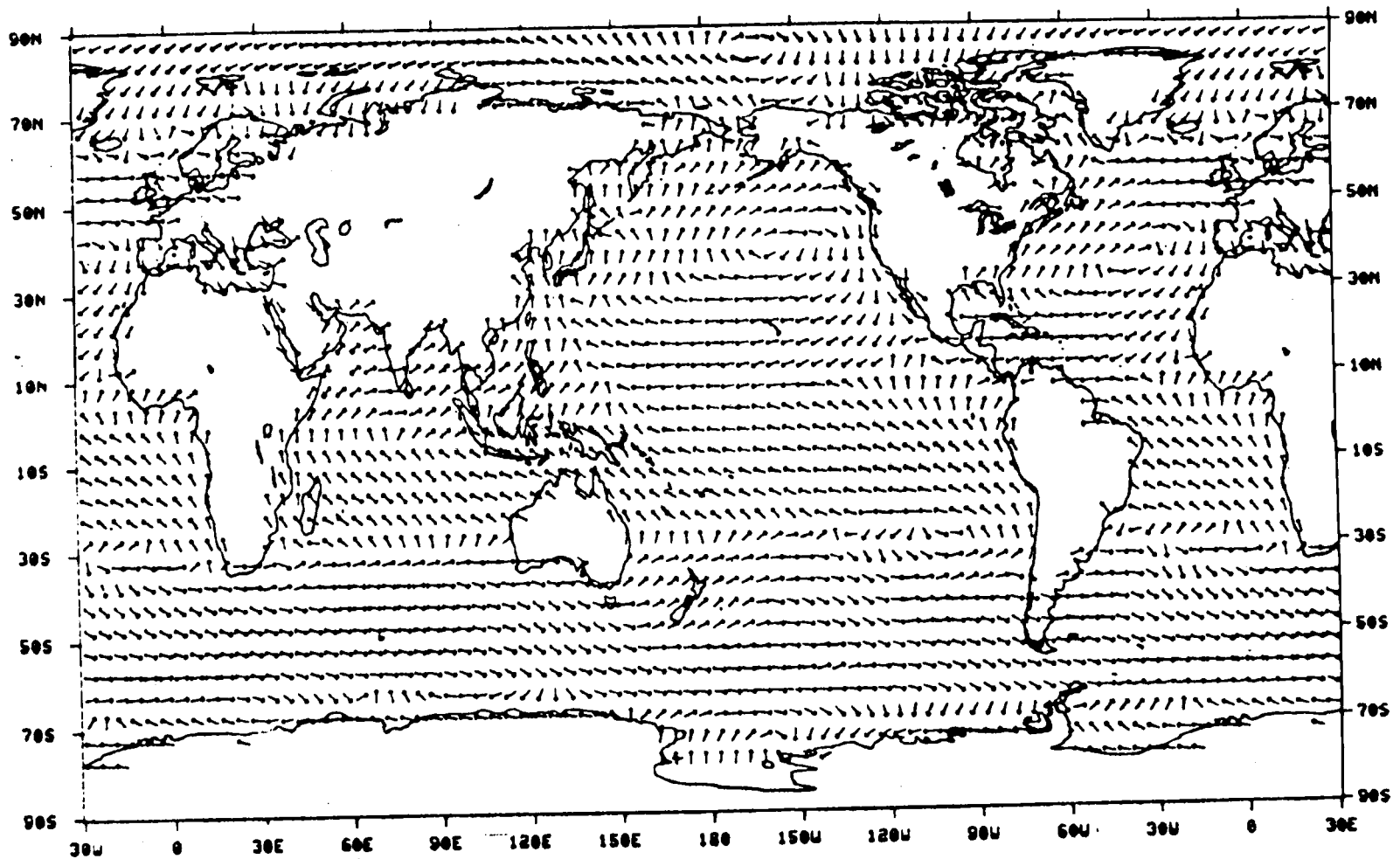


Fig. 2.16b. As in Fig. 2.16a except for July.

November through April, then reverses its direction to become southwesterly in May. The southwesterlies reach their maximum intensity in July and then gradually weaken until October. The anticyclonic gyre in the North Pacific and Atlantic also experience dramatic fluctuations with time while the counterparts in the Southern Hemisphere appear to be semi-permanent.

Fig. 2.17 shows the time variability of simulated zonal stress at latitudes close to those in Fig. 2.15. As in the observed field, the annual variation is the dominant mode for most latitudes. Semi-annual variation is found only at high latitudes in the Southern Hemisphere. The variability is similar to that of the observation at most latitudes. However, some distinct inconsistencies can be found in the high latitudes of both hemispheres. It is interesting to note that at 50N, the pattern is similar to the observed one except the sign is completely reversed. This is due mainly to the southward shift of the westerly stress as described in the previous section.

Figs. 2.18a-d show the distributions of the simulated vector fields of January, April, July, and October. In the Northern Hemisphere, the most conspicuous seasonal variation occurs over the Indian Ocean as mentioned in a previous section. In the simulated field, the

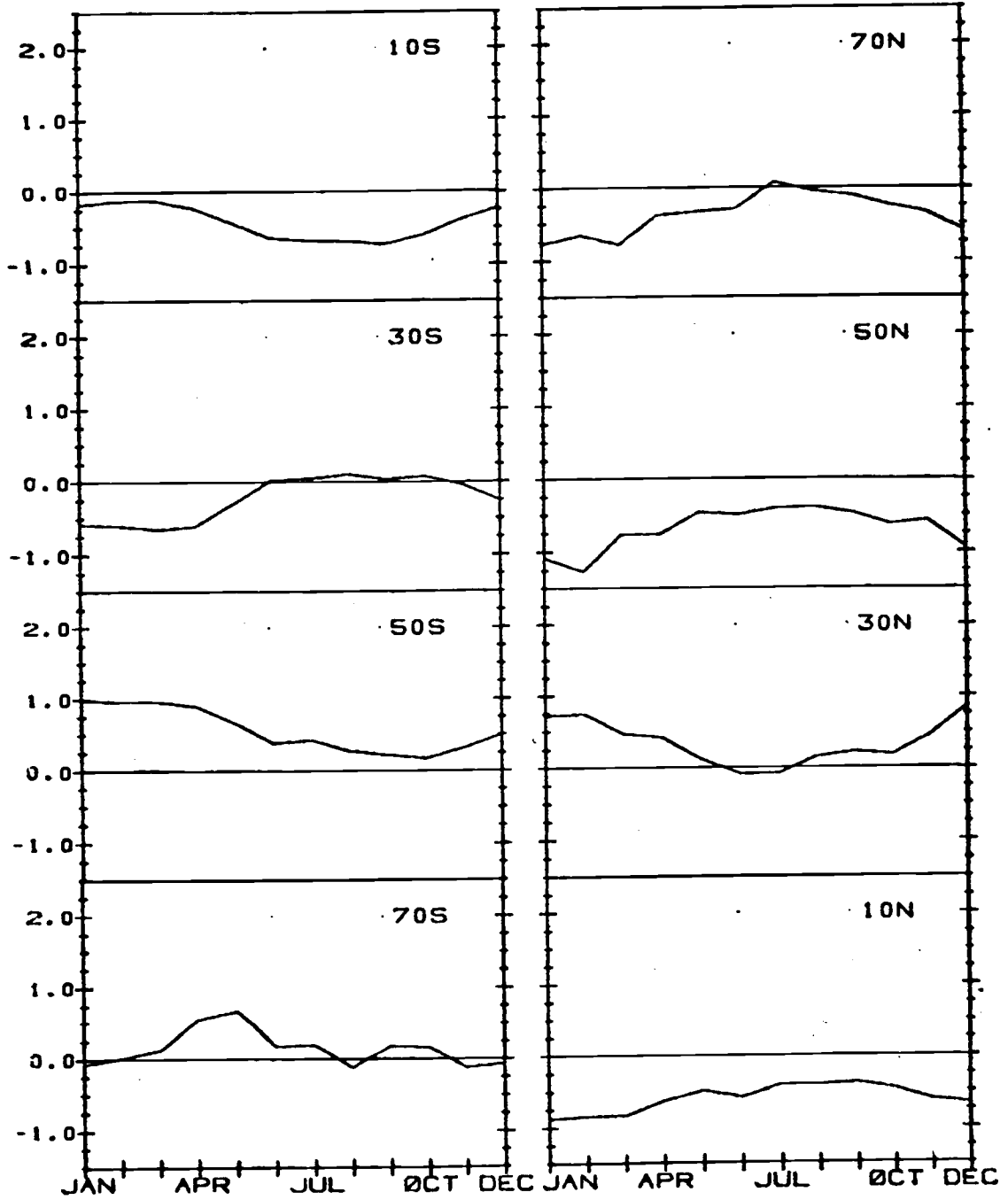


Fig. 2.17. As in Fig. 2.15 except for simulated wind stress.

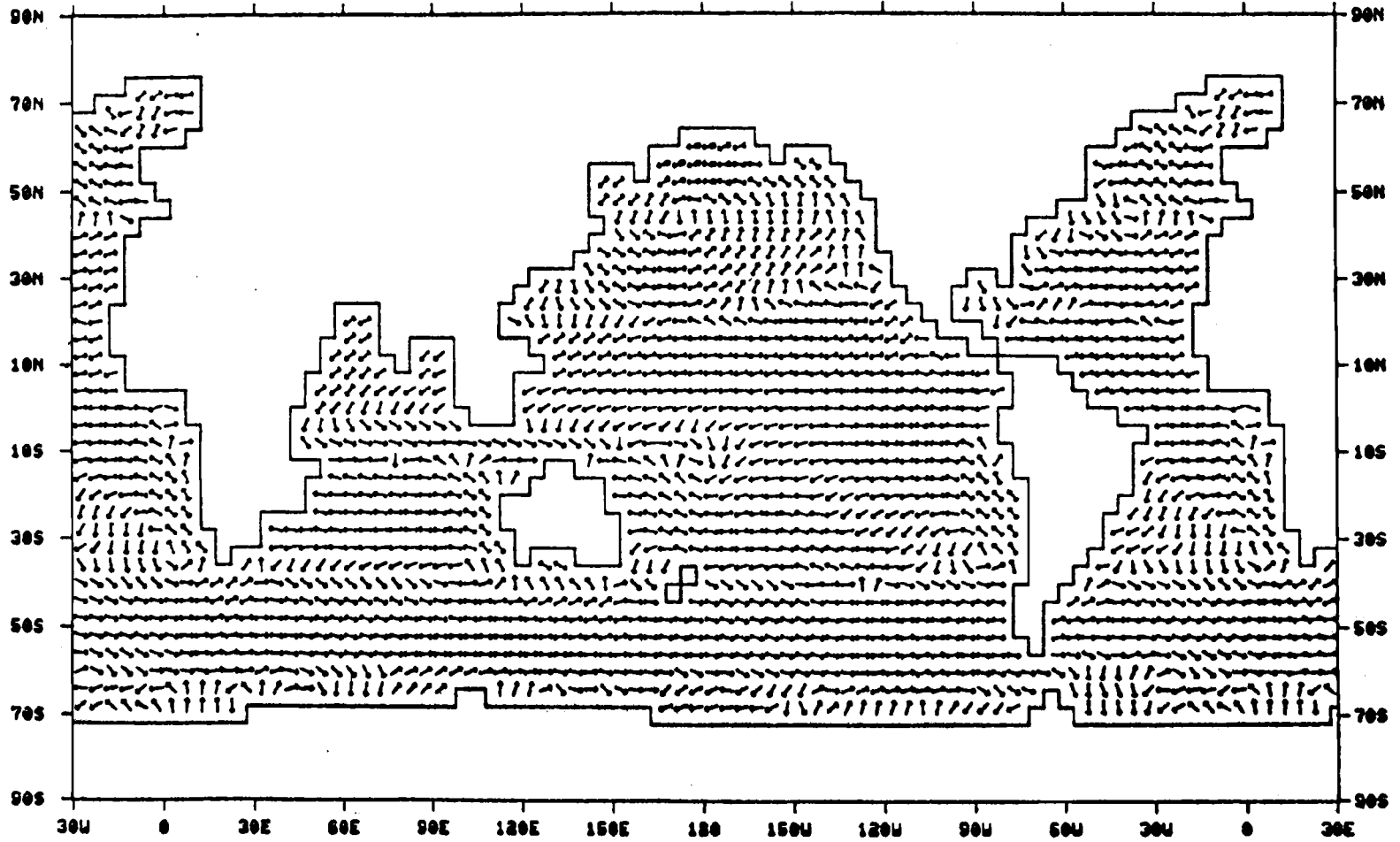


Fig. 2.18a. Mean simulated wind stress vectors for three Januarys.

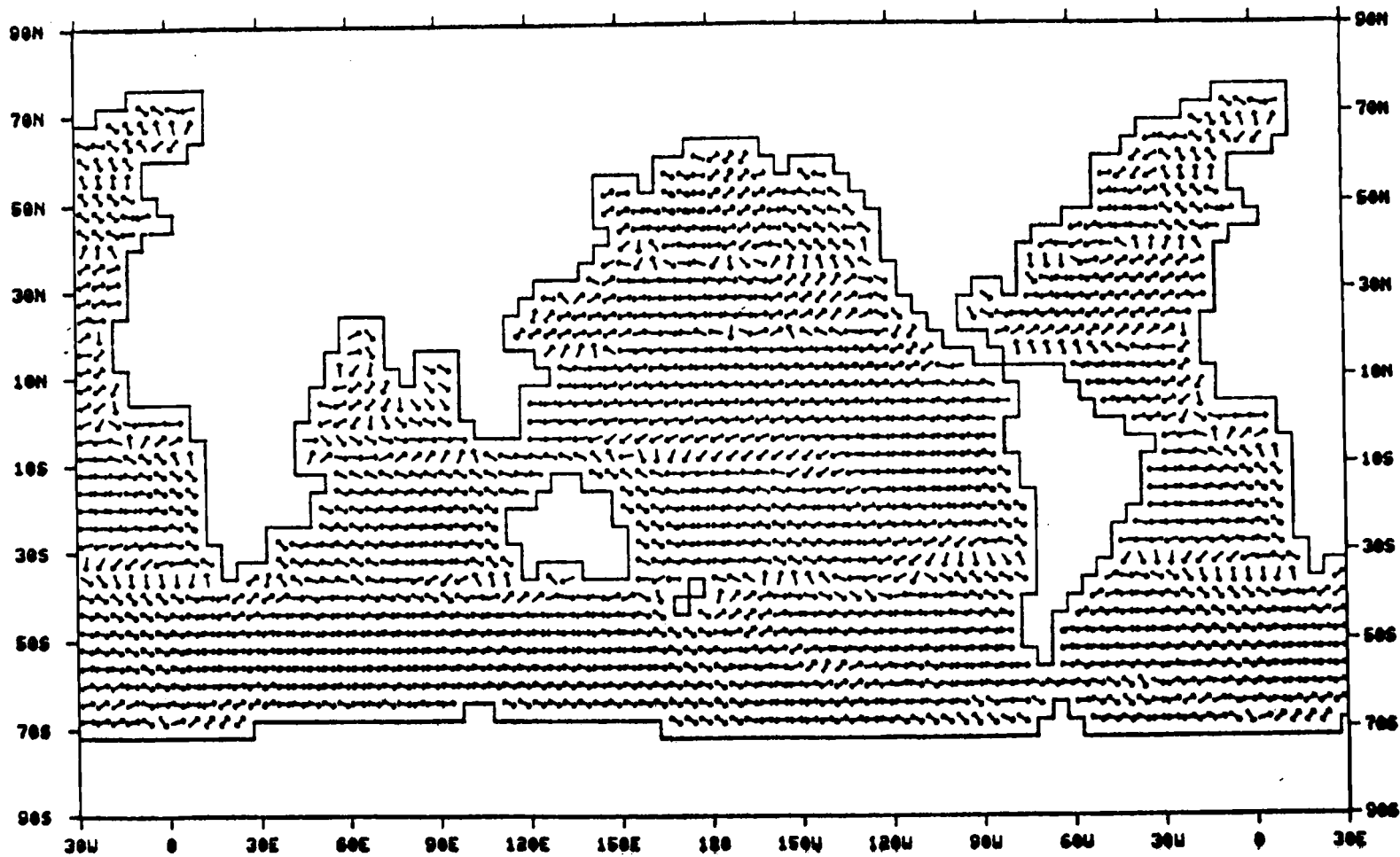


Fig. 2.18b. As in Fig. 2.18a except for April.

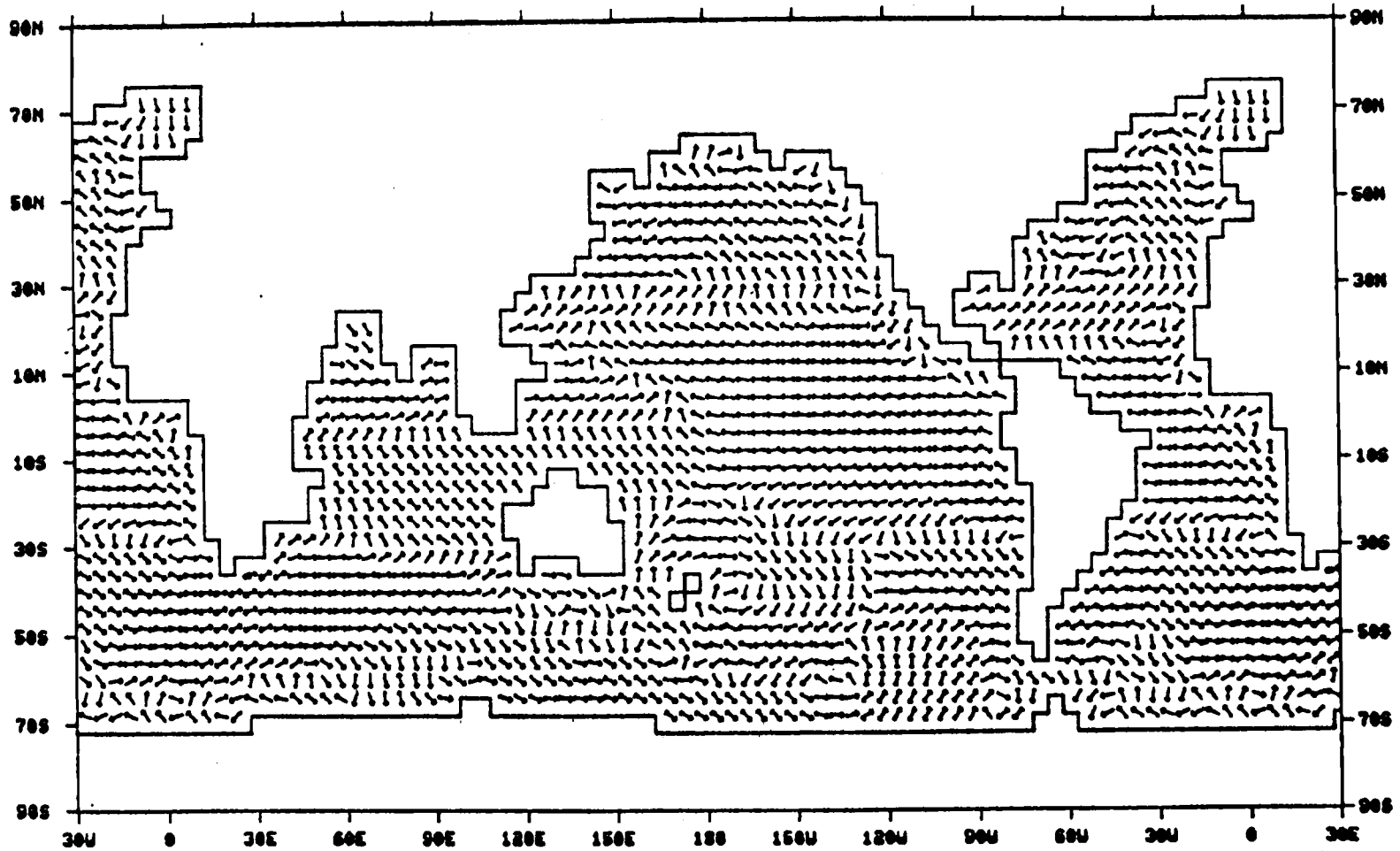


Fig. 2.18c. As in Fig. 2.18a except for July.

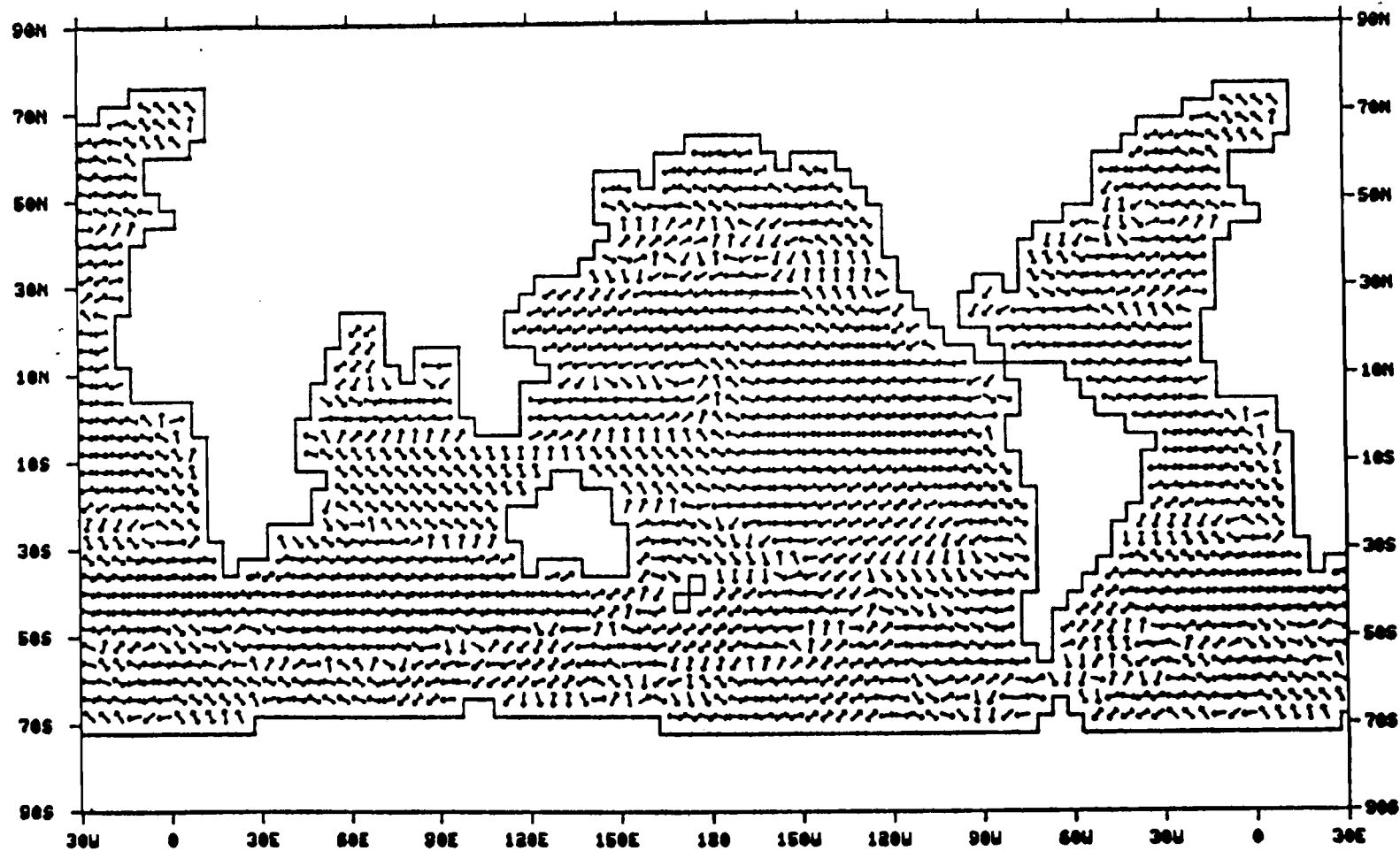


Fig. 2.18d. As in Fig. 2.18a except for October.

northeasterly stresses in winter gradually turn counterclockwise to northwesterlies as the season goes into summer, but never reach southwesterlies as found in the observed field. This has caused the annual mean wind stress vectors to have an almost opposite direction to those of the observed stress over this area. In the Pacific Ocean, the cyclonic gyre changes its position from month to month. The center of the cell is found at 45N in January, and at 30N in July. The simulated anticyclonic gyre, which is the dominating mode in the observed field, is never found to be well shaped throughout the year. In the Atlantic Ocean, the cyclonic gyre also migrates southward from 45N in winter to about 35N in summer. The anticyclonic gyre is found only during the summer season with its center near 23N. In the Southern Hemisphere, the anticyclonic gyres in the eastern part of the ocean show very little variation with time. In the Indian Ocean and east of Australia, the nearly zonal stresses in January turn clockwise to become northward in July. Because of this northward flow, a distinct cyclonic cell is formed east of New Zealand in June. It lasts throughout the southern winter and gradually fades as the northward stress turns back to zonal again. It is obvious that the wind stress field in the Southern Hemisphere behaves more in accordance with the observed field with time than in the Northern Hemisphere.

2.3.2 Curl

By examining the monthly mean observed curl fields (only January and July are shown in figs. 2.19a,b), one finds that the most dramatic seasonal variation occurs again in the Asian monsoon area, where a large negative value in summer can change to a weak positive value in the winter. In the Pacific and Atlantic Oceans, the boundary between positive and negative values remains almost unchanged throughout the year, but the magnitude does change from season to season, indicating a variation in strength but not in direction of the transport during the year. In southern oceans, temporal fluctuation of the stress curl are relatively weaker than those in northern oceans. Variation is found only in the pattern but not in the magnitude. The time variations in the tropical ocean are small, yet it is significant because of the rapid response of the ocean to the wind stress due to the small Coriolis parameter.

Figs. 2.20a-d show the simulated curl fields for January, April, July, and October. In the Northern Hemisphere, the curl in January is generally positive over the Indian Ocean and gradually changes to negative in summer. However, the negative value remains small, compared to the observation, due to the model's failure in

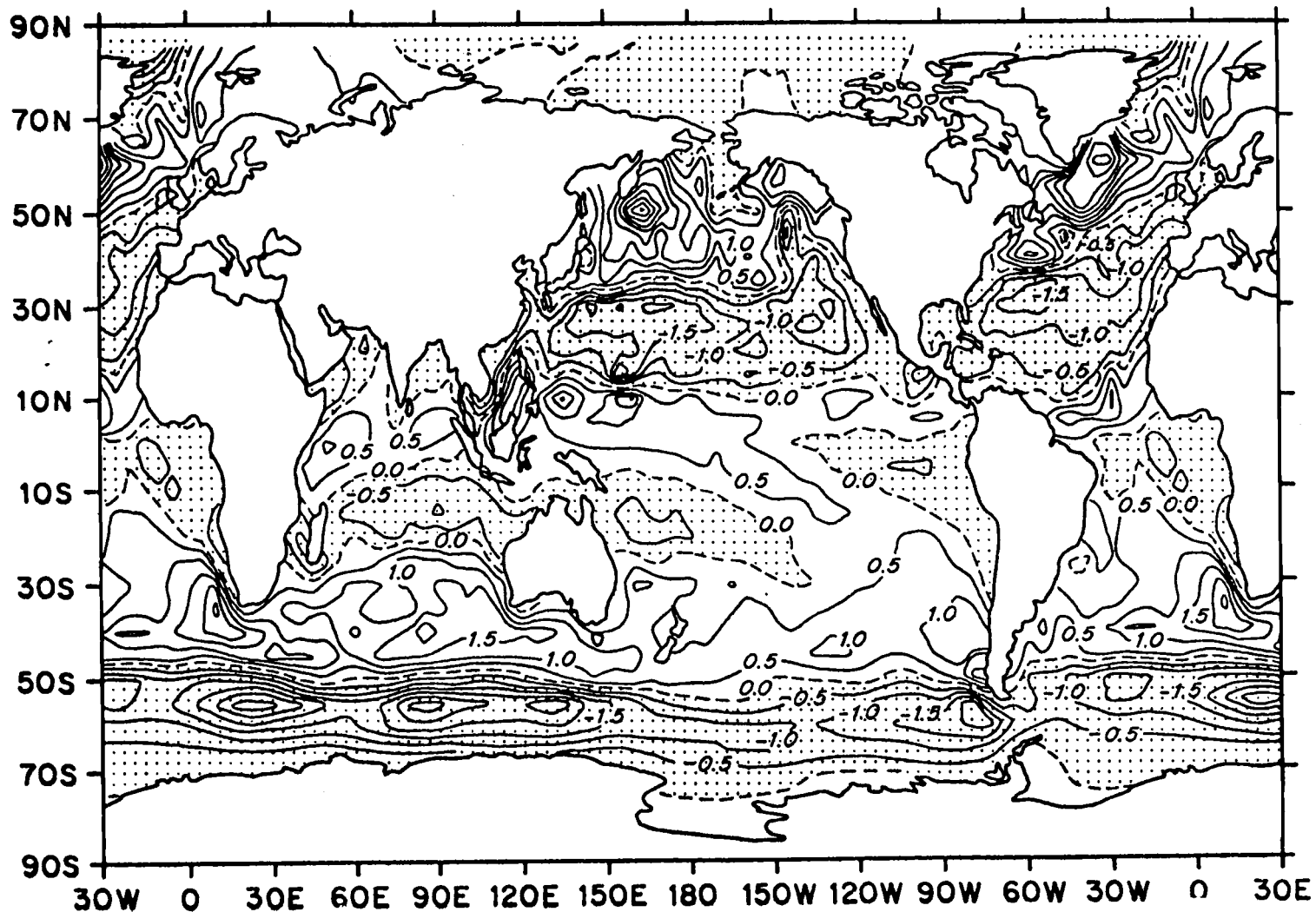


Fig. 2.19a. Mean observed wind stress curl for January. Contour interval is 0.5×10^{-8} dyne/cm². The zero lines are dashed and the negative values are stippled. (after Han and Lee (1981))

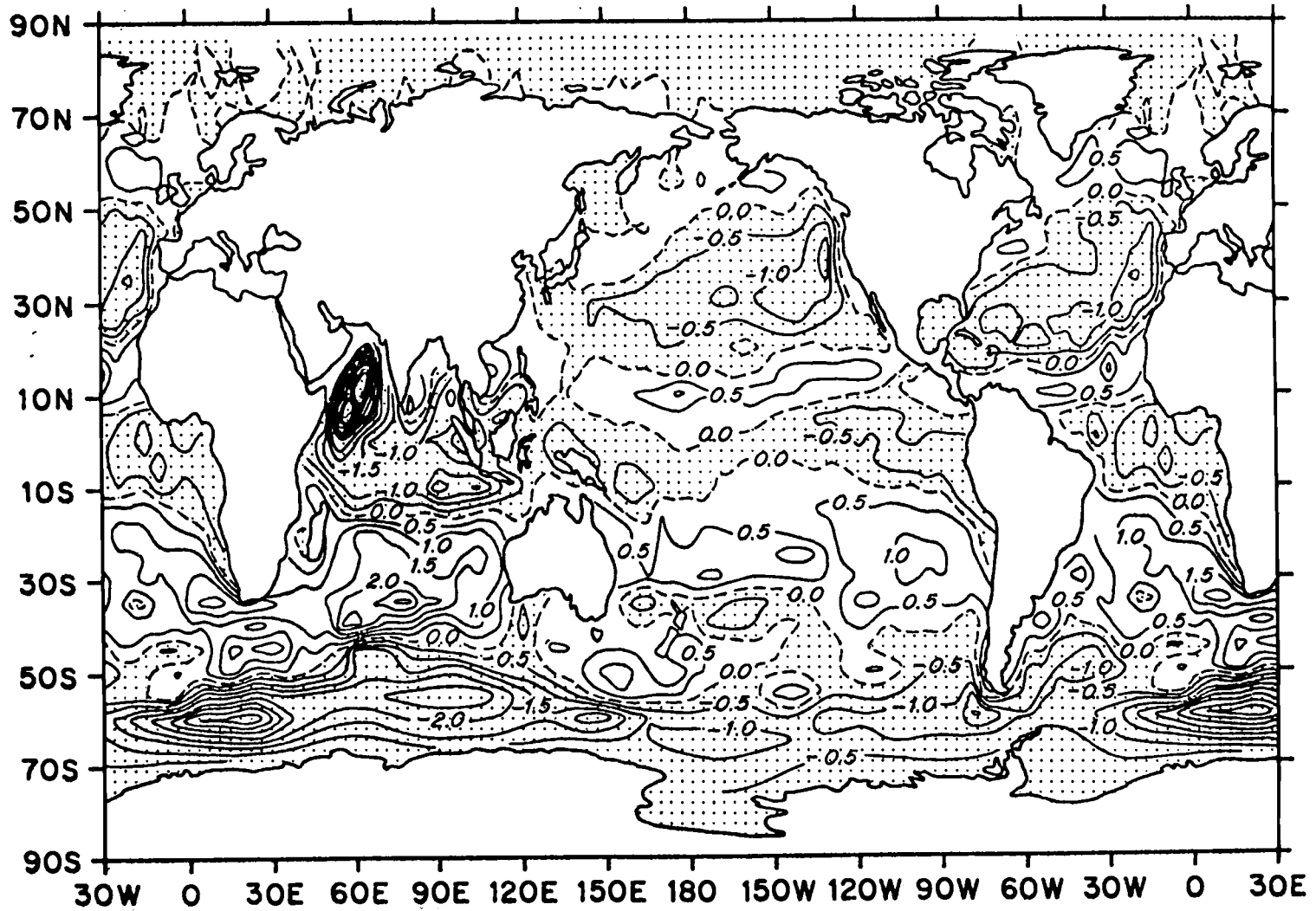


Fig. 2.19b. As in Fig. 2.19a except for July.

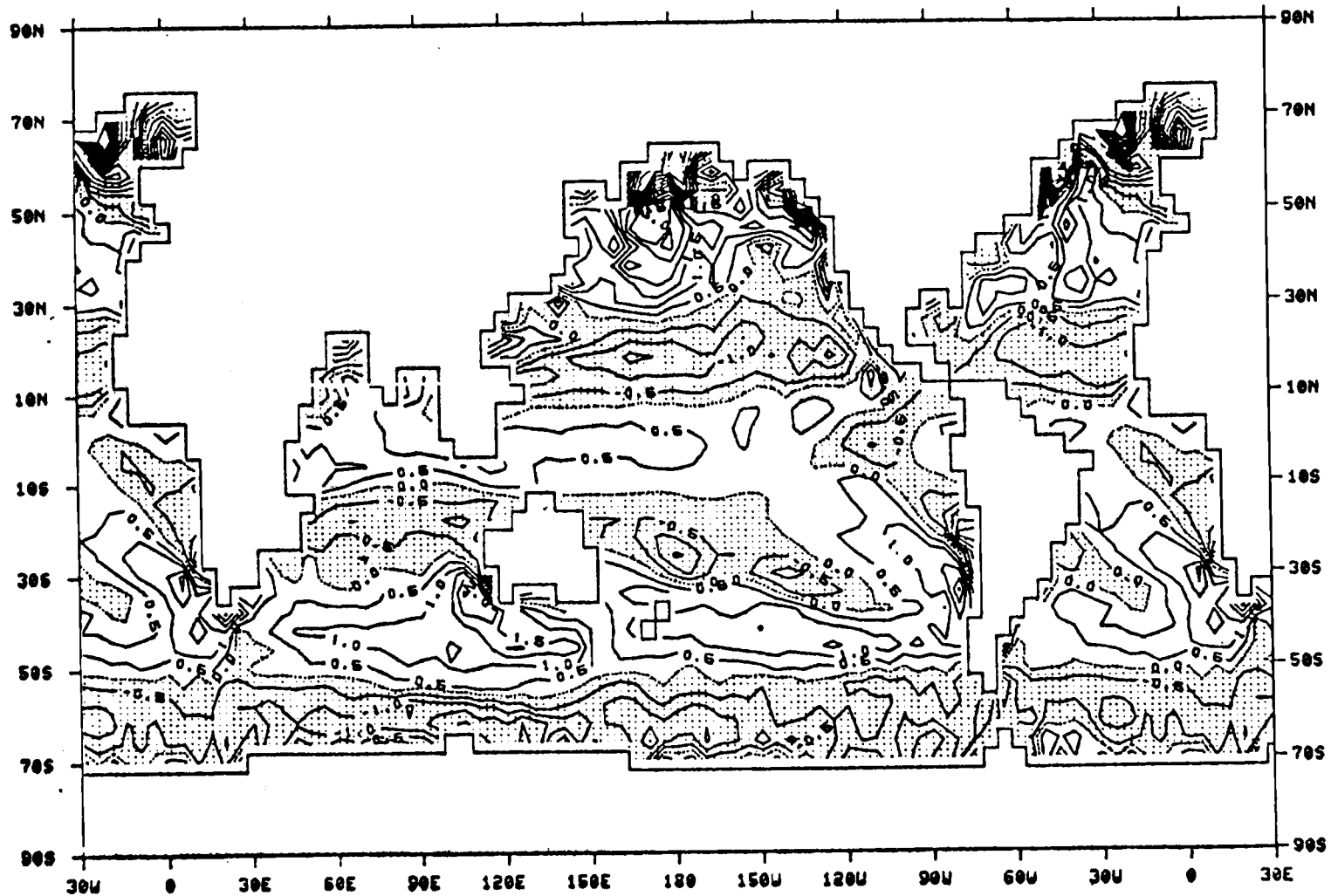


Fig. 2.20a. Mean simulated wind stress curl for three Januarys. Also see Fig. 2.19a.

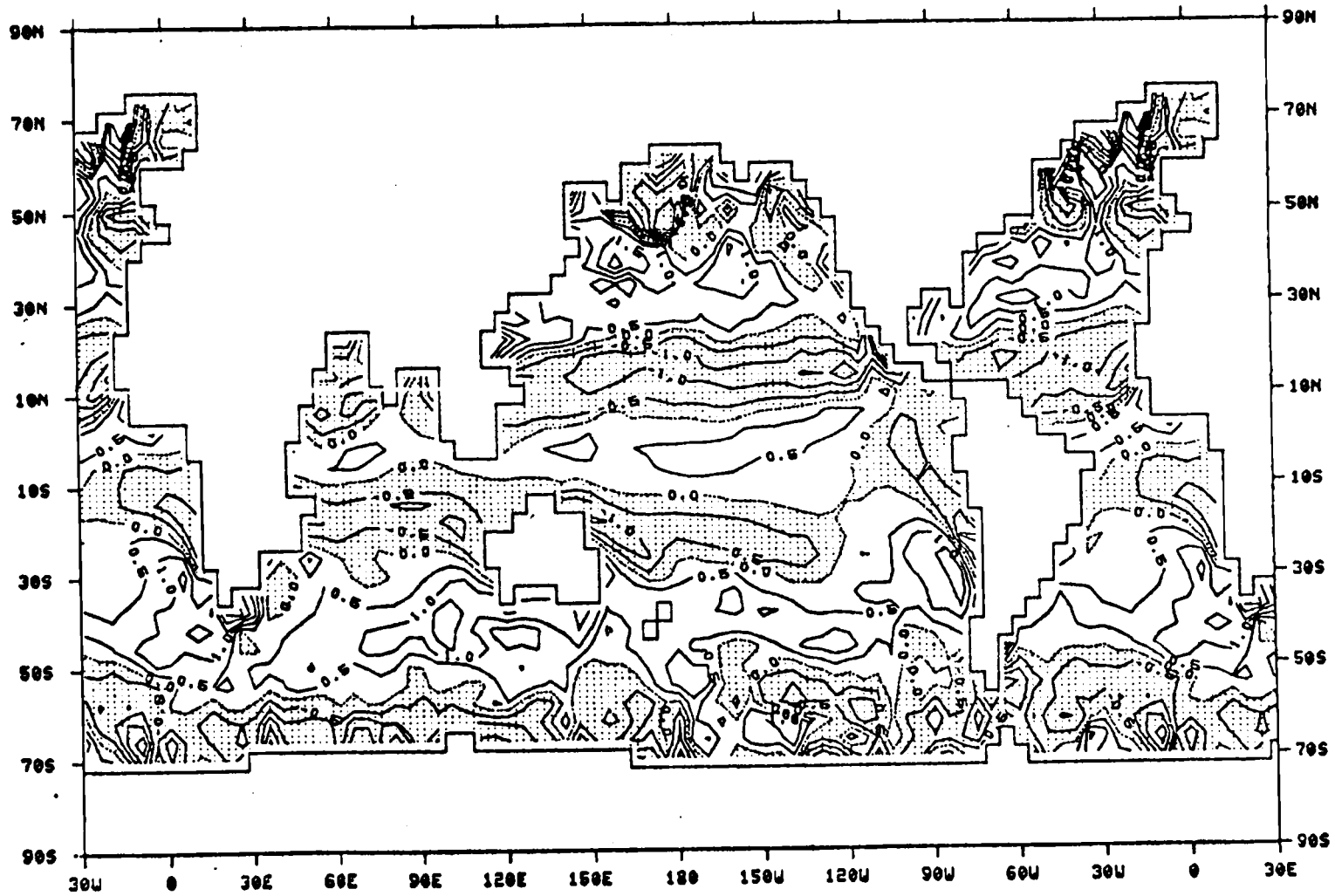


Fig. 2.20b. As in Fig. 2.20a except for April.

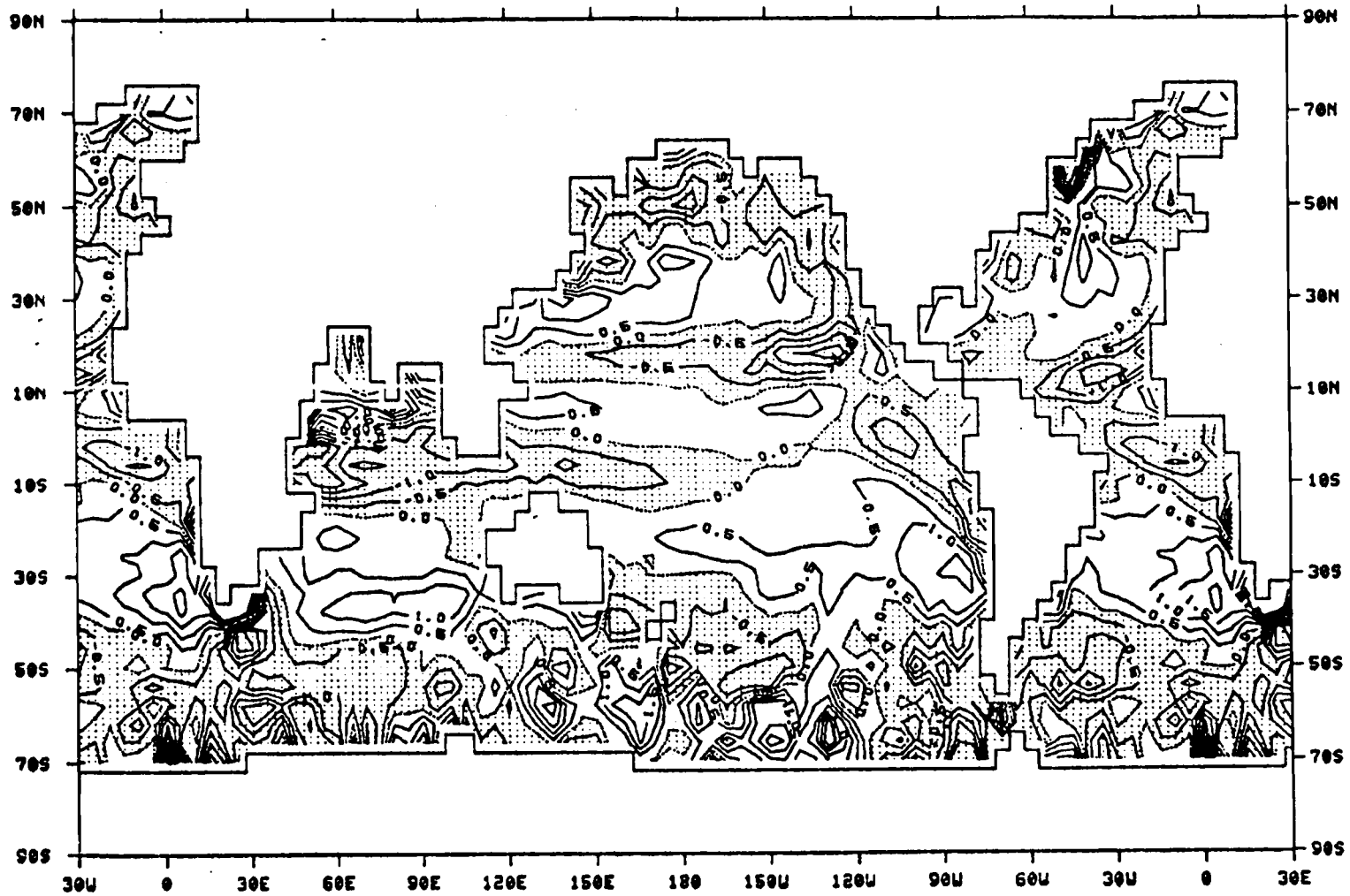


Fig. 2.20c. As in Fig. 2.20a except for July.

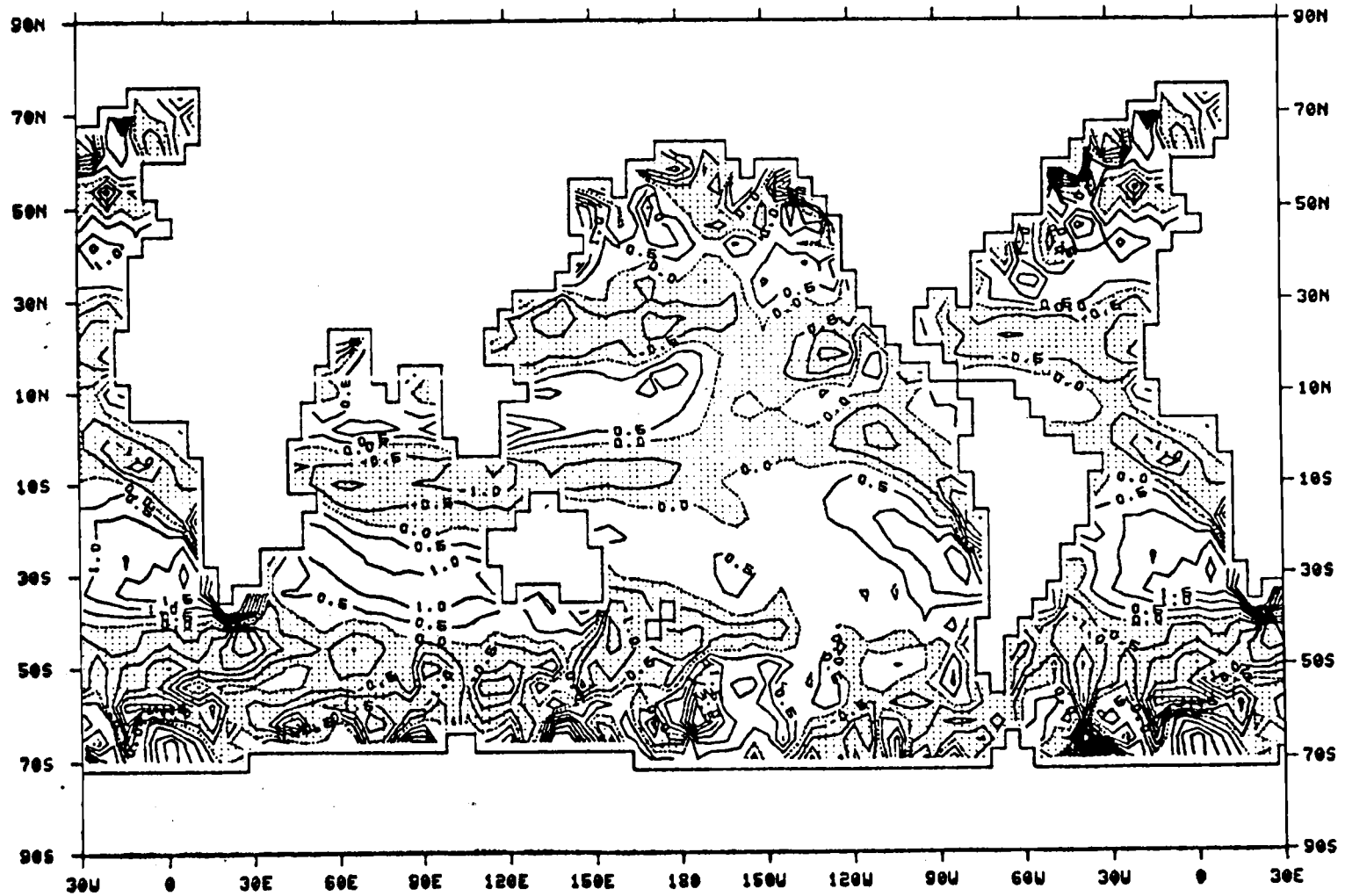


Fig. 2.20d. As in Fig. 2.20a except for October.

simulating the strength of the summer monsoon over the Indian Ocean. In the Pacific and Atlantic oceans, the positive area shifts about 10 degrees to the south from winter to summer as a result of the seasonal migration of the main gyre over the oceans. In the Southern Hemisphere, the curl fields over the Atlantic and east part of the Pacific ocean have little variation with time. Over the Indian Ocean, the negative region between 10S and 30S in January shifts about 15 degrees to the north in July and the maximum value reaches -2.0 compared to -1.0 in January. In the west Pacific Ocean, the variation is also distinct. The sign of the curl is reversed almost everywhere as seasons changes from summer (southern) to winter. This results from the change of flow pattern due to the building up of the cyclonic cell east of New Zealand in winter. Another significant variation can be found at the southern tip of Africa, where the magnitude of the curl becomes very large in winter. As in the observed fields, the time variability in the tropical area is small both in magnitude and pattern. The large values near the northern and southern boundaries are statistically unstable due to the relatively short period of sampling, and hence they will be smoothed out when averages are taken over longer time period of simulation.

3. SPECTRAL ANALYSIS OF SIMULATED WIND STRESS

In the last chapter the spatial characteristics of the AGCM simulated wind stress, in terms of mean fields and root mean square fields, have been reviewed. We will now examine the temporal characteristics of the wind stress by means of spectral analysis of the 3-year time series. This technique allows computation of the contribution to the total variance at various frequencies. In this study, periods ranging from 12 hours to one year are resolved in the autospectral analysis. The cross spectra between pairs of selected quantities are also calculated. This will allow the examination of the relationship between pairs of quantities at various frequencies, and will also provide information about the spatial scales and directional properties of disturbances.

3.1 Autospectral analysis

3.1.1 Algorithm and method of calculation

The raw time series consists of 4380 data points with a uniform time interval of 6 hours. It is divided into 11 segments of six-month length each. The autospectrum is calculated for each segment according to the definition in Jenkins and Watts (1968, hereafter referred to as JW). The

spectral estimates are then averaged over the 11 segments.

For a stochastic process $x(t)$, $-T/2 < t < T/2$, The sample spectrum $C_{xx}(f)$ defined for a continuous range of frequency $(-\infty, \infty)$ can be expressed as

$$C_{xx}(f) = T |X(f)|^2 \quad (3.1.1)$$

where $X(f)$ is the Fourier transform of $x(t)$

$$X(f) = \frac{1}{T} \int_{-T/2}^{T/2} x(t) e^{-i2\pi ft} dt \quad (3.1.2)$$

(3.1.1) then becomes

$$C_{xx}(f) = \frac{1}{T} \int_{-T/2}^{T/2} x(t) e^{-i2\pi ft} dt \int_{-T/2}^{T/2} x(t') e^{i2\pi ft'} dt'$$

By defining a pair of new variables $u=t-t'$ $v=t'$, (3.1.3) becomes

$$C_{xx}(f) = \int_{-T}^T c_{xx}(u) e^{-i2\pi fu} du \quad (3.1.4)$$

where $c_{xx}(u)$ is the sample auto-covariance function (ACF) and is computed as

$$C_{xx}(u) = \begin{cases} 0 & |u| > T \\ \frac{1}{T} \int_0^{T-|u|} (x(t) - \bar{x})(x(t+|u|) - \bar{x}) dt & 0 \leq |u| \leq T \end{cases} \quad (3.1.5)$$

Thus the sample spectrum is the Fourier transform of the sample ACF. By taking the inverse transform of (3.1.4), we get

$$C_{xx}(0) = \sigma_x^2 = \int_{-\infty}^{\infty} C_{xx}(f) df \quad (3.1.6)$$

The sample spectrum is able to tell how the variance (or power) is distributed over frequencies. It is desired to produce a spectrum that has smaller variance than the raw spectrum $C_{xx}(f)$, yet preserves the total power. This can be achieved through a smoothing procedure which is commonly done by introducing a lag window on the ACF. The smoothed spectrum is of the form

$$\bar{C}_{xx}(f) = \int_{-\infty}^{\infty} w(u) C_{xx}(u) e^{-i2\pi fu} du \equiv \int_{-\infty}^{\infty} \bar{C}_{xx}(u) e^{-i2\pi fu} du \quad (3.1.7)$$

here $w(u)$ is the lag window which satisfies some basic properties: (1) $w(0) = 1$, (2) an even function, and (3) $w(u) = 0$ for $|u| > T$.

Now take the inverse transform of (3.1.7) and let $u=0$

$$\bar{C}_{xx}(0) = \int_{-\infty}^{\infty} \bar{C}_{xx}(f) df = w(0) C_{xx}(0)$$

By use of property (1), we get

$$\bar{C}_{xx}(0) = \int_{-\infty}^{\infty} \bar{C}_{xx}(f) df = C_{xx}(0) = \int_{-\infty}^{\infty} C_{xx}(f) df \quad (3.1.8)$$

hence the total power (variance of the time series) remains invariant. In practice, we can replace property (3) by $w(u)=0$ for $|u| > M$ ($M < T$), and the ACF needs to be computed only up to maximum lag M .

The behavior of the spectrum is largely controlled by the selection of M . If we choose a small M the variance of the spectrum will be made small, thus the spectrum will look smoother. However, a smaller M means a larger base width (width of the main lobe of the corresponding spectral window, and is equal to $2/M$) which implies smoothing over a wide range of frequency, so that the bias (difference between the spectrum estimator and the true spectrum) may be large. The most commonly used lag windows are Bartlett, Tukey (cosine), and Parzen windows. The reader should refer to JW (1968) or Dtnes and Enochson (1972) for more details of the characteristics of these windows. In general, for a given M , the Parzen estimator has the smallest variance, and the Tukey estimator has the lowest bias. We choose Tukey window in this study because of the preference of its low-bias characteristic. The algebraic expression for the Tukey window is

$$w(u) = \begin{cases} 0.5 \left(1 + \cos \frac{\pi u}{M} \right) & |u| \leq M \\ 0 & |u| > M \end{cases} \quad (3.1.9)$$

and the corresponding spectral window is

$$W(f) = M \left(\frac{\sin(2\pi fM)}{2\pi fM} \right) \left(\frac{1}{1 - (2fM)^2} \right), \quad -\infty < f < \infty \quad (3.1.10)$$

The variance of the smoothed spectrum can be reduced to (75M/T)% of the unsmoothed spectrum. In this study, we choose M to be 25 days, therefore, the variance is reduced to about 10% of that of the raw spectrum.

Equation (3.1.7) can be written in discrete form for a batch of discrete type data

$$\bar{C}_{xx}(f) = 2\Delta t \left\{ C_{xx}(0) + 2 \sum_{k=1}^{L-1} C_{xx}(k) W(k) \cos(2\pi f k \Delta t) \right\} \quad (3.1.11)$$

where Δt is the time interval, L equals $M/\Delta t$. We calculate $C_{xx}(f)$ only over the positive half of the range of frequency, i.e. $0 < f < 1/2 \Delta t$ since $C_{xx}(f)$ is an even function. Then the value is doubled as is necessary to preserve the transform relation between sample spectrum and sample ACF.

In (3.1.11) $c_{xx}(k)$ is calculated as

$$C_{xx}(k) = \sum_{t=1}^{N-k} (x_t - \bar{x})(x_{t+k} - \bar{x}), \quad 0 \leq k \leq N-1 \quad (3.1.12)$$

where $N = T/\Delta t$, which is the total number of data points; and the lag window (Tukey) is

$$W(k) = \begin{cases} 0.5 \left(1 + \cos\left(\frac{\pi k}{L}\right) \right), & 0 \leq k \leq L \\ 0 & k > L \end{cases} \quad (3.1.13)$$

The 95% confidence interval is also estimated by calculating the lower and upper limits of the interval:

$$\frac{\nu \bar{C}_{xx}(f)}{\chi_{\nu}(1-\frac{1-0.95}{2})}, \frac{\nu \bar{C}_{xx}(f)}{\chi_{\nu}(\frac{1-0.95}{2})} \quad (3.1.14)$$

where ν is the degrees of freedom for the smoothed spectral estimator, and is equal to $2.667N/L$ for Tukey window. $\chi_{\nu}(\alpha)$ is the random variable distributed as chi-squared, with probability α . Taking the logarithm of (3.1.14), we get

$$\log \bar{C}_{xx}(f) + \log \frac{\nu}{\chi_{\nu}(1-\frac{1-0.95}{2})}, \log \bar{C}_{xx}(f) + \log \frac{\nu}{\chi_{\nu}(\frac{1-0.95}{2})}$$

The second parts in both expressions are independent of frequency, hence if we plot the spectrum on logarithmic scale, the confidence interval is constant for all frequencies and can be indicated by a single vertical bar.

3.1.2 Autospectra of the simulated wind stress

In fig. 3.1 the autospectra of the zonal and meridional wind stress components over the North Pacific Ocean at 42N are shown. The spectra have been averaged longitudinally over 5 points from 140E to 120W in order to increase the statistical stability. The minimum and maximum resolvable frequencies are $\frac{1}{2N\Delta t}$ and $\frac{1}{2\Delta t}$ (Nyquist frequency) which correspond to periods of 365 days and 12 hours respectively. The spectra are lower

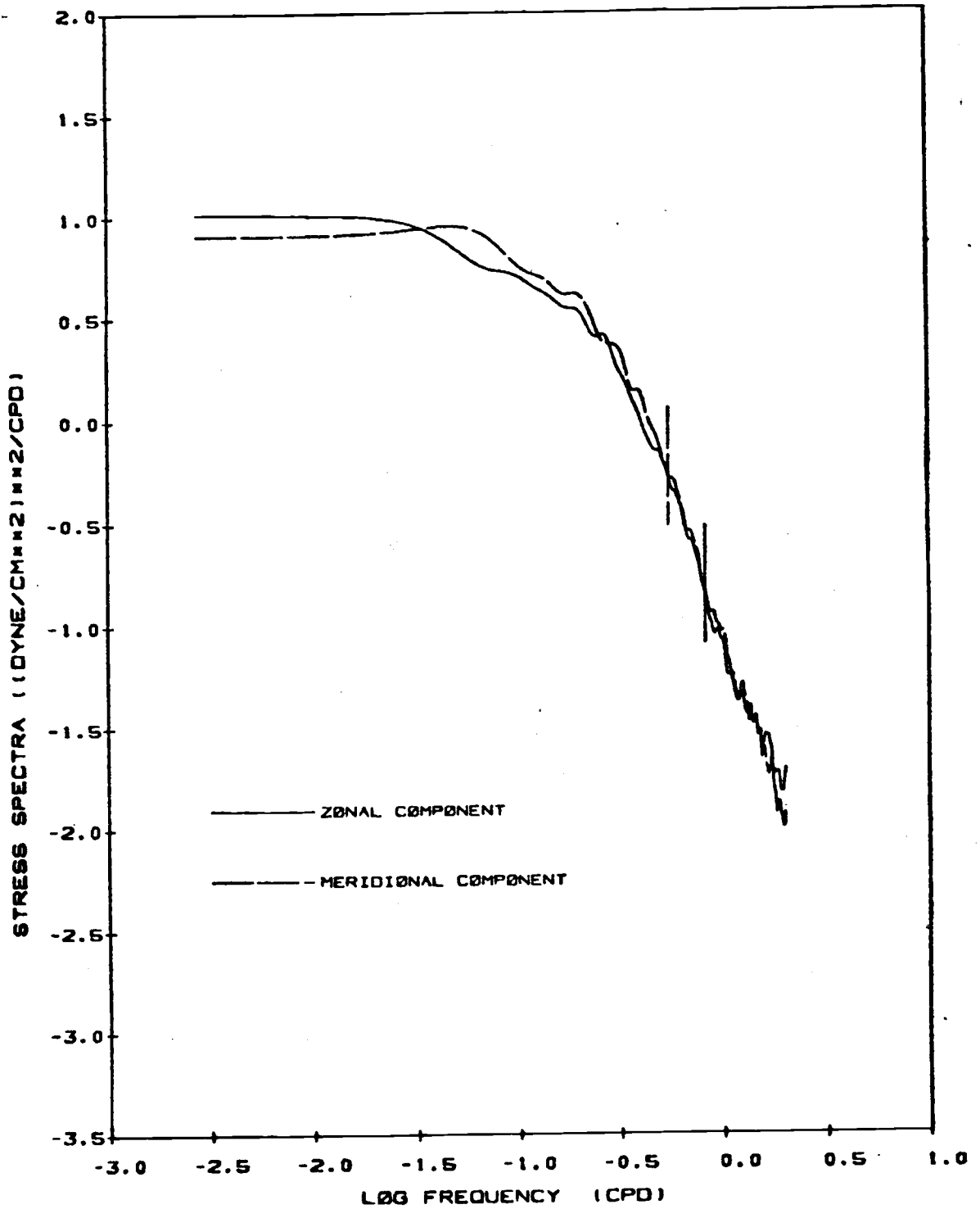


Fig. 3.1. Longitudinally averaged autospectra over the North Pacific Ocean at 42N (J=34). The 95% confidence interval is indicated by the vertical bars.

than $10 \text{ (dyne/cm}^2 \text{)}^2 \text{ /cpd}$ virtually everywhere with a sharp drop at 0.28 cpd which corresponds to synoptic scale of 3.6 days. The drop of power is almost linear with frequency on a log-log scale. No significant peak is found at any frequency. The spectrum of observed wind stress at 43N (Willebrand, 1978) shows a much flatter shape with a sharp drop at 0.3 cpd. The power is much larger than that of the simulated stress, especially at high frequencies. This is probably due to the inability of simulating fast moving meso-scale or small scale disturbances by a coarse-resolution model. Also, 43N happens to be the latitude of maximum observed rms stress in contrast to the minimum rms stress in simulated fields. The spectrum of the zonal component is larger than the meridional component only for frequencies lower than 0.035 cpd (28 days). This is true for most latitudes in the North Pacific. However, the stress spectra for the observed zonal component is larger for all frequencies.

Fig. 3.2 displays the wind stress magnitude spectra at five different latitudes from 26N to 62N. The shapes are similar except at 62N where the decrease at high frequencies is much more rapid. The structure of the rms stress field (fig. 2.13) is reflected here. Due to the multiple-center nature in the rms field, it is hard to judge which latitude has the maximum averaged energy, but

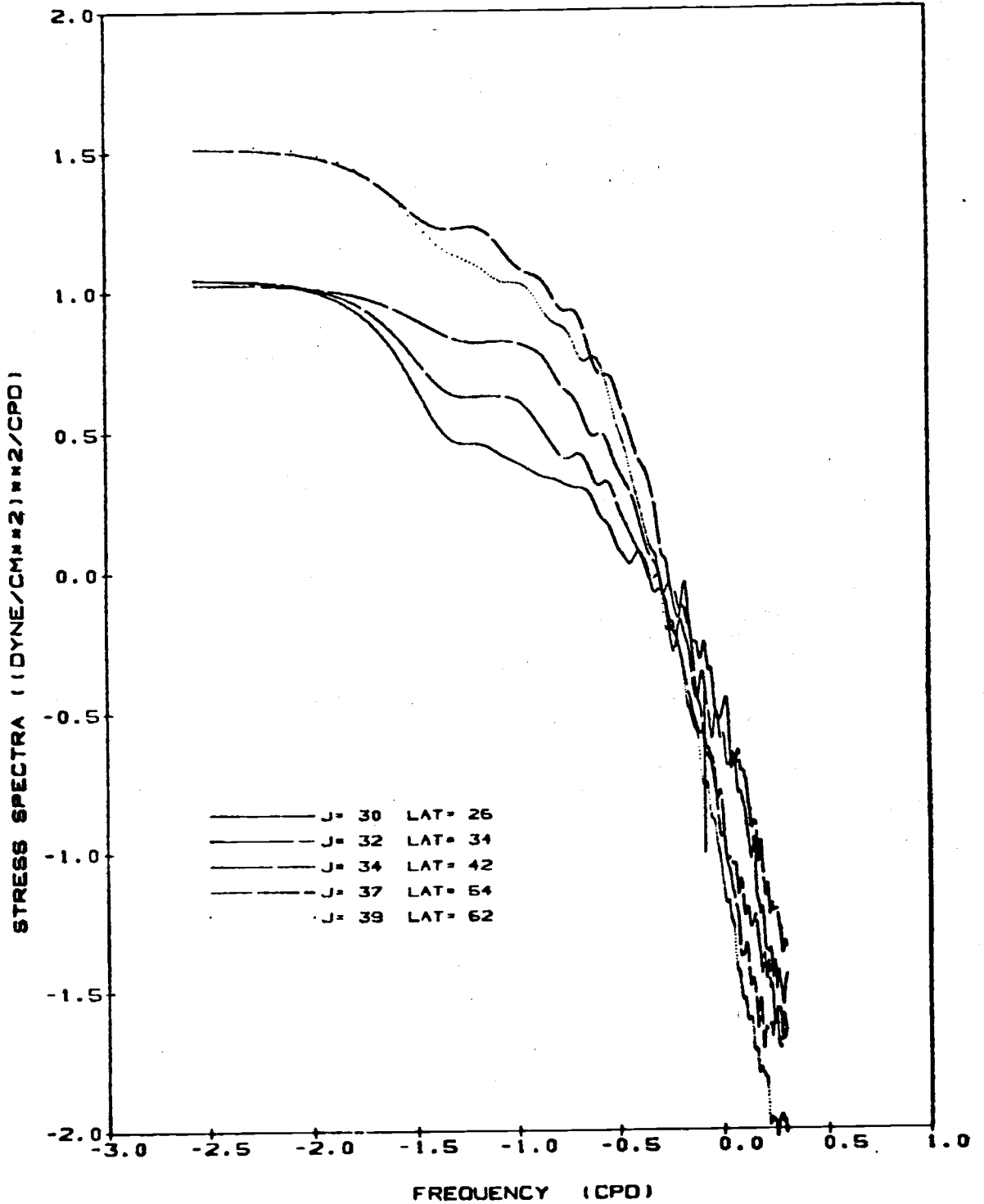


Fig. 3.2. Longitudinally averaged spectra of horizontal stress at 5 latitudes over the North Pacific Ocean.

it is clear that the northern latitudes have large energies than the southern latitudes. This indeed is the case in fig. 3.2, the spectra at 54N and 62N are larger than those at lower latitudes. The spectra drops at higher frequencies have virtually no difference for all latitudes.

The spectra of selected points over the North Atlantic Ocean reveals a very similar shape and energy level with those on about the same latitudes over the Pacific. However, the spectrum over the North Indian ocean exhibits a very different pattern. Fig. 3.3 illustrates the spectra of a point at (90E, 10N), just east of Sri Lanka. As expected from the rms stress field, the energy level is very low, especially for the meridional component. Both components show a significant peak at the diurnal frequency (one day). In the tropical atmosphere, a diurnal variability is evident due to several possible mechanisms depending on the geographical location. Over or near islands and lands, the diurnal variations of many atmospheric parameters are controlled by land-sea breeze (Houze et al., 1981). Over the open oceans, they are attributed to the day-night differences in the radiative heating profiles between the thick cloud covered area and the surrounding clear air areas (McBride and Gray, 1980). Atmospheric tide may also contribute to the diurnal variability although it is relatively weak. In the AGCM,

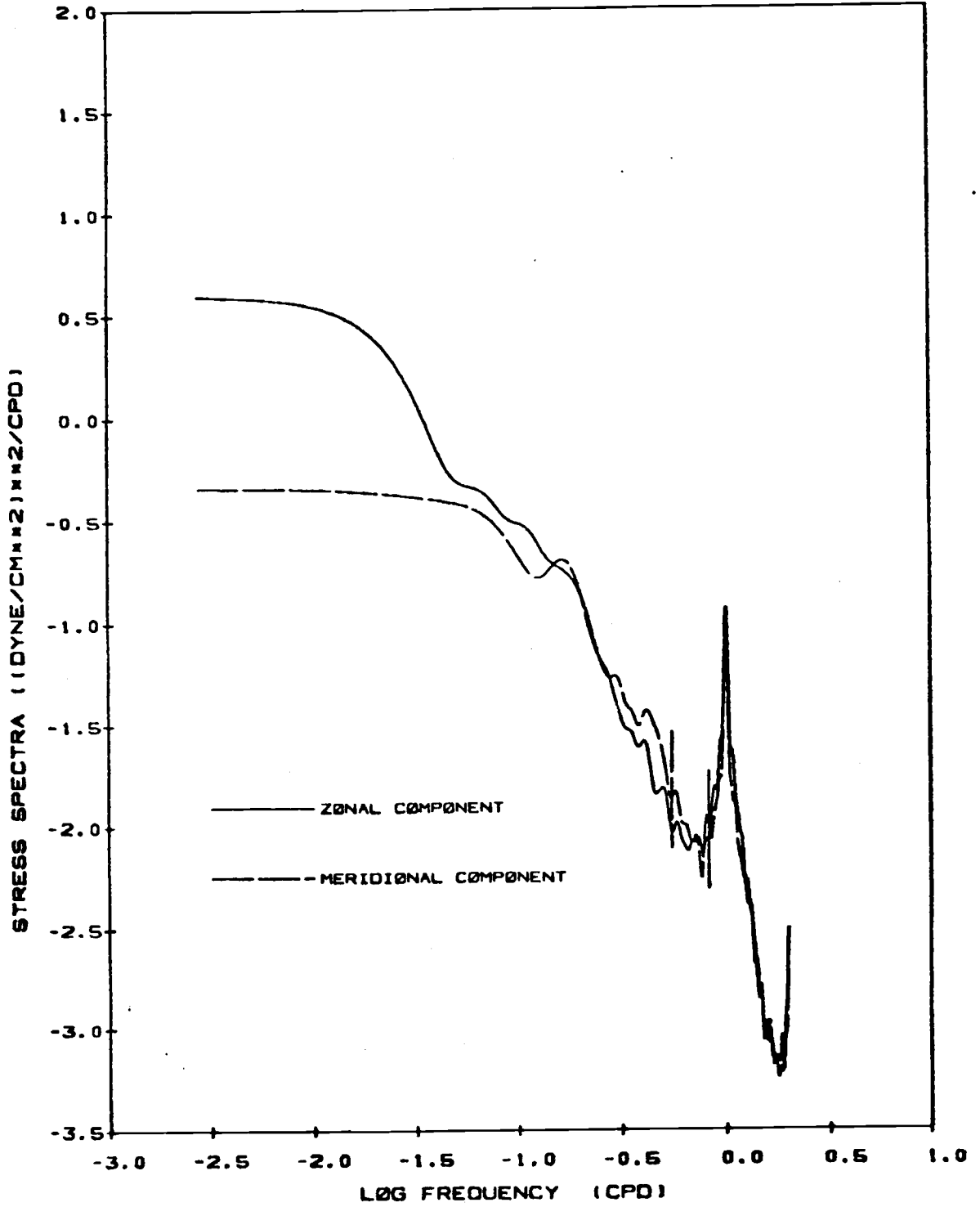


Fig. 3.3. Autospectra at (90E, 10N) (I=55, J=26).

the cloud effect and the diurnally varying characteristics of solar radiation are included. The most likely mechanism responsible for the peak at diurnal frequency over the ocean point is the existence of cloud. However, the effect of land-sea contrast cannot be ruled out because the selected point is surrounded by large land mass, besides, another point (175W, 6S) at the center of equatorial Pacific does not show such a strong peak at diurnal frequency. Fig. 3.4 shows the spectra of horizontal stress magnitude at four points in the South Pacific along 175W. The energy level increases with latitude except at 38S, just east of New Zealand.

Although the data period is only 3 years, it is still possible to resolve peaks of longer period (at least to the annual cycle) if there exists one. For this purpose, we have to use a much narrower window, i.e., larger M . To avoid large computing time, we first take the average of every four consecutive data to get a time series of one day interval. Then choose the maximum lag for Tukey window to be 365 days. By doing this, the degrees of freedom is largely reduced, hence a wider 95% confidence interval is expected. One point in the west Pacific Ocean on 42N is selected for this analysis. The spectra of the stress magnitude and both components are calculated. An average over frequency bands of different lengths is done for every

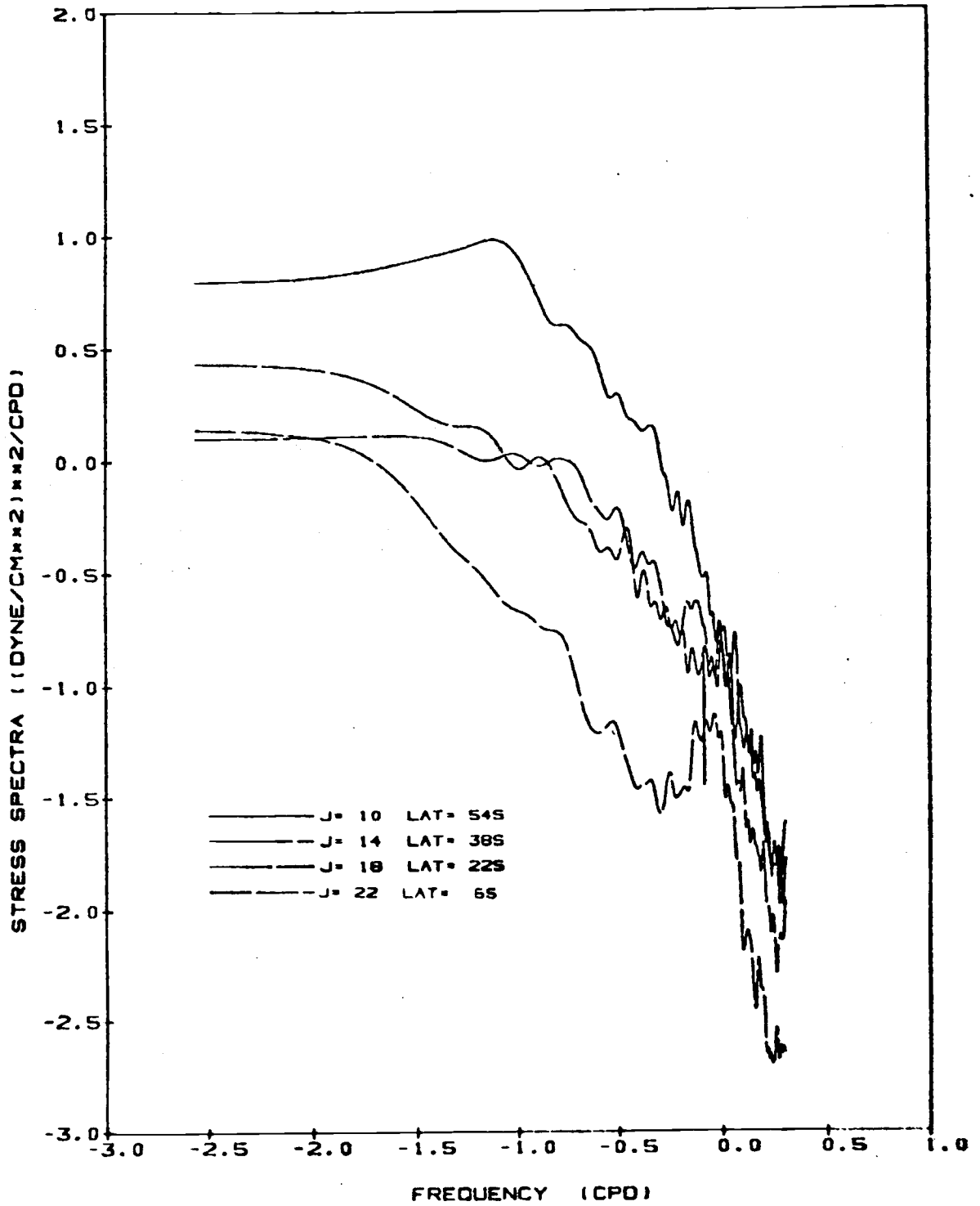


Fig. 3.4. Autospectra at 4 points over the South Pacific Ocean.

spectrum estimate in order to obtain equidistant spacing on a logarithmic scale and to eliminate the wiggles at higher frequencies. As shown in fig. 3.5, annual peaks are found in the stress magnitude and zonal component, though with great uncertainty. The meridional component does not exhibit a significant annual peak, however it has a peak at half-year cycle. The dynamics and the behavior of this fluctuation are not clear. The annual cycle is stronger in stress magnitude than in the components. This reveals the nonstationary character of the simulated wind field (Willebrand, 1978). Since the stress magnitude is a positive quantity, the annual cycle is distinct only when fluctuation of the component stress is much stronger in one season than in another six months later. To verify this, we repeat the procedure used in obtaining the spectra in fig. 3.1, except that the spectra are not averaged over all the 11 segments but over those containing the same six months period in the year. Four spectra are obtained roughly representing the four seasons. Again, the spectra are averaged over 5 points longitudinally. Those for winter and summer are shown in fig. 3.6. The energy level is higher in winter than in summer for all frequencies. The spectra for the other two seasons (not shown here) are somewhat in between. Willebrand pointed out that averaging over all seasons would distort the spectra shape in the presence of nonstationarity. However, if all the other

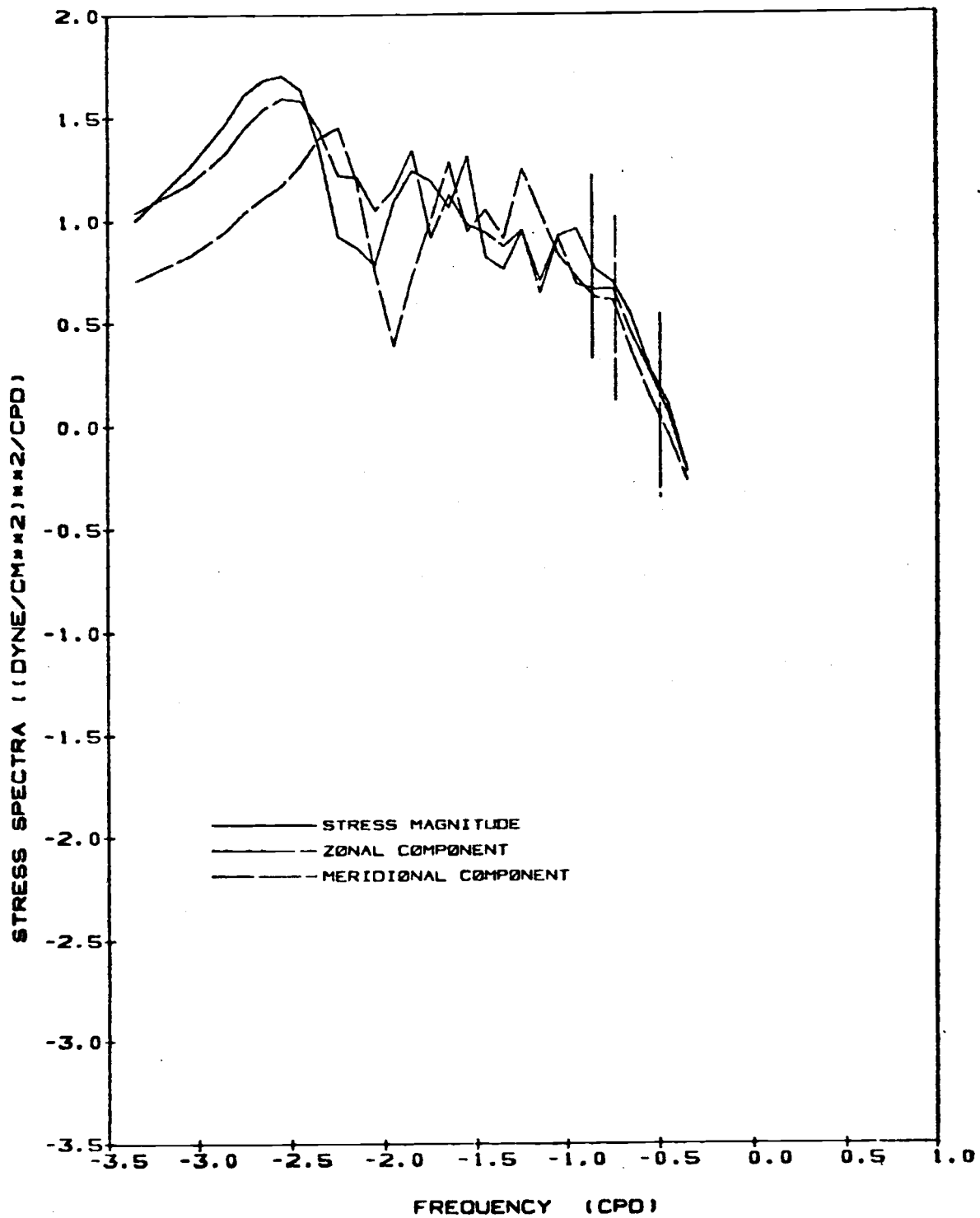


Fig. 3.5. Autospectra at (160E, 42N) (I=69, J=34).

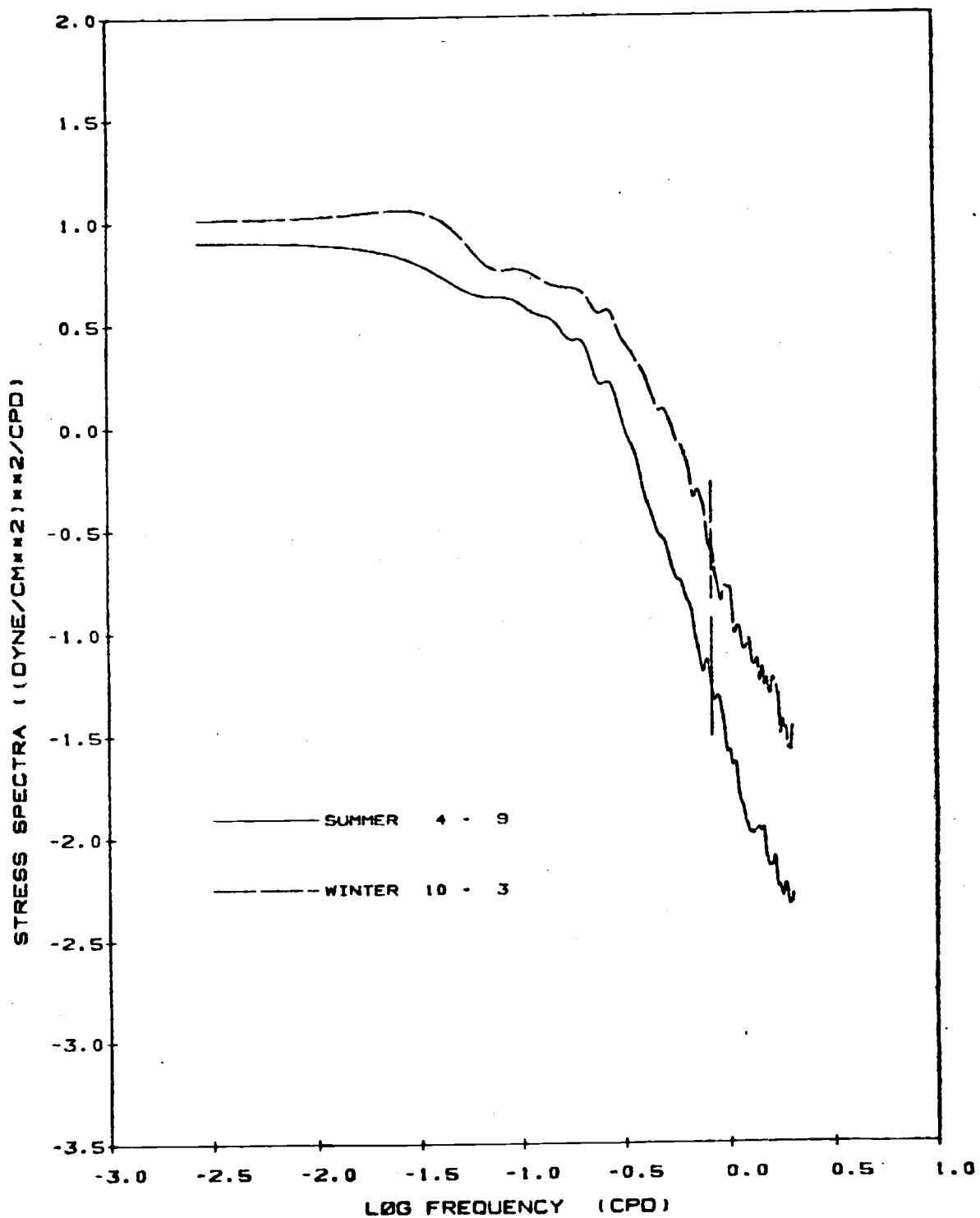


Fig. 3.6. Longitudinally averaged autospectra of zonal-component wind stress for the summer and winter over the North Pacific Ocean at 42N.

characteristics, such as the shape, remain unchanged for all seasons, as in the present analysis and in the real atmosphere, the averaging would be justified and will increase the statistical stability.

3.2. Cross-spectral analysis

3.2.1 Algorithm and Method of calculation

The sample cross spectrum is defined as

$$C_{x_1x_2}(f) \equiv C_{12}(f) = T X_1^*(f) X_2(f) \quad (3.2.1)$$

for two time series $x_1(t)$ and $x_2(t)$ in the range $-T/2 < t < T/2$, where the asterisk denotes the complex conjugate. By similar steps as in section 3.1., we get

$$C_{12}(f) = \int_{-T}^T c_{12}(u) e^{-i2\pi fu} du \quad (3.2.2)$$

where $c_{12}(u)$ is the sample cross covariance function (CCF) and is defined as

$$\begin{aligned} c_{12}(u) &= \frac{1}{T} \int_{-T/2}^{T/2-u} (x_1(t) - \bar{x}_1)(x_2(t+u) - \bar{x}_2) dt, \quad 0 \leq u \leq T \\ &= \frac{1}{T} \int_{-T/2+u}^{T/2} (x_1(t) - \bar{x}_1)(x_2(t+u) - \bar{x}_2) dt, \quad -T \leq u \leq 0 \\ &= 0, \quad |u| > T \end{aligned} \quad (3.2.3)$$

The inverse transform of (3.2.2) is written as

$$c_{12}(u) = \int_{-\infty}^{\infty} C_{12}(f) e^{i2\pi fu} df \quad (3.2.4)$$

Since $C_{12}(f)$ is a complex function, it can be written as

$$C_{12}(f) = R_{12}(f) - i G_{12}(f) \quad (3.2.5)$$

where $R_{12}(f)$ is an even function and $G_{12}(f)$ is an odd function. The sample amplitude and phase spectra are then defined as

$$A_{12}(f) = \sqrt{R_{12}^2(f) + G_{12}^2(f)} \quad (3.2.6)$$

$$F_{12}(f) = \tan^{-1}(-G_{12}(f)/R_{12}(f))$$

From (3.2.4) and (3.2.5), we get

$$C_{12}(u) = \int_{-\infty}^{\infty} R_{12}(f) \cos(2\pi fu) df + \int_{-\infty}^{\infty} G_{12}(f) \sin(2\pi fu) df \quad (3.2.7)$$

the first and second terms on the right hand side represent the even part $r_{12}(u)$ and odd part $g_{12}(u)$ of the CCF, respectively. They can be obtained by the definition of CCF:

$$r_{12}(u) = \frac{1}{2}(C_{12}(u) + C_{12}(-u)) = \int_{-\infty}^{\infty} R_{12}(f) \cos(2\pi fu) df \quad (3.2.8)$$

$$g_{12}(u) = \frac{1}{2}(C_{12}(u) - C_{12}(-u)) = \int_{-\infty}^{\infty} G_{12}(f) \sin(2\pi fu) df$$

By taking the inverse transform of the last two equations, we can calculate the value of $R_{12}(f)$ and $G_{12}(f)$ as

$$R_{12}(f) = \int_{-T}^T r_{12}(u) \cos(2\pi fu) du \quad (3.2.9)$$

$$G_{12}(f) = \int_{-T}^T g_{12}(u) \sin(2\pi fu) du$$

Thus the amplitude and phase spectrum can be obtained by

(3.2.6). To get a smoothed spectral estimates, we introduce the lag window $w(u)$ as a weighting function,

$$\begin{aligned}\bar{R}_{12}(f) &= \int_{-T}^T r_{12}(u)w(u)\cos(2\pi fu)du \\ \bar{G}_{12}(f) &= \int_{-T}^T g_{12}(u)w(u)\sin(2\pi fu)du\end{aligned}\quad (3.2.10)$$

The smoothed amplitude and phase spectra are then obtained by replacing R_{12} and G_{12} in (3.2.6) with \bar{R}_{12} and \bar{G}_{12} in (3.2.10). It is often more convenient to calculate the squared coherency spectrum defined as

$$\bar{K}_{12}^2(f) = \bar{A}_{12}^2(f) / (\bar{C}_{11}(f)\bar{C}_{22}(f)) \quad (3.2.11)$$

where $\bar{C}_{11}(f)$ and $\bar{C}_{22}(f)$ are the frequency spectra for time series $x_1(t)$ and $x_2(t)$ respectively as described in the previous section.

The discrete form of the above equations for estimating the smoothed cross spectra are similar to those for autospectra, hence they are not described here.

JW showed that an estimator $Y_{12}(f)$ which takes the inverse hyperbolic tangent value of coherency $|K_{12}|$ will have a variance which is controlled only by the smoothing factor (variance ratio) of the imposed window, and is relatively independent of frequency. Hence, the confidence interval can be represented by a constant interval on the Y

scale. The coherency spectra to be shown in this section will be in Y scale. The 95% confidence interval is calculated and illustrated by a vertical bar.

For squared coherency $K_{12}^2(f)$ at a certain frequency f , we have

$$Y_{12}(f) = \operatorname{arctanh} |K_{12}(f)| = \frac{1}{2} \ln \frac{1 + |K_{12}|}{1 - |K_{12}|} \quad (3.2.12)$$

and the $100(1-\alpha)\%$ confidence interval is

$$Y_{12}(f) \pm \gamma \left(1 - \frac{\alpha}{2}\right) \sqrt{\frac{I}{2T}} \quad (3.2.13)$$

where $\pm \gamma \left(1 - \frac{\alpha}{2}\right)$ is the range in which the $100(1-\alpha)\%$ chance that a random variable with normal distribution will fall, the value of γ is 1.96 for a probability of 95%. I/T is the variance ratio for a specified window, and is $0.75M/T$ for Tukey window. The confidence interval for phase spectral estimates depends on the coherency estimate and the degrees of freedom of the spectra estimate. We used a diagram provided in JW to determine the interval for a certain frequency. Several intervals are calculated and represented by vertical bars at corresponding frequencies.

The raw time series are divided into 5 overlapping segments of 12-month each. The cross spectra are calculated for each segment. An average over all segments is made for squared coherency and phase spectrum. Finally,

the confidence intervals are evaluated for Y estimator and phase spectrum.

3.2.2 Cross spectra of wind stress components

There are many options for selecting two time series to perform the cross spectral analysis. However, it is often hard to interpret the information that the cross spectrum provides for a certain pair of quantities. The cross spectra that are presented here are two-point, one-field type of correlations. The "one-field" is either the zonal or meridional component of wind stress.

(a) Two points of east-west separation

Two points, at longitudes 160E (I=69) and 170E (I=71), on latitude 30N are selected. They are separated by an east-west distance of 963 Km. The coherences and phase differences are shown in fig. 3.7. The coherences for zonal stress are very high for lower frequencies. There is a distinct peak at 0.28 cpd (3.6 days) which corresponds to the synoptic time scale. The overall coherence for meridional stress is low except between 0.16 cpd (6.3 days) and 0.33 cpd (3 days). The low coherence at high frequencies could be either due to noise of any kind or to the destructive interference among different wavenumber in

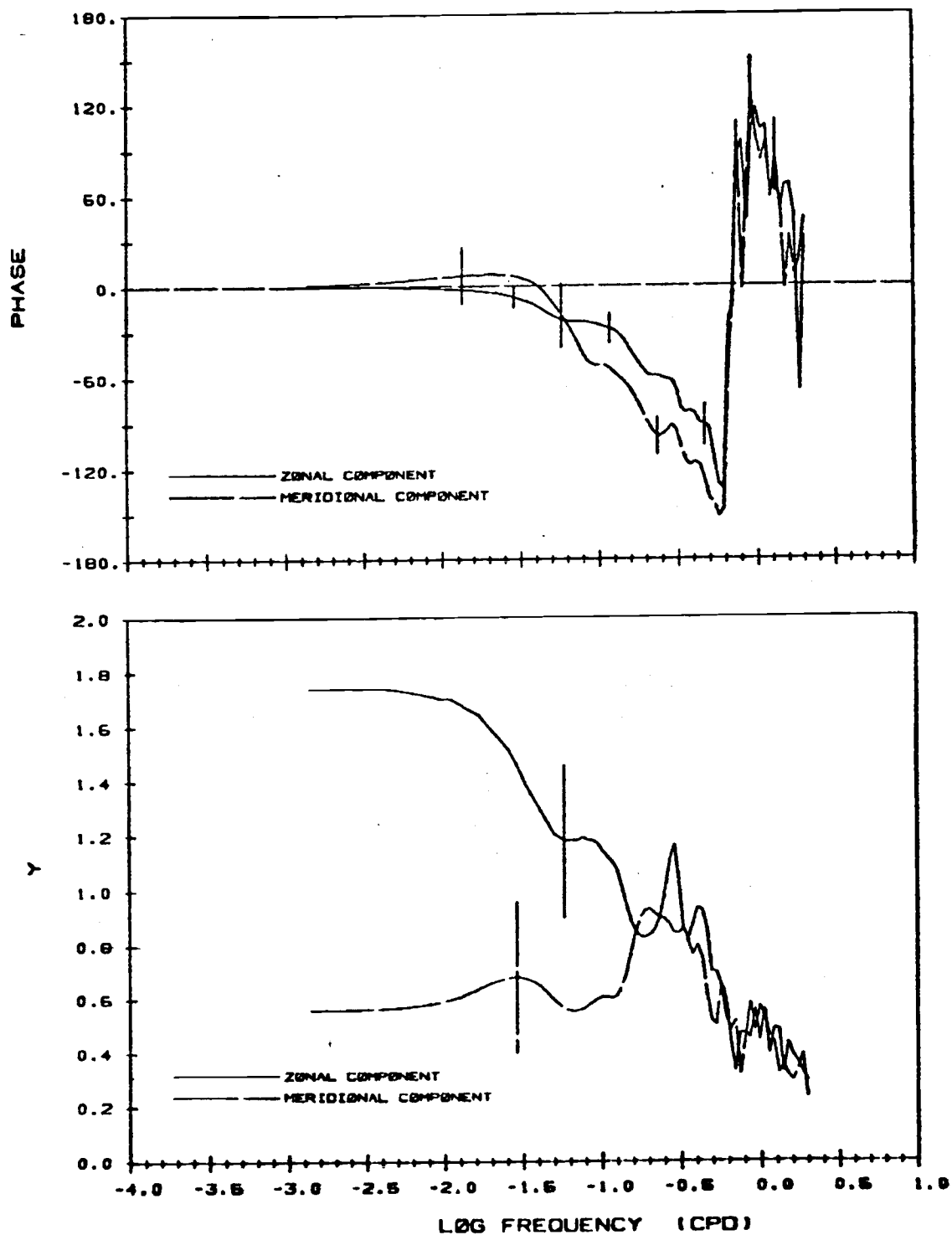


Fig. 3.7. Coherence and phase spectra of stress component for two points at (170E, 30N) and (160E, 30N) with a east-west separation of 963 Km. The Y is the inverse hyperbolic tangent of the coherence. See text for detail.

a process of broad wavenumber bandwidth. The latter was suggested by Willebrand in his analysis of the observational data.

If there is a net propagation of a disturbance from one spatial point to another, a phase difference will occur. Otherwise, the disturbance is symmetric with respect to the line that connects the two points. The phase spectrum of both stress components indicates the east-west asymmetry. The phases are nearly zero for periods longer than 15 days. It decreases to about -180 degrees at 0.63 cpd (1.5 days). The negative phase value means a lag of the first point (east point in this calculation) to the second point, hence indicating a net eastward propagation. The lag is more distinct for the meridional component indicating the association of smaller wavelength fluctuations. The sudden increase to positive value at higher frequencies is due to the use of a single branch of the multivalued arctan function in a computer and should be recognized as continuously decreasing.

Fig. 3.8 shows the results of the same process as above except the distance between the two points is doubled. The coherency estimates for both stress components are apparently lower than the previous estimates. However, it is interesting to note that

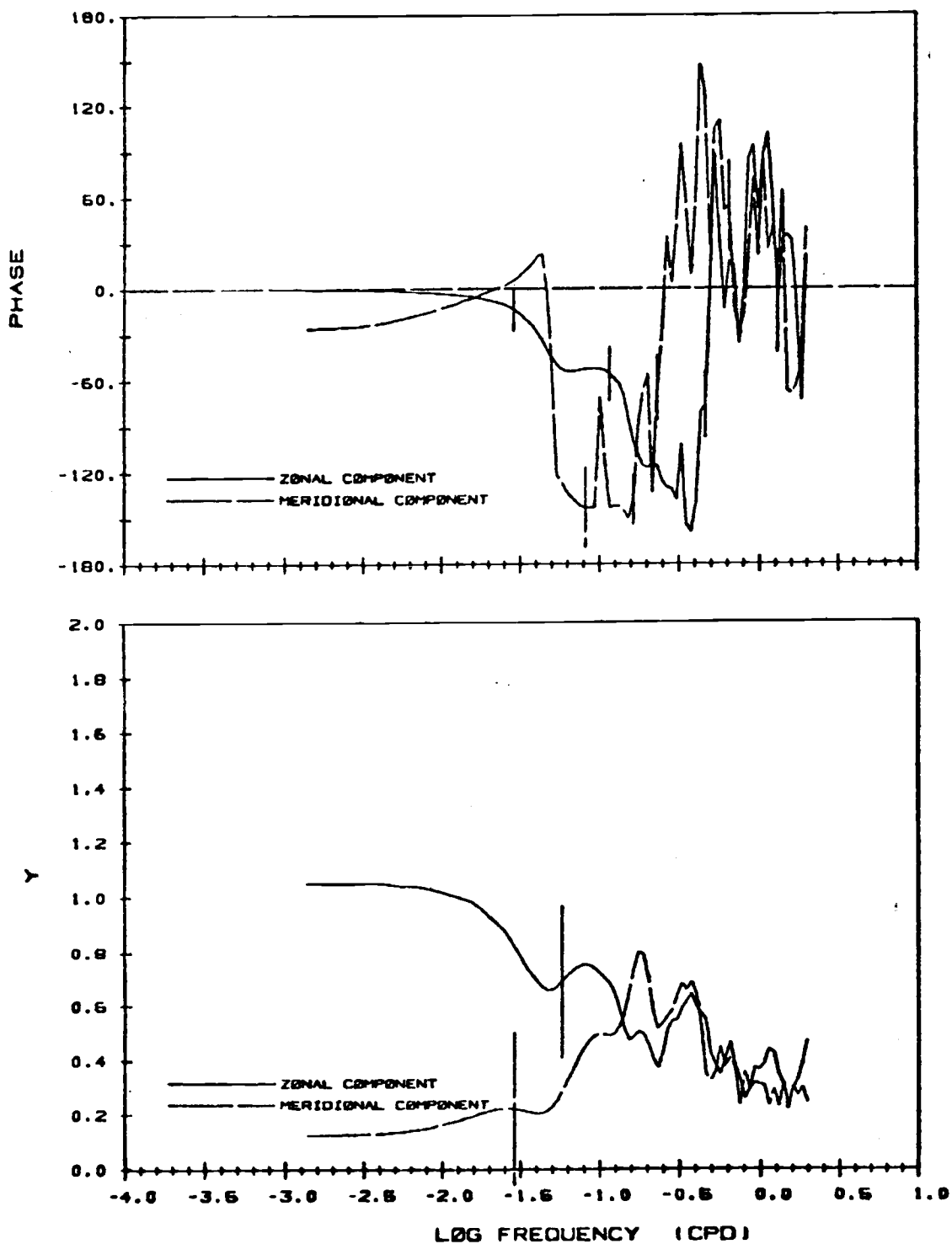


Fig. 3.8. As in Fig. 3.7 except for two points at (170E, 30N) and (150E, 30N) with an east-west separation of 1926 Km.

although the meridional stress is almost uncorrelated for most frequencies, the peak at 0.16 cod still clearly exists, but with lower coherence.

(b) Two points with south-north separation

The same analysis for two points along 160E separated by a south-north distance of 445 Km are shown in fig. 3.9. The stress components act differently when compared with the previous case. The meridional component now has the larger coherence for almost the entire frequency band. This phenomena, also found in the real atmosphere (Willebrand, 1978), can be predicted by the turbulence theory, which states that the longitudinal correlation exceeds the lateral correlation. The meridional components at the two points are well correlated at the synoptic period (4 days). The phase difference is essentially zero for all frequencies, indicating symmetric structure with respect to south-north wavenumber. The coherences of the zonal component are generally low for higher frequencies except at the synoptic scale of 3-5 days. The phase difference is slightly negative between periods of 6 days and 30 hours, indicating a southward propagation. We can see from figs. 3.7 and 3.9 that no matter what orientation the calculation is based on, the zonal component is always more 'red' than the meridional component.

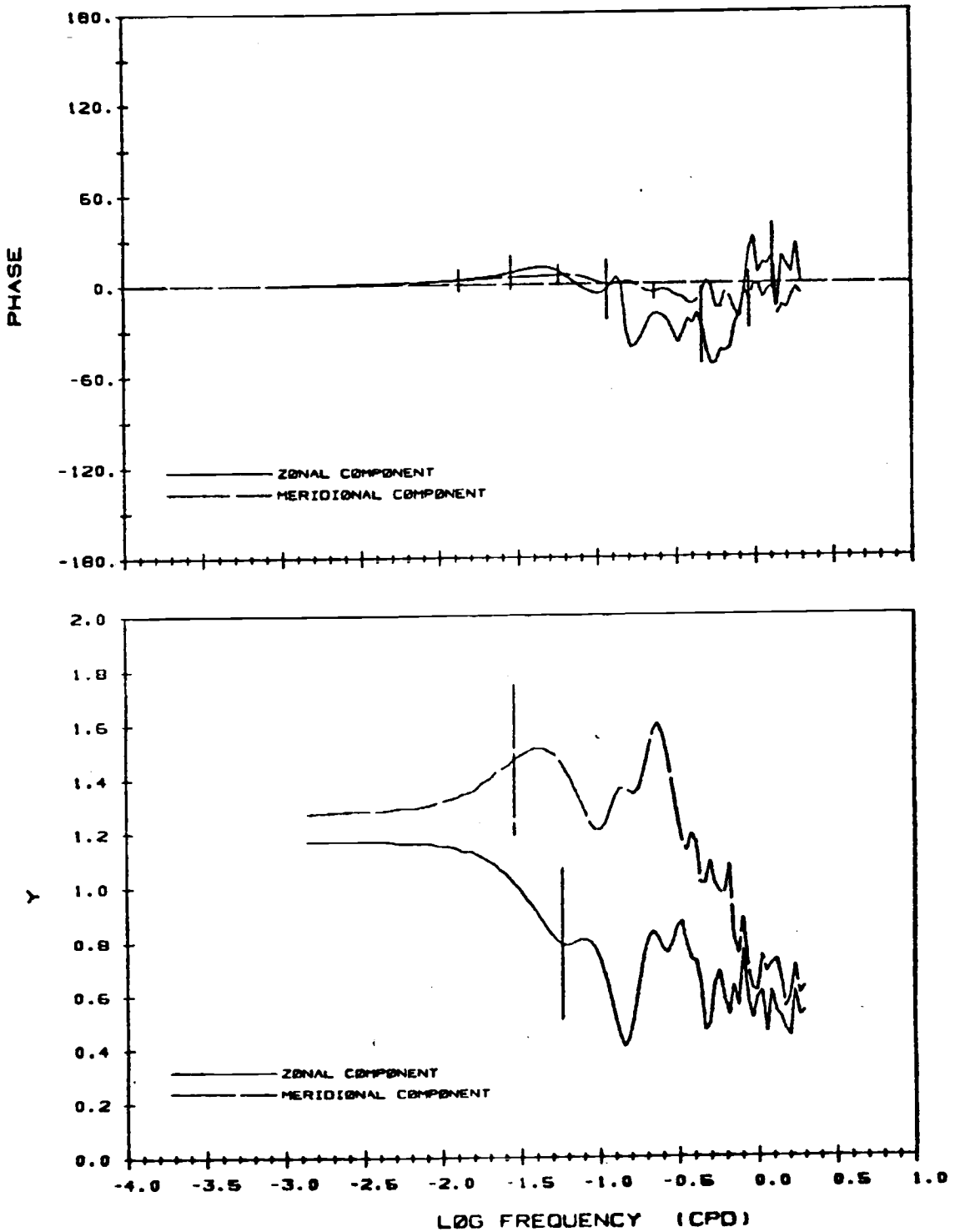


Fig. 3.9. As in Fig. 3.7 except for two points at (160E, 30N) and (160E, 34N) with a south-north separation of 445 Km.

Fig. 3.10 shows the results of the same process with doubled distance (890 Km). The coherences for both components decrease rapidly, especially at higher frequencies of the meridional component and at lower frequencies of the zonal component. Yet the peak at the synoptic period in the zonal component still exists. By comparing fig. 3.10 with fig. 3.7, we find that for about the same spacing between 2 points, the coherence is much larger for the zonal component, indicating the spatial scale for the disturbances is larger in its east-west direction than in its south-north direction.

In an attempt to resolve the signal of longer periods, we again modify the original time series as we did in the autospectral analysis, except the size is reduced to 1/8 of its original size by taking the average of 8 data in a two-day period. The maximum lag of the window is chosen to be 365 days (or $L=183$). Two points at 175W and 175E on 58N, separated by east-west distance of 589 Km, are selected. The spectrum of zonal stress is shown in fig. 3.11. The overall coherence is high. The most distinct peak at the low frequencies corresponds to the annual cycle. The phase is generally small, indicating a symmetric structure of low frequency disturbances.

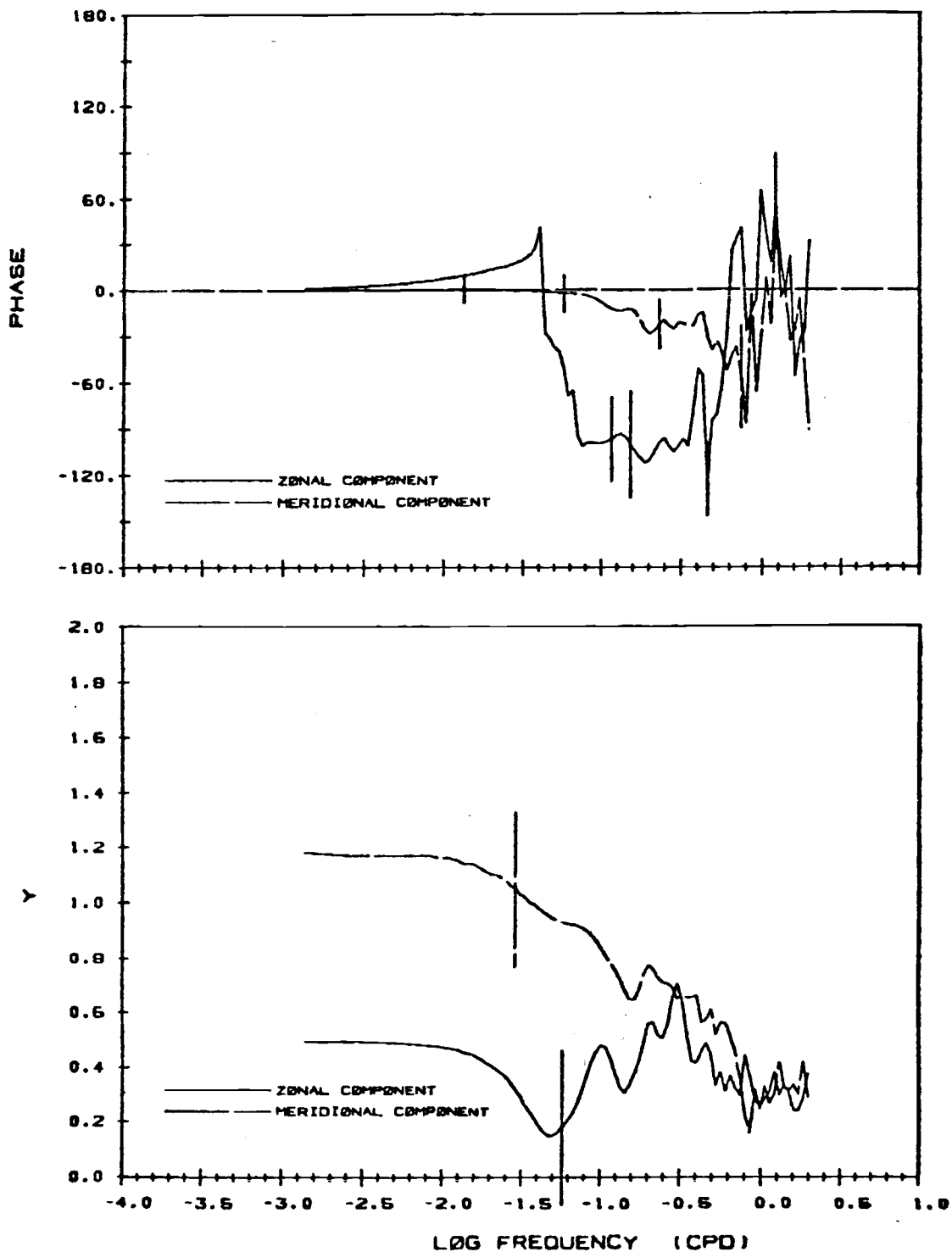


Fig. 3.10. As in Fig. 3.7 except for two points at (160E, 34N) and (160E, 42N) with a south-north separation of 890 Km.

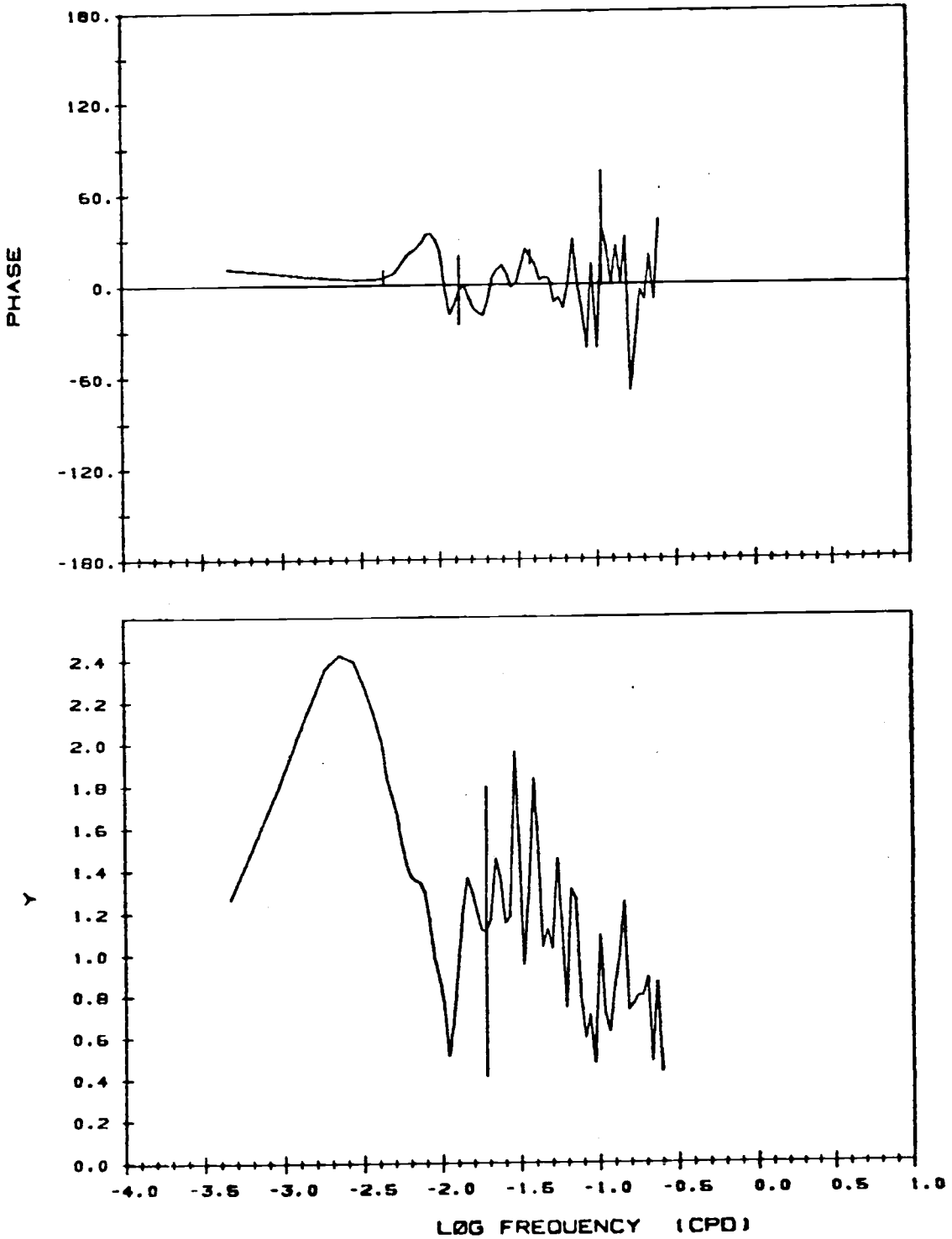


Fig. 3.11. Coherence and phase spectra of zonal component wind stress for two points at (175W, 58N) and (175E, 58N) with a east-west separation of 589 Km.

4. BAROTROPIC OCEAN EXPERIMENT

The large scale ocean circulation is primarily driven by atmospheric wind stress and the exchange of heat with the atmosphere. Certain processes in the earth's hydrologic cycle that affect the salinity, such as evaporation, precipitation and river runoff may also play an important role. In recent years, numerical modeling techniques have become increasingly useful for the study of these large scale ocean circulations. The basic principles of the numerical modeling for the ocean are not much different from those for the atmosphere. However, primary difficulties exist due to currently limited knowledge about oceanic processes, e.g. the subgrid-scale turbulent process. In spite of the difficulties, some experiments with coarse-grid global ocean models do show good reproduction of many of the observed ocean large-scale features, indicating that the coarse-resolution model is capable of simulating some large-scale processes.

The homogeneous wind-driven oceanic circulation model has been shown to be successful in describing the general characteristics of the horizontal circulation. In the real ocean, the most striking feature is the western intensification of the circulation. The pattern exists in each ocean although the basin differs in shape, topography,

stratification and pattern of wind stress. This might suggest that the ocean circulation is governed by a set of simple yet powerful constraints which are relatively independent of the factors which vary among ocean basins. The homogeneous model is able to expose those constraints in the most elementary way. Furthermore, when the model fails to predict some feature well, the physical cause can be roughly related to the absence of stratification or to any simplification made in the model. The homogeneous wind-driven model has been extensively used to study the roles of many factors in ocean general circulation, including the β -effect, nonlinear effects, bottom friction, bottom topography, etc. A good review of previous works on the homogeneous ocean circulation is given by Welander (1975), although only analytical models are included.

In this chapter, the barotropic version of the OSU six-layer OGCM is tested, in which the ocean is driven by the AGCM simulated surface wind stress. The OSU-OGCM is a primitive equation model in which the ocean is vertically divided up to six layers of unequal mass depending on the depth at each ocean point. The horizontal domain of the global model extends from 74N to 72S. The northern boundary follows the edges of the continental shelf of the composite landmass of the North and South America, Europe,

Africa and Asia. The southern boundary follows the edge of the continental shelf of Antarctica. New Zealand, Australia combined with New Guinea, and Antarctica are treated as islands. The horizontal grid size is 5 degrees in longitude and 4 degrees in latitude which matches the resolution of the OSU AGCM. A description of the governing equations, solution procedures, and the numerical methods is given by Han and Gates (1982a). The annual mean streamfunction of the mass transport and the seasonal variabilities of the streamfunction fields are discussed. They are also compared against those generated by the same model using observed wind stress.

4.1. The circulation driven by AGCM simulated wind stress

In this experiment, the density of sea water is fixed as a constant throughout the integration. The heat and salinity fluxes prescribed at the upper boundary are kept zero. The bottom topography is included, and was originally taken from Gates and Nelson (1975). The diffusivity in the vertical direction is given as $1 \text{ cm}^2/\text{sec}$, and that in the horizontal direction is $8 \times 10^9 \text{ cm}^2/\text{sec}$ for momentum and $2 \times 10^7 \text{ cm}^2/\text{sec}$ for heat and salt. The reference density is fixed as 1 gm/cm^3 and the specific heat of water is 1 cal/gm/deg C .

We will refer to the experiment with time-varying AGCM wind stress as Case A. In Case A the OGCM used a new set of AGCM simulated wind stress data every 6 hours. Starting from rest, the system was integrated for one simulated year. The annual mean of total mass transport streamfunction pattern is shown in fig. 4.1. Fig. 4.2 shows the streamfunction of simulated mass transport of the experiment in which the observed annual mean wind stress was used as the constant forcing (Han and Gates, 1982). We will refer to the latter experiment as Case B hereafter. The integration in Case B was carried out for 90 days to obtain a steady state.

The streamfunction fields shown in figs. 4.1 and 4.2 are quite similar in general. Both show many of the familiar ocean gyres. The nonlinear effect of the momentum advection term in the present model is relatively small compared to the lateral friction due to the use of large diffusivity. Hence, the mean circulation driven by the varying forcing field should be very close to that driven by constant mean forcing field.

In the Northern Hemisphere, clockwise gyres are clearly seen in both Case A and Case B, but the positions are different. The maximum transport is found to be on 20 N which is 10 degrees south to that of Case B. The

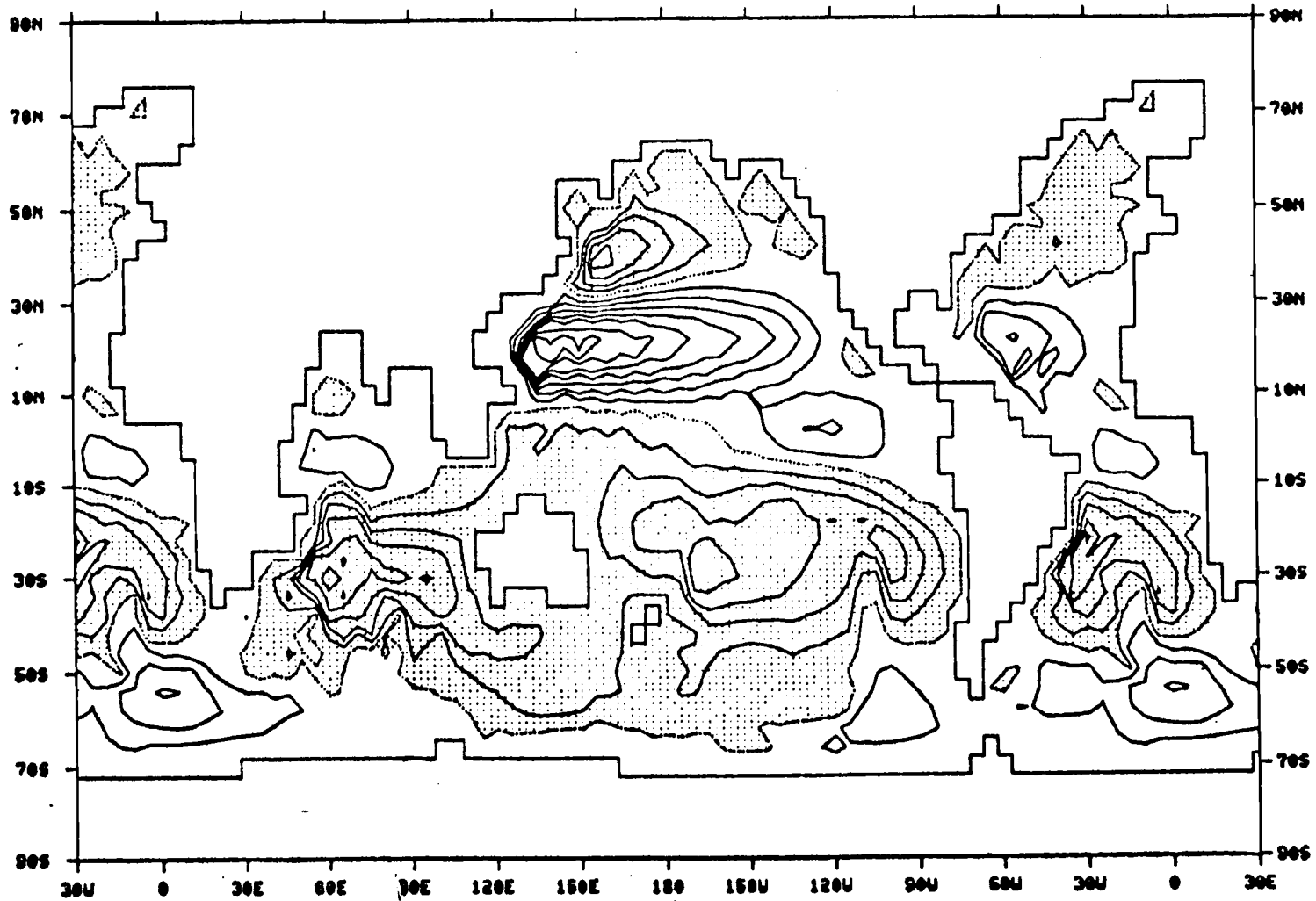


Fig. 4.1. Annual mean streamfunction of the mass transport of the oceanic circulation driven by the AGCM simulated surface wind stress. Contour interval is 4 Sv. The zero lines are dashed and the negative values are stippled.

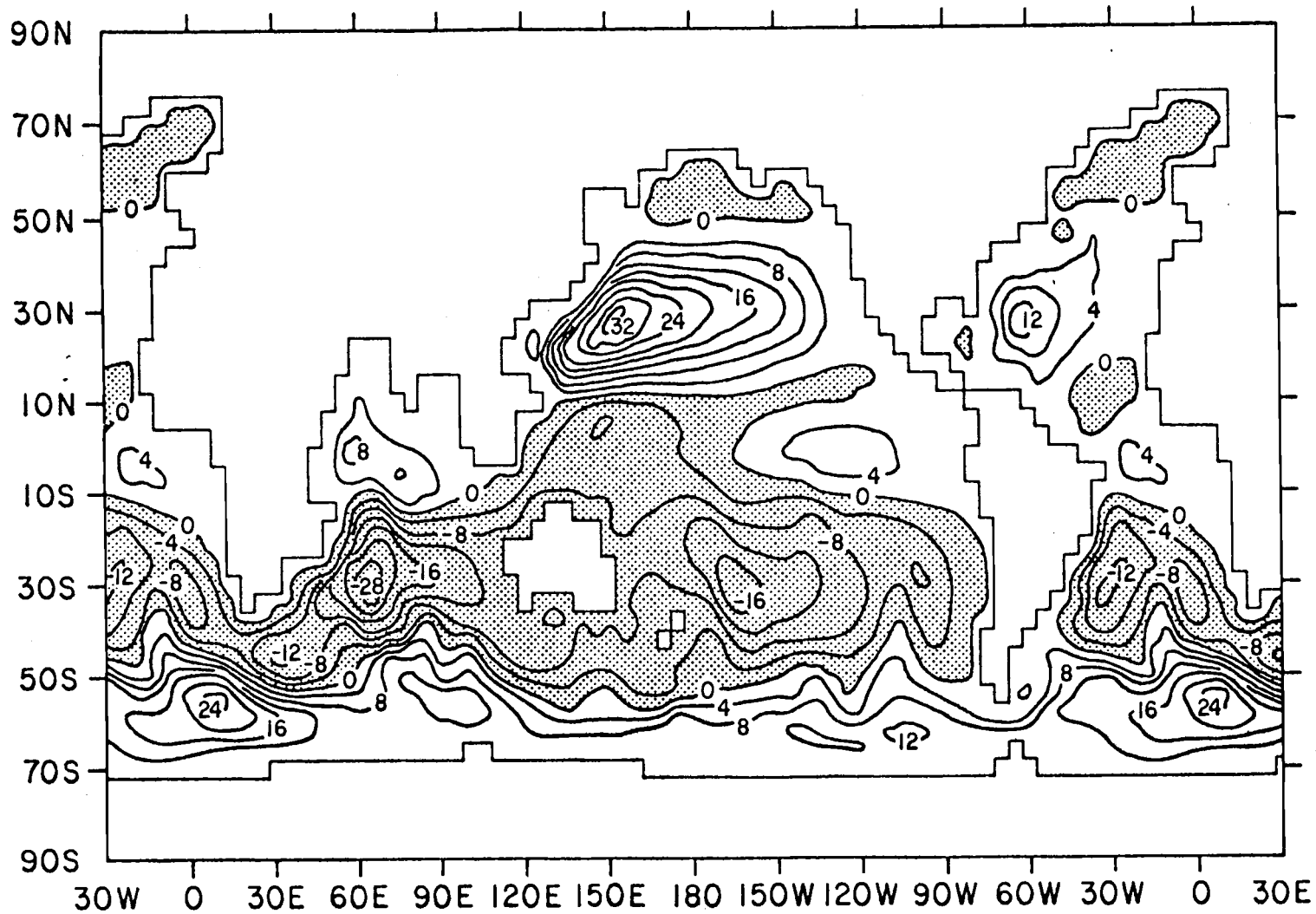


Fig. 4.2. Streamfunction of the mass transport at day 90 of the oceanic circulation driven by observed surface wind stress. Also see Fig. 4.1.

linear theory predicts that all the western boundary currents associated with the subtropical gyres intensify only to the latitudes of maximum wind stress curl, and subsequently return to the interior as broad and relatively slow currents. Hence, we could expect the 10 degree positioning error from the zonal mean curls as shown in fig. 2.11. The maximum transport of the clockwise circulation is about 30 Sv ($1 \text{ Sv} = 10^{12} \text{ cm}^3 / \text{sec}$) in the Pacific ocean. This is smaller than in Case B, but still in reasonable agreement with the observed geostrophic transport of 40 Sv. The transport in the Atlantic Ocean (Gulf stream) is 12 Sv, which is smaller than the 15 Sv in Case B. Both Cases, however, greatly underestimate the observed geostrophic transport of the Gulf stream. The discrepancy could be due to the lack of internal thermohaline circulation and/or a nonlinear recirculation which cannot be simulated by a coarse-grid viscous model (Han and Gates, 1982). By including the thermohaline forcing (Han and Gates, 1982b), the transport is enhanced to 27 Sv, which is comparable with the transport of the Florida Current (29 Sv), but still lower than the observed transport of 75 Sv in the vicinity of Cape Hatteras. In the Pacific Ocean, the north-south extent of the clockwise circulation is 30 degrees compared to 40 degrees in Case B. This is the result of the existence of a broad and strong counterclockwise subarctic gyre to the north. The transport

could reach 18 Sv while the transport of the same circulation in Case B is less than 4 Sv. The subarctic gyre in the North Atlantic Ocean is broad and rather weak.

In the Southern Hemisphere, the observed circulation pattern is in remarkable agreement with that of Case B. Differences are found only in the magnitude of transport. The Antarctica Circumpolar Current is much weaker in the present case. The total mass transport through the Drake Passage is less than 4 Sv compared to 10 Sv in Case B. The difference results directly from the smaller curl value of the AGCM simulated wind stress (fig. 2.12). It is hard to judge the accuracy of the present estimate due to the lack of direct measurement of this transport. However, the magnitudes in both cases are much smaller than other numerical studies. Han and Gates (1982b) found the transport is mainly affected by the joint effect of baroclinicity and topography. In the barotropic experiment which excludes the baroclinic effect, the transport is largely controlled by the value of eddy diffusivity because the wind stress torque is mainly balanced by the lateral friction in the Antarctica region. The present model uses a relatively large diffusivity and therefore greatly suppresses the transport.

The clockwise subtropical gyres in the South Atlantic

and South Pacific Oceans agree well with those in Case B. Both cases fail to simulate the East Australia current, which is the poleward return boundary flow of the South Pacific subtropical circulation. Instead, the model current passes Australia and flows into Indian Ocean through a narrow channel between Indo-China and Australia. The total mass transport through the channel is about 6 Sv in Case A compared to 10 Sv in Case B. The latter agrees with the observational estimate made by Godfrey and Golding (1981).

In the South Indian Ocean for Case A, the maximum transport of the counterclockwise circulation is about 20 Sv, which is less than 28 Sv of the corresponding circulation in Case B. The associated Agulhas current is not correctly simulated. It returns to the interior without branching around the southern tip of Africa as is found in Case B and the observation.

The tropical circulation is largely inertially controlled, therefore, it is poorly simulated due to the lack of inertial effect in the model. The only discernable tropical circulation is found in the eastern part of the Pacific. The maximum transport is 8 Sv in Case A and is about 6 Sv in Case B. Both are much less than the observational estimate of 40 Sv.

4.2. Seasonal Variation of the Simulated Ocean Transport

As can be seen in the last chapter, the imposed atmospheric forcing on the ocean can be of any cycle period between hours and years. However, most of the variance of the forcing field (wind stress) is explained in the range of one day to 300 days. Willebrand (1980) found the ocean response to the atmospheric disturbances with periods longer than one year, or close to the inertial period (18 hours), can be strongly trapped near the ocean surface. When the forcing period is away from the inertial period and is less than one year, the trapped response can penetrate to the ocean floor and is independent of depth. Hence, the simulated ocean response by the present barotropic model would be quite significant due to the temporal characteristics of the AGCM simulated wind stress field.

Figs. 4.3a-d display the monthly mean stream functions of January, April, July and October representing four seasons. In the Northern Hemisphere, the cyclonic gyre in the Pacific shifts about 5 degrees to the south of its winter position in the summer. This results from the south shift in the curl field. The mean mass transport by the associated Kuroshio current is larger in April than in other months. However, a more careful check of selected

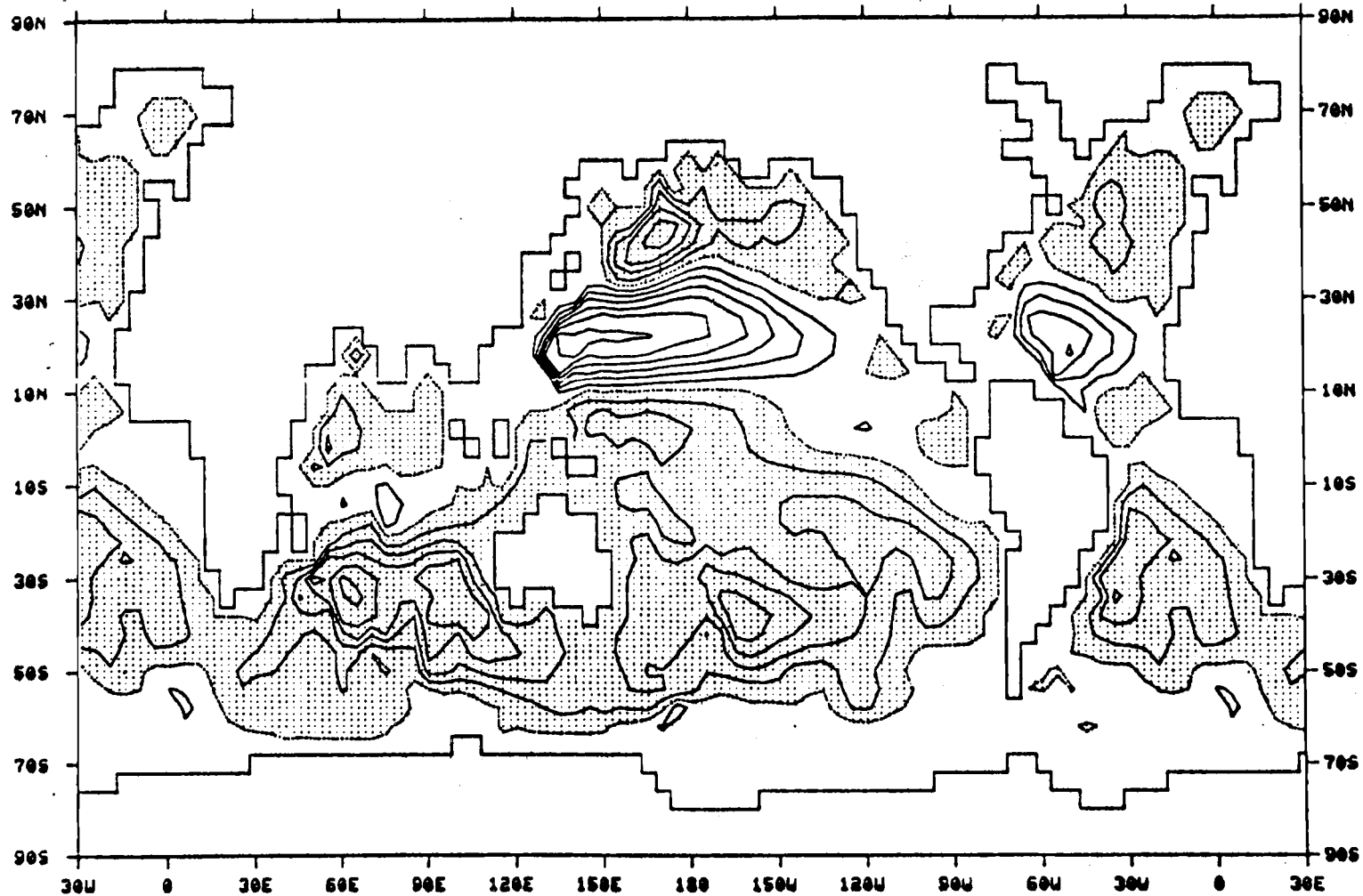


Fig. 4.3a. Monthly mean streamfunction of the simulated transport for January. Contour interval is 5 Sv. The zero lines are dashed and the negative values are stippled.

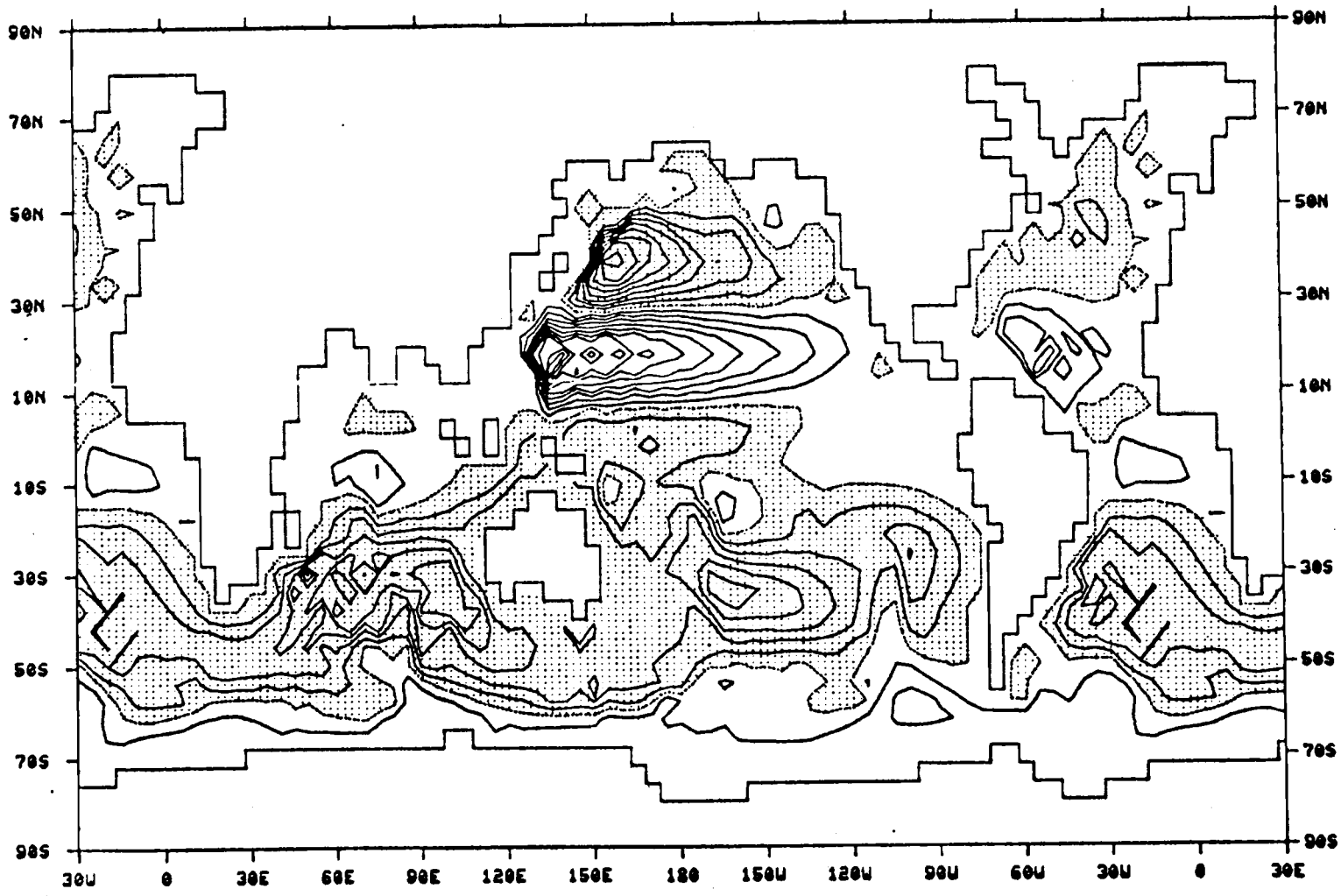


Fig. 4.3b. As in Fig. 4.3a except for April.

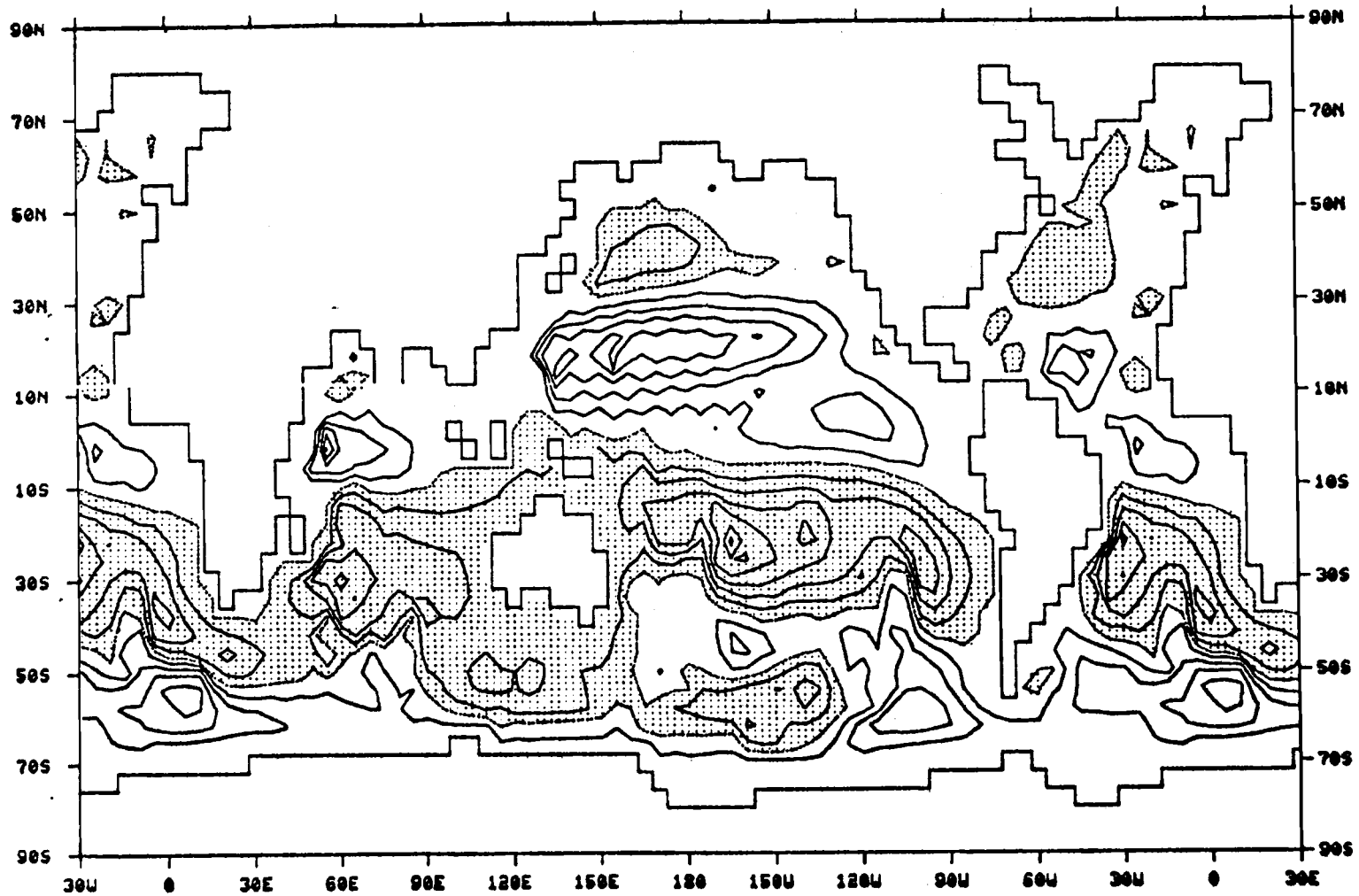


Fig. 4.3c. As in Fig. 4.3a except for July.

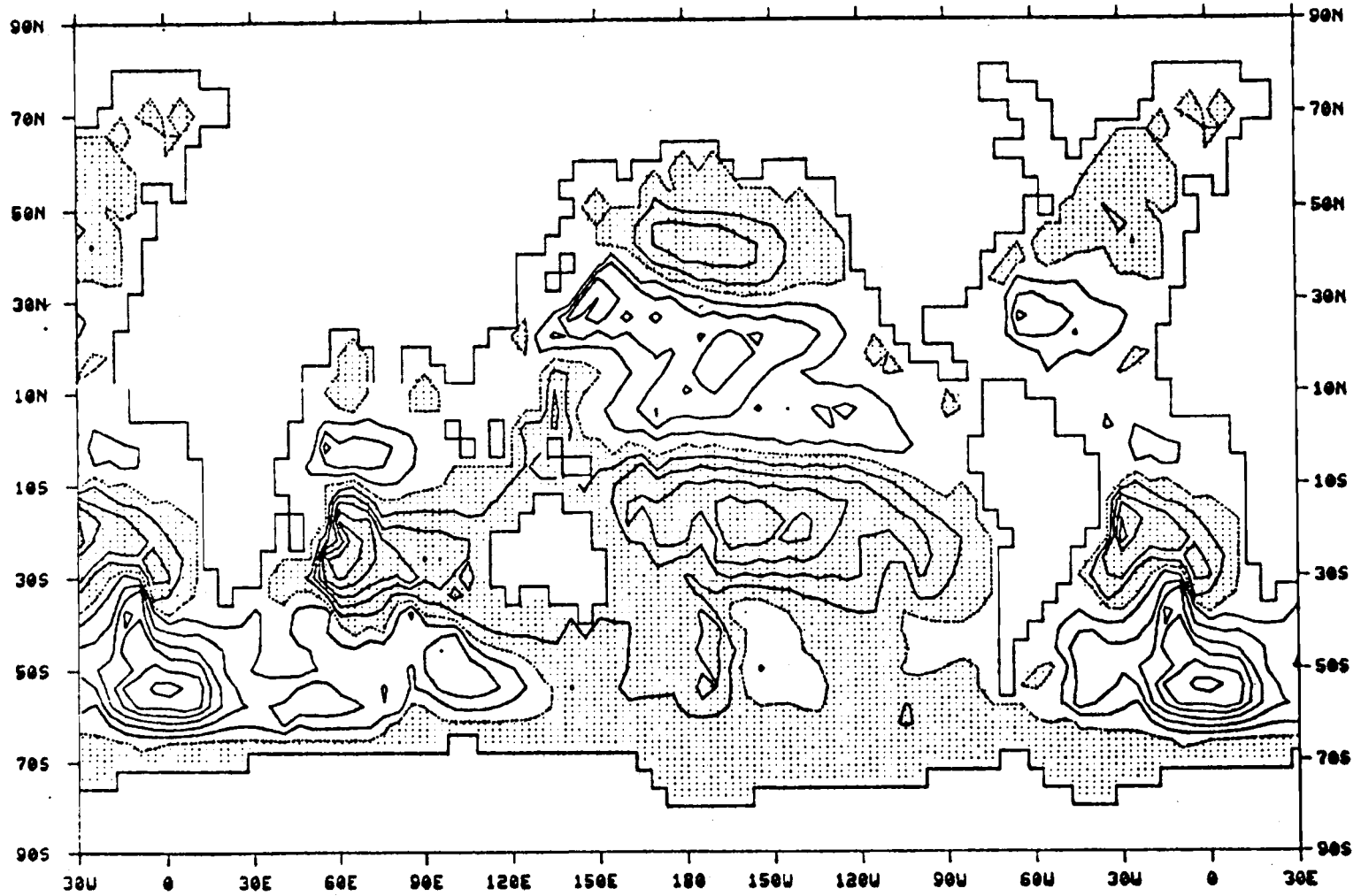


Fig. 4.3d. As in Fig. 4.3a except for October.

daily fields reveals a maximal transport of 60 Sv in late February and a minimum of 20 Sv in October. The annual variability is 40 Sv in Case A compared to 24 Sv in Case B in which maximum and minimum transport occur in January and September, respectively.

The Atlantic subtropical gyre also moves southward from winter to summer. The northward mass transport by the Gulf Stream Current reaches a maximum of 30 Sv in late January and is relatively low in early July. A minimum value of 8 Sv is found in late September but not in July. The annual variability agrees well in phase with that of Case B, but not in magnitude.

The most interesting seasonal variation is found in the North Indian Ocean. Although the strength of the summer monsoon is not adequately simulated by the AGCM, the ocean's response to the weak annual variation is pronounced. The clockwise circulation pattern in the winter gradually reverses its direction to become counterclockwise in the summer. The associated Somali current also reverses its direction with season as observed. The maximum southward transport occurs in January with a value of 8 Sv (1.7 Sv in Case B) and the maximum northward transport is about 24 Sv in July, which agrees well with that in Case B.

The subarctic circulation does not change much in the Atlantic Ocean while it varies significantly with time in the Pacific Ocean. The maximum mass transport occurs in January with an averaged magnitude of about 20 Sv. The minimum is found in summer months with a mean value of less than 8 Sv.

In the Southern Hemisphere, the subtropical counterclockwise circulation moves toward the equator as the seasons change from July (southern winter) to January. The annual variation of the simulated transport of the Brazil current is 12 Sv, which is larger than the 4 Sv simulated in Case B. The maximum of 24 Sv occurs in August and the minimum is in January.

In the Pacific Ocean, the transport of the return flow just east of New Zealand does not change much in the monthly mean fields, however, very rapid fluctuation can be seen from the selected daily fields, indicating the rapid response of the model to the forcing field. A weak clockwise gyre occupying the western equatorial Pacific in January intensifies and shifts westward as the season progresses to July. This is also observed in Case B. The simulated transport of the the Indian Ocean gyre shows little variation in magnitude. The Antarctica circumpolar current is fairly weak in January. It gradually

intensifies until July, and then weakens very rapidly.

Figs. 4.4a,b show the time-longitude sections of the streamfunction along 34N (J=32) for two 60-day periods of the simulation. The tilt of the isolines indicates westward phase propagation virtually everywhere, with the phase speeds of the order 9-10 m/sec. The amplitude increases from late October to late February as discussed in this section. This increase is almost synchronous with the seasonal increase in amplitude of the wind stress fluctuation (fig. 2.17). Groups of wave trains moving eastward can also be identified with a group speed of the order 70-80 cm/sec. Willebrand (1980), who did a barotropic experiment with varying wind stress forcing, found similar characteristics in the simulated zonal velocity field but with a smaller phase speed (3-5 m/sec). Therefore, the waves with westward phase propagation and eastward group velocity are likely to constitute a main part of the response of a barotropic model to the fluctuating winds.

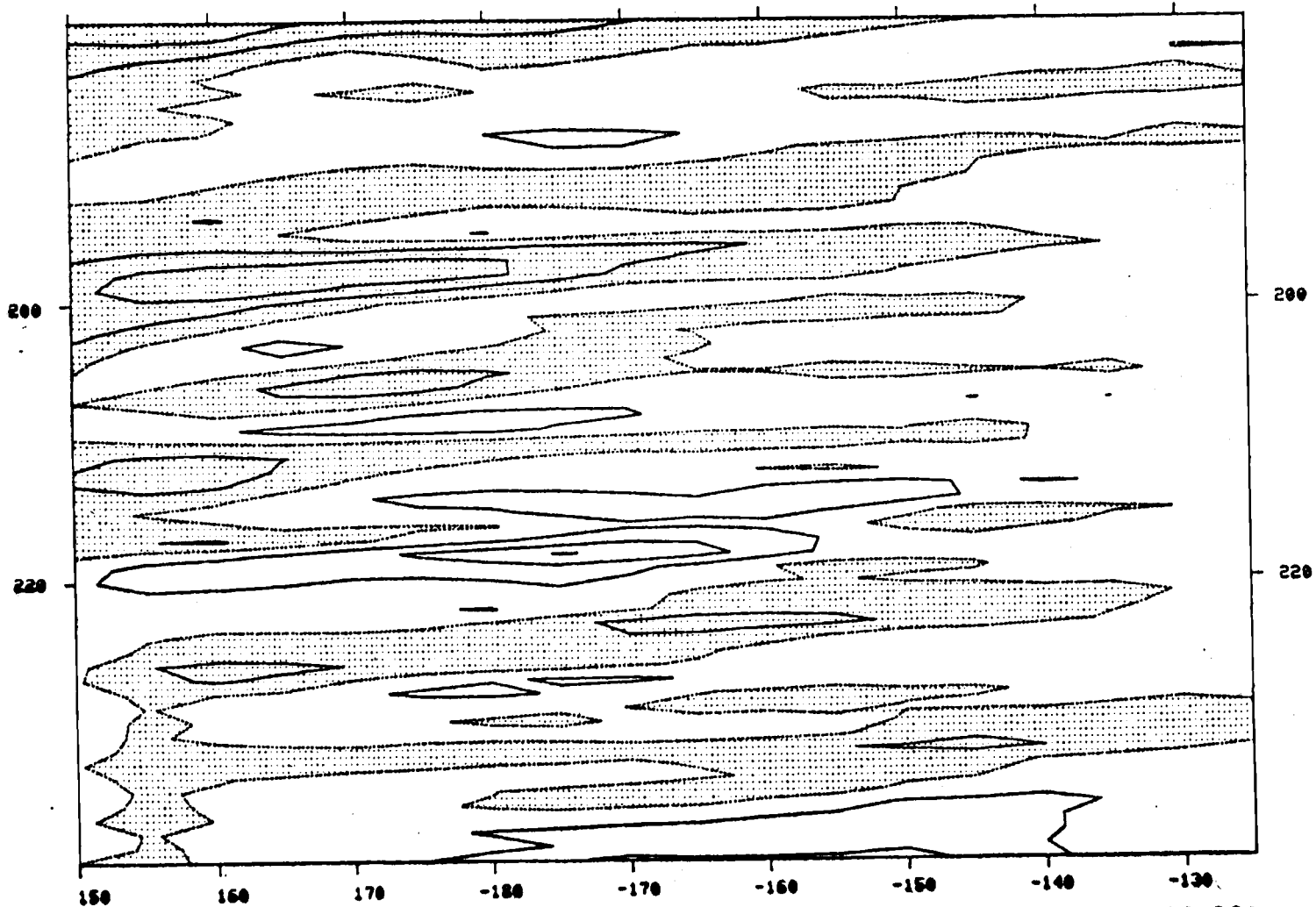


Fig. 4.4a. Time-longitude plot of the streamfunction along 34N (J=32) for day 180-240 of the simulation. Contour interval is 10 Sv. The zero lines are dashed and the negative values are stippled. The abscissa is the longitude (degree) and the ordinate is the time (day).

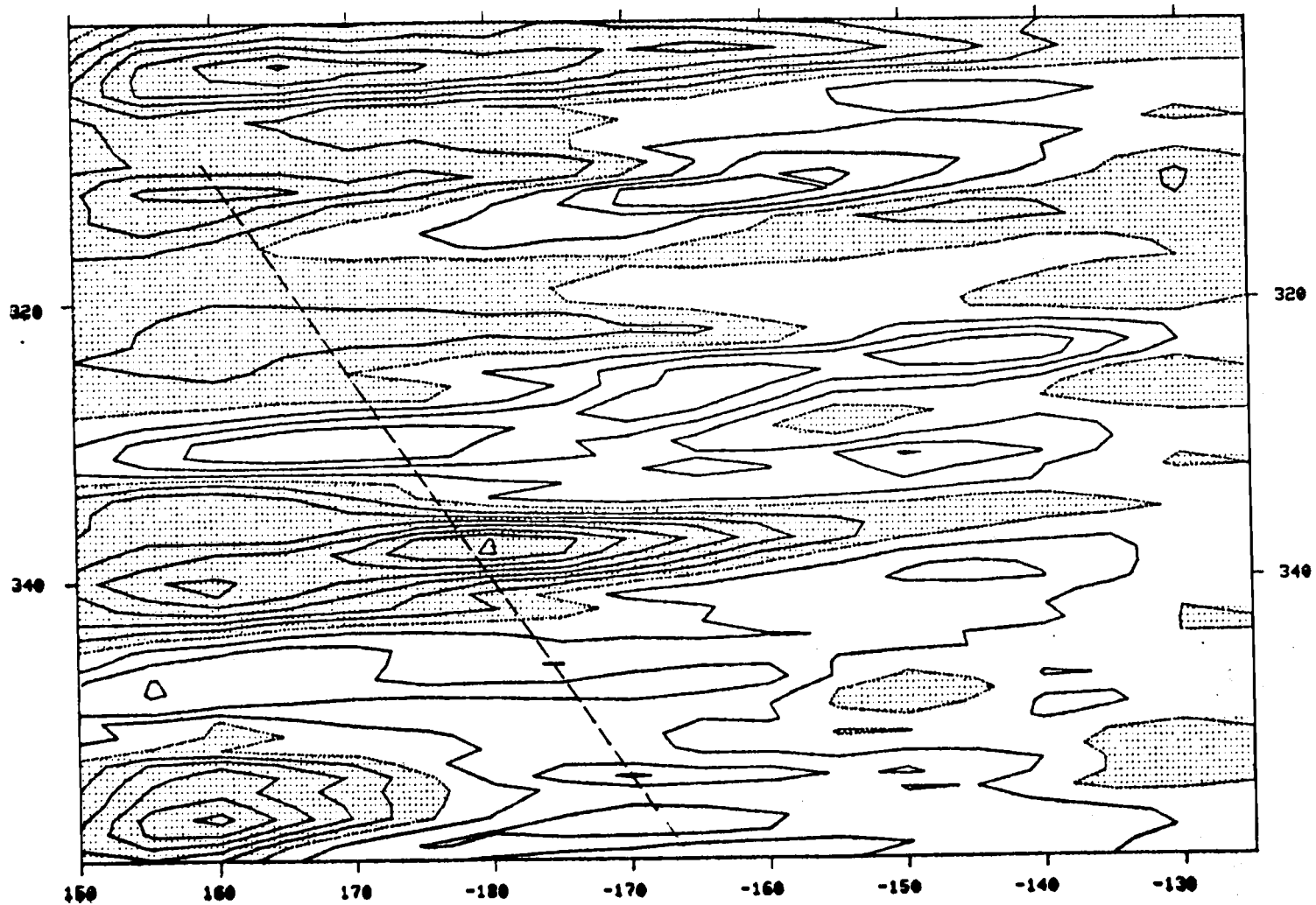


Fig. 4.4b. As in Fig. 4.4a except for day 300-360. The heavy dashed lines correspond to an eastward group velocity of 75cm/sec.

5. SUMMARY

Surface wind stress, as simulated by the OSU 2-level AGCM has been analyzed. The major findings are summarized as follows:

(1) 3-year mean vector fields reveal position shifts of the main gyres in the northern oceans compared with the observations. The cyclonic gyre in the Pacific Ocean is approximately 15 degrees too far south compared with the observed position. The cyclonic and anticyclonic gyres over Atlantic Ocean are about 10 to 20 degrees south of the observed. The distribution over the southern oceans is, well simulated.

(2) Magnitudes of the 3-year mean wind stress are generally smaller than the observations as revealed in the components fields. The difference is especially distinct in the Southern Hemisphere.

(3) The vertical component of the wind stress curl generally bears the same characteristics as the stress fields, i.e. positioning differences in the Northern Hemisphere and magnitude differences in the Southern Hemisphere.

(4) The root mean square wind stress field shows that the maximum time variability occurs in the northern oceans near the northern boundary and western part of the oceans.

(5) Seasonal variability is strongly dependent on

latitude. Annual variation dominates most latitudes. Semi-annual variation is found only at high latitudes in the southern Hemisphere. The most distinct annual cycle over Indian ocean monsoon area is missing in the simulated field.

(6) Autospectral analysis of wind stress shows a similar spectral shape to that of the observed stress. The spectrum is generally white at low frequencies. It drops sharply at a frequency corresponding to the synoptic time scale. No significant peak is found at any frequency for extratropical latitudes. However, a distinct diurnal cycle is found in the tropical area.

(2) The annual peak is resolvable by using a narrower spectral window. The peak is much more dominant in the stress magnitude than in the stress components, which reveals the nonstationary characteristics of the stress field. The fluctuations are stronger in winter than in summer.

(8) Cross-spectral analysis shows that the eastward propagating disturbances of synoptic time scale dominate the variability as is found in the real atmosphere. Disturbances in the meridional direction are rather symmetric. Low frequency disturbances are also symmetric and have no preferred propagation directions.

An experiment using a homogeneous ocean which is

driven by AGCM simulated wind stress has been carried out using a barotropic version of OSU six-layer OGCM. We found:

- (1) The positions of the major circulations are largely controlled by the wind stress curl field. Thus, the annual mean circulations in the Northern Hemisphere driven by AGCM simulated wind stress reveal a southward shift compared to that driven by observed wind stress. The circulations in the Southern Hemisphere agree well with that driven by observed wind stress.
- (2) The annual variabilities of the mass transport in most oceans for the present study are larger than that of the observed wind stress case. This is probably due to the stronger seasonal variability of the simulated wind field.
- (3) Planetary waves with westward phase propagation at the speed of 9-10 m/sec and eastward group velocity of 70-80 cm/sec are likely to be the major part of the response of the barotropic model to the fluctuating winds.

The overall performance of the simulated wind stress is satisfactory. However, the positioning error of the main gyre in the northern oceans must be improved in view of its important effects on the ocean transport. A further diagnostic study of the spatial and temporal variabilities of the wind stress curl is needed due to its importance in modifying the ocean response (Leetmaa, 1978).

A cross-spectral analysis between the ocean response and the atmospheric forcing, e.g. the streamfunction and the wind stress curl, should also be done in order to quantitatively understand the response of the model to the forcing.

BIBLIOGRAPHY

- Bryan, K., 1963: A numerical investigation of a nonlinear model of a wind-driven ocean. J. Atmos. Sci., 20, 594-606.
- Bunker, A. F., 1976: Computations of surface energy flux and annual air-sea interaction cycles of the North Atlantic Ocean. Mon. Wea. Rev., 104, 1122-1140.
- Deacon, E. L. and E. K. Webb, 1962: Small scale interaction. The Sea, Vol. I, Interscience Publishers, New York, pp. 43-80.
- Esbensen, S. K. and R. W. Reynolds, 1981: Estimating Monthly averaged air-sea transfers of heat and momentum using the bulk aerodynamic method. J. Phys. Oceanogr., 11, 457-465.
- Fissel, D., S. Pond and M. Miyake, 1976: Spectra of surface Atmospheric Quantities at ocean weather ship P. Atmosphere, 14, 77-97.
- Frye, D. E., S. Pond and W. P. Elliott, 1972: Note on the kinetic energy spectrum of coastal winds. Mon. Wea. Rev., 100, 671-672.
- Garratt, J. R., 1977: Review of drag coefficients over oceans and continents. Mon. Wea. Rev., 105, 915-929.
- Gates, W. L., 1979: The climate system and its portrayal by climate models: A review of basic principles. I. Physical basis of climate. Climate Variations and Variability: Facts and Theories, A. Berger, ed., NATO advance study Institute Series, Riedel, Rordrecht, pp.3-19.
- , E. S. Batten, A. B. Kahle and A. B. Nelson, 1971: A documentation of the Mintz-Arakawa two-level atmospheric general circulation model. R-877-ARPA, The Rand Corporation, Santa Monica, CA, 408pp.
- and A. B. Nelson, 1975: A new tabulation of the Scripps topography on a 1 global grid. Part II. Ocean depths. R-1227-1-ARPA, The Rand Corporation, Santa Monica, CA, 132pp.
- and M. E. Schlesinger, 1977: Numerical simulation of the January and July global climate with a two-level atmospheric model. J. Atmos. Sci., 34, 36-76.

- Godfrey, J. S. and T. J. Golding, 1981: The Sverdrup relation in the Indian Ocean, and the effect of Pacific-Indian Ocean throughflow on Indian Ocean circulation and on East Australia current. J. Phys. Oceanogr., 11, 771-779.
- Han, Y.-J. and W. L. Gates, 1982a: Preliminary analysis of the performance of the OSU six-level oceanic general circulation model. Part I. Basic design and barotropic experiment. Report No.30, Climatic Research Institute Oregon State University, Corvallis, 53pp.
- and W. L. Gates, 1982b: -----. Part II. A baroclinic experiment. Report No.34, Climatic Research Institute, Oregon State University, Corvallis, 54pp.
- and S.-W. Lee, 1981: A new analysis of monthly wind stress over the global ocean. Report No.26, Climatic Research Institute, Oregon State University, Corvallis, 148pp.
- Haney, R. L., 1971: Surface Thermal boundary condition for ocean circulation models. J. Phys. Oceanogr., 1, 241-248.
- Hellerman, S., 1963: Computation of wind stress fields over the Atlantic Ocean. Mon. Wea. Rev., 93, 239-244.
- , 1967: An updated estimate of the wind stress on the world ocean. Mon. Wea. Rev., 95, 607-626. (Correction, Mon. Wea. Rev., 96, 63-74, 1968)
- Hidaka, K., 1958: Computation of the wind-stress over the oceans. Record of Oceanographic Works in Japan, 4, 77-123.
- Houze, R. A., Jr., S. G. Geotis, F. D. Marks, Jr., and A. K. West, 1981: Winter monsoon convection in the vicinity of North Borneo, I, Structure and time variation of the clouds and precipitation. Mon. Wea. Rev., 109, 1595-1614.
- Hwang, H., 1970: Power density spectrum of surface wind speed on Palmyra Island. Mon. Wea. Rev., 98, 70-74.
- Jenkins, J. M. and D. G. Watts, 1968: Spectral analysis and its applications. Holden-Day, San Francisco, 525pp.
- Leetmaa, A., 1978: Fluctuating winds: An energy source for mesoscale motions. J. Geophys. Res., 83, 427-430.

- Manabe, S., 1969: Climate and the ocean circulation. II. The atmospheric circulation and the effect of heat transfer by ocean currents. Mon. Wea. Rev., 97, 775-805.
- , K. Bryan and M. J. Spelman, 1975: A global ocean-atmosphere climate model. Part I. The atmospheric circulation. J. Phys. Oceanogr., 5, 3-29.
- McBride, J. L. and W. M. Gray, 1980: Mass divergence in tropical weather systems, I, Diurnal variations. Quart. J. R. Meteorol. Soc., 106, 501-516.
- Otnes, R. K. and L. Enochson, 1972: Digital time series analysis. Wiley, New York, 467pp.
- Schlesinger, M. E. and W. L. Gates, 1979: Numerical simulation of the January and July global climate with the OSU two-level Atmospheric general circulation model. Report No. 9, Climatic Research Institute, Oregon State University, Corvallis, 102pp.
- and W. L. Gates, 1981: Preliminary analysis of four general circulation model experiments on the role of the ocean in climate. Report No. 25, Climatic research Institute, Oregon State University, Corvallis, 56pp.
- Sverdrup, H. U., 1947: Wind-driven currents in a baroclinic ocean; with application to the equatorial currents of the eastern Pacific. Proc. Nat. Acad. Sci., 33, 318-326.
- Vonder Haar, T. H., and A. H. Jort, 1973: New estimate of annual poleward energy transport by Northern Hemisphere oceans. J. Phys. Oceanogr., 2, 169-172.
- Welander, P., 1975: Analytical Modeling of the oceanic circulation. Proceedings of Symposium on Numerical Methods of Ocean Circulation. National Academy of Sciences, Washington D. C., pp. 63-75.
- Willebrand, J., 1978: Temporal and spatial scales of the wind field over the North Pacific and North Atlantic. J. Phys. Oceanogr., 8, 1080-1094.
- , S. G. H. Philander and R. C. Pacanowski, 1980: The oceanic response to large-scale atmospheric disturbances. J. Phys. Oceanogr., 10, 411-429.